

# IMPROVING LIGHT SHEET MICROSCOPY PERFORMANCE FOR THICK SAMPLES

by

YANG LIU

(Under the Direction of Peter A. Kner)

## ABSTRACT

Light sheet fluorescence microscopy (LSFM) is the best method for high-speed imaging of thick, live samples over a large field of view (FOV). In this dissertation, we describe four different projects to improve LSFM's performance.

Though LSFM provides excellent temporal resolution and optical sectioning, the images are affected by sample size and thickness. Scattering introduces background light, leading to a lower signal-to-noise ratio (SNR). We have implemented optical sectioning structured illumination (SIM), improving SNR by a factor of 5.6. Further, the system's imaging speed can capture seizure dynamics in the central nervous system (CNS) of zebrafish larvae.

Stripe artifacts in LSFM lower image quality. No current solutions are optimized for SIM-LSFM. To mitigate artifacts while improving optical sectioning capabilities for semi-opaque specimens using SIM, we developed an axial dithering approach that reduces stripe artifacts by 20% at 156 microns deep into the specimen and an adaptive reconstruction approach to improve the image with 38% increase in uniformity. The volumetric imaging speed of LSFM can be accelerated through the use of an Electrical Tunable Lens (ETL) which allows the focal plane imaged onto the camera to be rapidly adjusted, allowing for imaging at several volumes per second. However, it also introduces spatially varying aberrations. Here, we demonstrate a system combining adaptive optics and an ETL, improving the signal to background ratio by a factor of 3.5 across a 400 by 400 by 100  $\mu\text{m}^3$  volume. Further, it is fast enough to capture neural activities in the CNS of zebrafish larva.

The geometry of LSFM limits the resolution to the cellular level laterally and reduces its resolution by a factor of 3 axially. Improvement of axial resolution usually comes at the cost of FOV. We have developed a single-objective LSFM system with super-resolution SIM. This allows for multi-direction illumination with better penetration and isotropic resolution improvement. We have

measured fluorescent beads and cerebellum organoids with a lateral resolution 313nm and 1.64 $\mu$ m axial resolution over a 20 $\mu$ m axial range with 276 $\mu$ m FOV using 2D SIM. We demonstrate through simulations an achievable resolution of 161 nm by 767 nm.

**INDEX WORDS:** Fluorescence microscopy, Super-resolution microscopy, Structured illumination microscopy, Light-sheet microscopy, Wavefront correction , Adaptive Optics, Neural imaging

IMPROVING LIGHT SHEET MICROSCOPY PERFORMANCE FOR  
THICK SAMPLES

by

YANG LIU

B.S., University of Georgia, 2015

A Dissertation Submitted to the Graduate Faculty of the  
University of Georgia in Partial Fulfillment of the Requirements for the  
Degree

DOCTOR OF PHILOSOPHY

ATHENS, GEORGIA

2022

©2022  
Yang Liu  
All Rights Reserved

IMPROVING LIGHT SHEET MICROSCOPY PERFORMANCE FOR  
THICK SAMPLES

by

YANG LIU

Major Professor: Peter A. Kner

Committee: James D. Lauderdale  
Luke J. Mortensen  
Mable Fok

Electronic Version Approved:

Ron Walcott

Vice Provost for Graduate Education and Dean of the Graduate School

The University of Georgia

August 2022

# DEDICATION

I am thankful to God for this opportunity and to my wonderful family for their support during my Ph.D. This dissertation is dedicated to my wife Grace Liu, my daughter Wendy Liu, my parents Guanghong Diao and Delong Liu, and my parents-in-law Regina and Philip Palmer.

# ACKNOWLEDGMENTS

I would like to thank my advisor Dr. Peter Kner for his patience, guidance, and mentorship. Thank you to my collaborator Dr. James Lauderdale and his lab, to Dr. Daichi Kamiyama and his lab, and to my committee members including Dr. Kner, Dr. Lauderdale, Dr. Luke Mortensen, and Dr. Mabel Fok. I would also like to thank my colleagues Abhijit Marar, Keelan Lawrence, John Green, Nahain Siddique, Bingxi Liu, Ming Song, and Shaoheng Li for their help and support.

# CONTENTS

<b>Acknowledgments</b>	<b>v</b>
<b>List of Figures</b>	<b>vii</b>
<b>List of Tables</b>	<b>x</b>
<b>1 Introduction</b>	<b>1</b>
1.1 Wide Field Fluorescence Microscopy . . . . .	1
1.2 Nature of Light-Diffraction . . . . .	3
1.3 Resolution Limit and Point Spread Function . . . . .	4
1.4 Optical Sectioning in Wide Field Microscopy . . . . .	6
1.5 Light Sheet Fluorescence Microscopy . . . . .	8
1.6 Principle of Light Sheet Microscopy . . . . .	9
1.7 Parameters of Light Sheet Microscopy . . . . .	11
1.8 Configurations of Light Sheet Microscopy . . . . .	12
1.9 Superresolution Microscopy . . . . .	16
1.10 Stimulated Emission Depletion Microscopy . . . . .	17
1.11 Single Molecule Localization Microscopy . . . . .	19
1.12 Structured Illumination Microscopy . . . . .	19
1.13 Objectives of This Dissertation . . . . .	24
<b>2 Zebrafish neural imaging with light sheet microscopy</b>	<b>32</b>
2.1 Optical System Design . . . . .	34
2.2 Structured Illumination and Image Reconstruction . . . . .	36
2.3 Beads Sample Preparation . . . . .	37
2.4 Zebrafish Sample Preparation . . . . .	38
2.5 Data Analysis . . . . .	38
2.6 Results and Discussion . . . . .	38
2.7 Conclusion . . . . .	41

<b>3</b>	<b>Correcting artifacts in light sheet microscopy imaging</b>	<b>47</b>
3.1	Stripe artifact reduction for DSLM-SI . . . . .	48
3.2	Adaptive linear SR-SI reconstruction . . . . .	52
<b>4</b>	<b>Volumetric light sheet microscopy with an electrically tunable lens and adaptive optics</b>	<b>57</b>
4.1	Light Sheet Microscopy with Adaptive Optics . . . . .	58
4.2	3D Imaging of Light Sheet Microscopy . . . . .	59
4.3	Optical Setup . . . . .	61
4.4	ETL and Galvo Mirror Calibration . . . . .	63
4.5	Multi-Region AO Corrections . . . . .	63
4.6	Sample Preparation . . . . .	65
4.7	Signal-to-Background Ratio Comparison . . . . .	65
4.8	Image Fusion . . . . .	65
4.9	Results and Discussion . . . . .	66
<b>5</b>	<b>Single objective multi-direction illumination light sheet microscopy</b>	<b>71</b>
5.1	Optical Design . . . . .	72
5.2	Designing the Field of View . . . . .	74
5.3	3D Imaging with Reflected Light Sheet Microscopy . . . . .	76
5.4	Remote Focusing for 3D Imaging . . . . .	76
5.5	Illumination Synchronization . . . . .	80
5.6	Multi-Direction Light Sheet Illumination . . . . .	81
5.7	Imaging Area of the Multi-Direction Light Sheet . . . . .	82
5.8	Point Spread Function of the System and 3D Imaging . . . . .	82
5.9	Structured illumination with LSFM . . . . .	83
5.10	Investigation of Isotopic Resolution . . . . .	83
5.11	Conclusion . . . . .	84
<b>6</b>	<b>Conclusion</b>	<b>94</b>
	<b>Bibliography</b>	<b>96</b>
	<b>Appendices</b>	<b>124</b>
<b>A</b>		<b>124</b>
A.1	LLSM illumination pattern simulation . . . . .	124
A.2	Mask at conjugate back pupil plane . . . . .	134

# LIST OF FIGURES

1.1	widefield microscope . . . . .	3
1.2	illustration of diffraction and interference . . . . .	4
1.3	Wave optics view of the microscope system and diffraction limited PSf . . . . .	5
1.4	Resolution limit . . . . .	6
1.5	Demonstration of convolution in optical microscope imaging	7
1.6	PSF and 3D OTF . . . . .	8
1.7	Light Sheet Fluorescence Microscopy Schematic . . . . .	9
1.8	Static light sheet and scanning light sheet . . . . .	10
1.9	PSF of light sheet microscopy . . . . .	11
1.10	Gaussian light sheet parameters . . . . .	25
1.11	Configurations of LSFM . . . . .	26
1.12	Principle of a confocal microscope . . . . .	27
1.13	STED microscopy principle . . . . .	28
1.14	SMLM principle . . . . .	29
1.15	Principle of a SIM microscope . . . . .	30
1.16	SIM pattern comparison . . . . .	30
1.17	3D SIM principle . . . . .	31
2.1	Optical setup of the system . . . . .	34
2.2	Implementation of DSLM-SI . . . . .	35
2.3	Illumination beam profile characterization . . . . .	42
2.4	Point spread function . . . . .	43
2.5	Optical sectioned image comparison . . . . .	44
2.6	two color live imaging zebrafish . . . . .	45
2.7	3D image stack of zebrafish larva . . . . .	46
3.1	(A) Mechanism of axial dithering DSLM. (B) aDSLm Beam. (C) DSLM Beam. (D) Comparison of beam profiles in the axial direction. FWHM are $11.83\mu\text{m}$ and $7.14\mu\text{m}$ respectively. Scale bar is $10\mu\text{m}$ in (B). . . . .	48

3.2	Comparison of aDSL <sub>M</sub> and DSL <sub>M</sub> using a dye phantom. (A) aDSL <sub>M</sub> . (B) DSL <sub>M</sub> . (C) Line profiles along the line indicated in (A). (D) The ratio ( $\alpha$ ) of mean intensity to standard deviation at locations 1,2,3 in (B). $\alpha$ is the $\alpha$ of the entire image. (blue: aDSL <sub>M</sub> , red:DSL <sub>M</sub> ). Scale bar is $50\mu\text{m}$ . . . . .	49
3.3	Imaging of zebrafish larva. (A) aDSL <sub>M</sub> . (B) DSL <sub>M</sub> . (C) Line intensity profile (averaged over 10 pixels) at location noted in (A). Arrows point to regions where striping is strong in (B). Scale bar is $50\mu\text{m}$ , Sample is illuminated from right side. . . .	50
3.4	Comparison of aDSL <sub>M</sub> -SI (A) and DSL <sub>M</sub> -SI (B) using a dye phantom. The illumination pattern wavelength is $4.68\mu\text{m}$ . (C) The line intensity profile plotted at location noted in (B). The blue arrow points to a region where the stripe pattern is notably absent in the DSL <sub>M</sub> -SI image. Scale bar is $40\mu\text{m}$ . . . .	51
3.5	Point spread function (PSF) comparison using beads phantom. (A),(B),(E),(F) show the lateral PSF. Pixel size $97.5 \times 97.5 \text{ nm}^2$ . (C),(D),(G),(H) show the axial PSF. Pixel size of $0.0975 \times 1.5\mu\text{m}^2$ . (I) and (J) are the intensity profiles of the lateral PSF and axial PSF, respectively. Scale bars in A and E are $20\mu\text{m}$ and scale bars in C and G are $4\mu\text{m}$ . . . . .	52
3.6	Imaging of zebrafish larvae. (A) Uniform LR-SI. (B) Adaptive LR-SI. (C) and (D) are enlargements of (A) and (B) respectively at the location of the box in (A). Arrows indicate regions where the distortion of the uniform LR-SI result is evident. The scale bars in A and C are $30\mu\text{m}$ and $10\mu\text{m}$ respectively. Sample illumination is from the right side. . . . .	53
3.7	(A),(B) and (C) are RMS-DSL <sub>M</sub> -SI, RMS-aDSL <sub>M</sub> -SI, and adaptive-aDSL <sub>M</sub> -SI respectively. (C),(D) and (E) are respective close-ups of the box area shown in (A). Arrows point to areas where the stripe artifact is especially strong on the RMS-DSL <sub>M</sub> -SI image. (G-I) Respective line profiles at the position indicated in (A) by the yellow line. Scale bar in (A) is $50\mu\text{m}$ and $20\mu\text{m}$ in (D). Sample is illuminated from right side. . . .	54
3.8	Performance comparison using 3-dpf zebrafish larva. (A) RMS-SI image and the region of interest locations. (B) Ratio of mean intensity to SD for the different methods at the regions indicated by blue boxes in (A). (C)-(E) Power Spectra of the region indicated by the red box in (A). Scale bar is $30\mu\text{m}$ in (A), and $0.2\mu\text{m}^{-1}$ in (C). Sample illumination is from the right side.	56

4.1	Principle of aberration correction in high-resolution optical microscopy . . . . .	58
4.2	fishAO . . . . .	60
4.3	Aberration from ETL . . . . .	61
4.4	Schematic of the optical setup. . . . .	62
4.5	ETL calibration with light sheet position . . . . .	64
4.6	Multi-region mapped AO . . . . .	67
4.7	Multi-region mapped AO . . . . .	68
4.8	Multi correction AO for ETL-LSFM on zebrafish larva . . . . .	69
4.9	Multi correction AO for ETL-LSFM on zebrafish larva . . . . .	69
4.10	ETL-LSFM with AO on neural activities imaging . . . . .	70
5.1	Schematic of the optical setup. . . . .	73
5.2	Fov and light sheet thickness. . . . .	75
5.3	Optical design of the remote focusing system . . . . .	77
5.4	Optical ray tracing of the remote focusing system . . . . .	78
5.5	Illustration of defocus . . . . .	79
5.6	illumination synchronization . . . . .	81
5.7	Light throughput comparison . . . . .	85
5.8	Multi-direction light sheet illumination working principle . . . . .	86
5.9	Multi-Direction Light Sheet Illumination . . . . .	87
5.10	Imaging Area of the Multi-Direction Light Sheet . . . . .	88
5.11	Point spread function of the light sheet system . . . . .	89
5.12	fruitfly 3D image stack . . . . .	90
5.13	LSFM with SIM illumination patterns . . . . .	91
5.14	PSF of SIM with LSFM . . . . .	92
5.15	Simulation of performances of the system with different illumination patterns . . . . .	93

# LIST OF TABLES

1.1	Table of different resolution criteria [9]. . . . .	6
-----	---	---

# CHAPTER I

## INTRODUCTION

The ability to observe a process or object under investigation is a critical step towards fundamental understanding. Imaging technologies have enabled us to gain this ability on macroscopic and microscopic levels, making them very important tools for the advancement of science and our knowledge of nature. Among all of the imaging techniques available, light microscopy has played perhaps the most substantial role in the study of biological science. Light microscopes use a series of lenses and visible light to enlarge the image of an object. These instruments allow researchers to examine details that are normally invisible to the human eye.

### **1.1 Wide Field Fluorescence Microscopy**

The first documented biological application of optical microscopy dates back to the 1630s. Italian scholars Fredrico Cesi and Francesco Stelluti used an optical microscope to investigate the anatomy of bees and weevils [8]. Later, Antoni Van Leeuwenhoek used an optical microscope to observe microorganisms, which set the foundation for modern microbiology. In 1665, Robert Hook published *Micrographia*, documenting his observation of insects and plants. Hook is also credited with the origin of the term “cell,” which he used to describe the boxlike structures he observed in cork tissue [48, 82]. As technology advanced, the modern digital microscope developed, and presently such microscopes are usually equipped with digital cameras. A user can observe the sample while partially or fully controlling the microscope with a computer.

In conventional optical microscopy (bright-field microscopy), a sample is often illuminated from one side and the transmitted light is collected on the other side. The contrast of the final image is the result of absorption and scattering from the dense area of the sample [185]. However, without any additional

staining, bright-field imaging of living cells suffers from low contrast, because cells are largely transparent. Phase contrast microscopy addresses this issue by introducing additional optics that convert the phase shifts caused by the specimen to intensity changes in the image. Phase contrast microscopy allows us to observe many cellular structures in detail, structures which cannot be seen with conventional bright-field microscopy imaging. In 1953, the Dutch physicist Frits Zernike was awarded a Nobel Prize in Physics for his invention of phase contrast microscopy. Phase contrast microscopy works well for thin samples. However, for thicker samples, differential interference contrast microscopy (DIC) is a better technique to use. DIC gives a pseudo-three-dimensional (3D) shaded appearance to cells. [138, 185]

The term fluorescence refers to a physico-chemical energy exchange whereby shorter wavelength photons are absorbed by a molecule and are re-emitted as longer wavelength photons [128]. The emission light is usually within the visible wavelength. Fluorophores (or fluorochromes) were first used in optical microscopy to tag certain components or parts of a specimen for observation and imaging. This occurs through the use of a concept called immunofluorescence. This technique uses the specificity of an antibody or antigen, in conjunction with the fluorochrome, to label specific biological molecule targets within a specimen. Immunofluorescence was first conceptualized in 1941 [34] and later demonstrated [33] in an experiment involving the labelling of antibodies with a fluorophore. According to the online Molecular Probes Handbook, Tenth Edition, there are about 3,000 molecular probes that can be used to label almost any aspect of a biological system. Fluorescence microscopy provides great specificity, contrast, and sensitivity, and has become a workhorse in biological research due to its many benefits. Figure. 1.1 is a simplified epifluorescence microscope setup. It generally includes a light source illuminating the sample uniformly at the excitation wavelength, a dichroic mirror which separates the excitation light from the emission fluorescence light, a tube lens which forms a final image onto the camera, and then an emission filter with a specific bandpass in the optical path to further filter out any light with an unwanted wavelength. This concept first originated in 1911 [74], and a very early prototype was demonstrated in 1929 [41, 53].

In the 1960s, naturally fluorescent gene products such as green fluorescent proteins (GFPs) were first reported on by Osamu Shimomura, through observation of the bioluminescence phenomena in jellyfish *Aequorea Victoria* [170]. In 2008, Roger Y. Tsien, Osamu Shimomura, and Martin Chalfie were awarded the Nobel Prize in Chemistry for their discovery and development of the GFP. The discovery of the fluorescence protein significantly advanced the field of

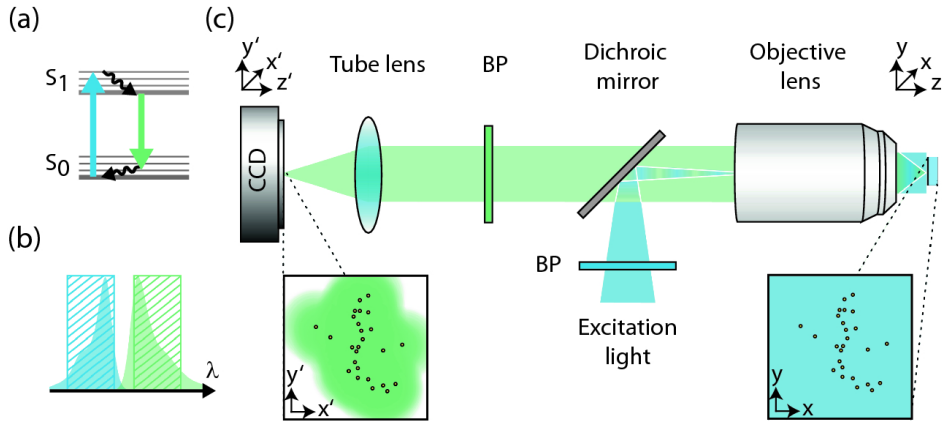


Figure 1.1: (a) Jablonski diagram of a fluorescent molecule. By absorption of a photon, the molecule can be excited from the electronic ground state,  $S_0$ , into any vibrational level of  $S_1$ . The molecule can return to any vibrational level of  $S_0$  by the spontaneous emission of a photon (fluorescence). From there it relaxes non-radiatively into its lowest vibrational level. (b). Absorption (blue) and emission (green) spectrum of a fluorescent molecule. The hatched areas indicate the transmission range of the respective bandpass filters. (c). Basic wide-field fluorescence microscope with epi-illumination. This figure is reprinted from Ref [40]

biological research, making it possible to study living, multicellular biological systems in more depth and detail than could previously be achieved.

## 1.2 Nature of Light-Diffraction

Optical microscopes allow us to visualize the fine structures and details of a specimen through a magnified image. However, increased magnification does not necessarily result in an increased ability to see these detailed structures. [86] The clarity of an image is necessarily governed by diffraction, which is a fundamental characteristic of light waves (in addition to reflection and refraction). Diffraction refers to the bending phenomenon of the light wave when it passes around the edge of an obstacle or small opening. This was first observed and termed by the Italian scientist Grimaladi, in his study of the deviation of light from rectilinear propagation in 1665 [66, 72]. In 1804, another important concept, the interference of light (the phenomenon of two light waves superimposed to form a resultant wave of greater, lower, or the sample amplitude) was introduced by

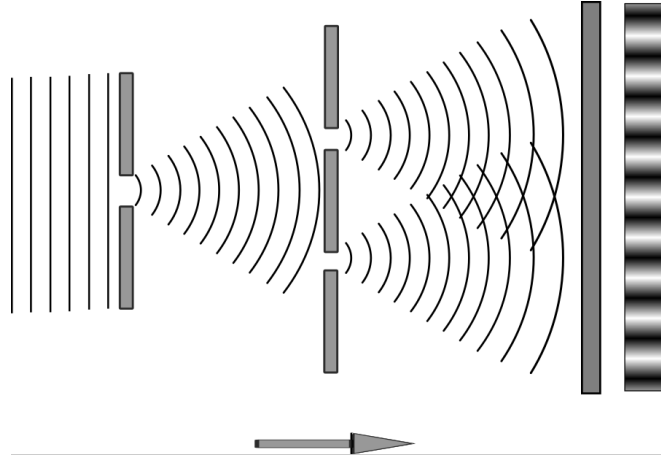


Figure 1.2: illustration of diffraction and interference

English physician Thomas Young through his experimental observation, also known as Young's double-slit experiment [64]. The combination of diffraction and interference is often explained in terms of the Huygens-Fresnel principle, which states that each point on a wavefront can be considered as a source of a new spherical wavelets with the same frequency as that of the primary wave [72]. This is shown in Figure. 1.2.

### 1.3 Resolution Limit and Point Spread Function

As shown in Figure. 1.3 (a), the limited collection angle and finite aperture of the microscope system will cause diffraction to occur and will blur the image of a point from the object plane. The 3D intensity distribution of the image of a point object is called the point spread function (PSF). The resolution of an optical microscope is defined by the smallest distance between two points that can still be distinguished in the image. German physicist Ernst Abbe concluded that the minimum resolvable distance is directly related to the wavelength of the light and the maximum collection angle [1].

$$d_{\text{Abbe}} = \frac{\lambda}{2n \sin(\alpha)} \quad (1.1)$$

Here  $\lambda$  is the wavelength of the the light,  $n$  is the refractive index of the immersion medium, and  $\alpha$  is the half aperture angle of the objective lens. The product of the refractive index and  $\sin(\alpha)$  is the numerical aperture (NA),

where  $NA = n \sin(\alpha)$ . The axial resolution limit is approximated as follows:

$$d_{\text{Abbe,axial}} = \frac{2\lambda}{NA^2} \quad (1.2)$$

Lord Rayleigh (John William Strutt) later published another equation address-

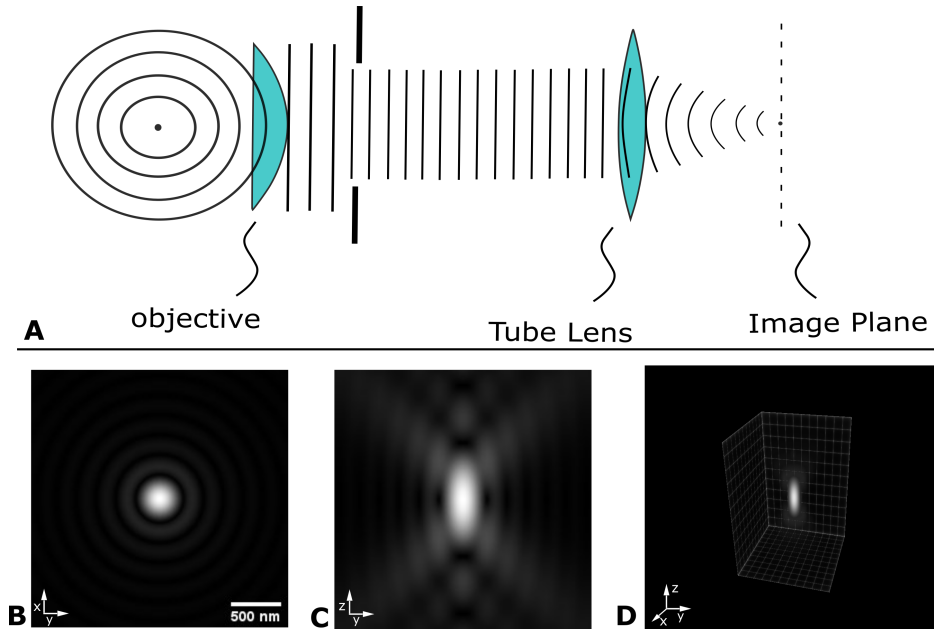


Figure 1.3: (A). Wave optics view of the microscope system. (B)-(D). Simulated 3D PSF with 550nm,  $NA=1.4$  and refractive index  $n=1.515$ , smallest lateral resolution of 200nm and axial resolution of  $\sim 500$ nm.

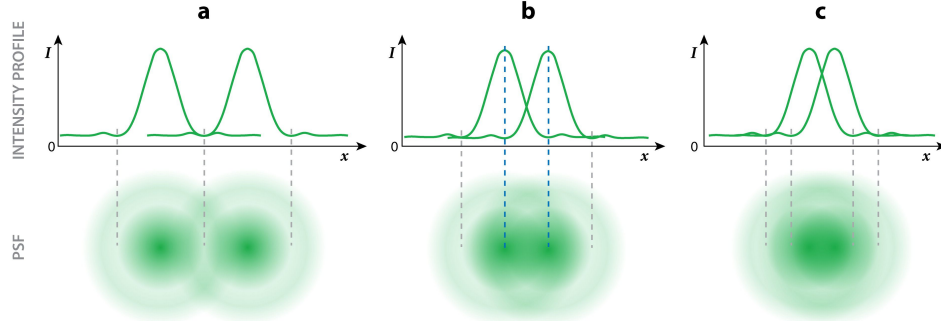
ing the study of self-luminous objects. This formula is now known as the Rayleigh criterion. It states that the central point of the diffraction spot coincides with the first diffraction minimum of the other diffraction spot on the image plane, and the two points on the sample are said to be resolved. [154] The formula is as follows:

$$d_{\text{Rayleigh}} = \frac{0.61\lambda}{NA} \quad (1.3)$$

Other criteria have been introduced throughout the years (e.g., the Sparrow criterion) to overcome bottlenecks, such as the fact that the Rayleigh criterion might hold for the eyes but not for detectors sensitive to small intensity variations, for instance, modern cameras. In most cases, resolution criteria are arbitrary and their values remain close to each other.

Table 1.1: Table of different resolution criteria [9].

Rayleigh	Sparrow	Abbe
$0.61 \lambda/NA$	$0.47 \lambda/NA$	$0.5 \lambda/NA$



 Jost A, Heintzmann R. 2013. Annu. Rev. Mater. Res. 43:261–82

Figure 1.4: Airy discs as a model for PSFs and showing the Rayleigh criterion. The gray dashed lines indicate the position of the first minimum. (a) The distance between the two points is larger than the resolution limit. (b) The two blue dashed lines are separated by a radius of the Airy pattern. (c) The distance between the two point sources is smaller than the resolution limit. The figure is adapted from [98].

## 1.4 Optical Sectioning in Wide Field Microscopy

In the imaging process of an optical microscope, the light rays from each point on the object converge at a corresponding point in a plane, and each of the points can be regarded as an individual point object. After passing through the optical microscope system, these point objects will result in a blurry image. We can describe the imaging process in terms of a convolution operation [98], and a detailed mathematical proof can be found in Ref [64]:

$$u_1(u, v) = \iint_{-\infty}^{\infty} h(u, v; \xi, \eta) u_0(\xi, \eta) \quad (1.4)$$

Here,  $u_1(u, v)$  is the field distribution at the image plane of the system, and  $u_0(\xi, \eta)$  is the electric field distribution at the object plane.  $h(u, v; \xi, \eta)$  is the impulse response function of this process. This function is also known as the PSF of the microscope. The PSF of the microscope is closely related to the pupil function ( $P(x, y)$ ) of the system, and this is shown in equation 1.5. Here,

$\tilde{\xi} = M\xi, \tilde{\eta} = M\eta$ ,  $M$  is the magnification between the object-plane and image-plane.

$$h(u, v; \tilde{\xi}, \tilde{\eta}) = \frac{1}{\lambda^2 z_1 z_2} \iint_{-\infty}^{\infty} P(x, y) \exp\left\{-j \frac{2\pi}{\lambda z_2} [(u - \tilde{\xi})x + (v - \tilde{\eta})y]\right\} dx dy \quad (1.5)$$

For fluorescence imaging, the PSF is equal to  $|h(u, v; \tilde{\xi}, \tilde{\eta})|^2$ . The convolution theorem states that the Fourier transform of a convolution is equal to the pointwise product of its Fourier transforms. The Fourier transform of the PSF is called the optical transfer function (OTF). The OTF describes the ability of the imaging system to transfer incoherent intensity information [98]. Figure 1.5 is an example of this concept. The Fast Fourier transform (FFT) is an efficient method of performing Fourier transforms on discrete signals, such as digital images captured by a camera.

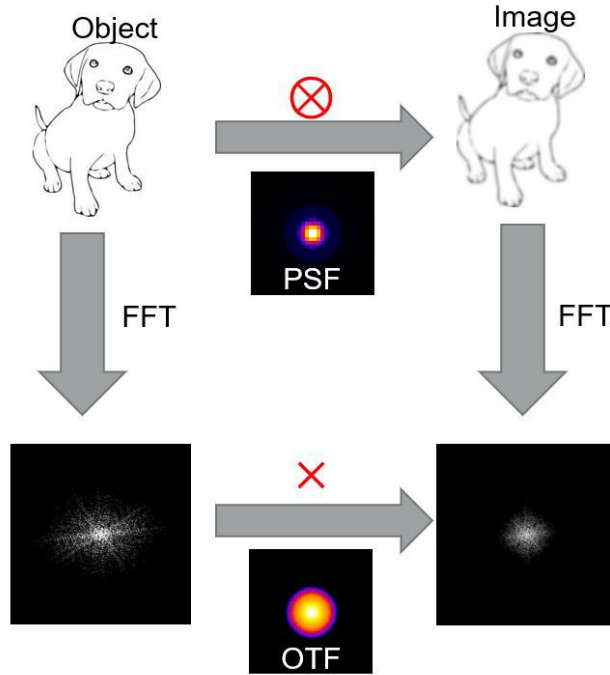


Figure 1.5: Demonstration of convolution in optical microscope imaging.

Here, lenses in the microscope perform a Fourier transform of the optical field in between their front and back focal planes [64]. In the fluorescence imaging system, a fluorescent molecule emits light in all directions. However, only a portion of that light is propagated through the objective lens. This directly translates to a limited support region of the OTF. This OTF determines the maximum spatial frequency range that can pass through the system. Figure 1.6

(a) shows the axial plot of a 3D PSF for a wide field fluorescence microscope, with the corresponding 3D OTF shown on the right. The 3D OTF has a toroidal shape with a cone-shaped space left in the axial direction. Figure 1.6(c) shows a two-dimensional OTF at a different focal position. As the object moves further away from the focal plane, fewer high spatial frequency components are able to pass through the system, i.e., less finer detail can be resolved. On the contrary, components at the lower portion of the frequency spectrum (closer to zero) pass through the optical system regardless of their distance from the focal plane. This indicates that both in-focus light and out-of-focus light all contribute to the formation of a final image. Therefore, the wide-field microscope lacks optical sectioning capability (i.e., the microscope's ability to distinguish features in the focal volume while discriminating from the background signal) [32], and the resulting image often has a low signal-to-background ratio [175].

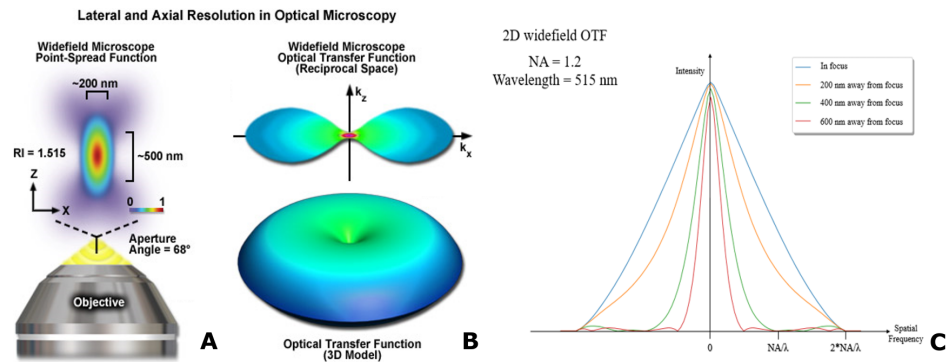


Figure 1.6: (A). 3D PSF wide field fluorescence microscope. (B)-(C). 3D and 2D OTF of wide field fluorescence microscope. Figures (A) and (B) are adapted from Ref [210].

## 1.5 Light Sheet Fluorescence Microscopy

Combining wide field imaging with light sheet illumination is one promising approach to creating optical sectioning. This type of microscope is termed Light Sheet Fluorescence Microscopy (LSFM) or Selective Plane Illumination Microscopy (SPIM). This technique was first described in 1903 by Richard Zsigmondy and Henry Siedentopf [172, 104]. At that time, it was termed Ultramicroscopy and it was used during the 1990s, primarily in chemistry and materials science [104]. The first biological application was demonstrated in 1993 by Voie et al [194]. However, LSFM only gained traction in 2004 when it was first applied to in vivo imaging [91]. Since then, the field of LSFM has

grown quickly. This is primarily due to its flexibility. Researchers can optimize resolution, penetration depth, and acquisition speed, making LSFM an attractive option for application to a wide range of research scenarios.

## 1.6 Principle of Light Sheet Microscopy

LSFM uses an orthogonal illumination scheme, where only a thin section of the sample at the focal plane of the detection objective lens is illuminated. In this way, a minimum amount of out-of-focus fluorescence light is introduced into the detection portion of the system. The entire 2D cross-section of the sample can be captured rapidly, and the imaging speed can be as fast as the limit of the capturing speed of the camera in 2D. The 3D image stack is captured by taking a series of 2D images, either by moving the sample or by moving the illumination light sheet and focal plane.

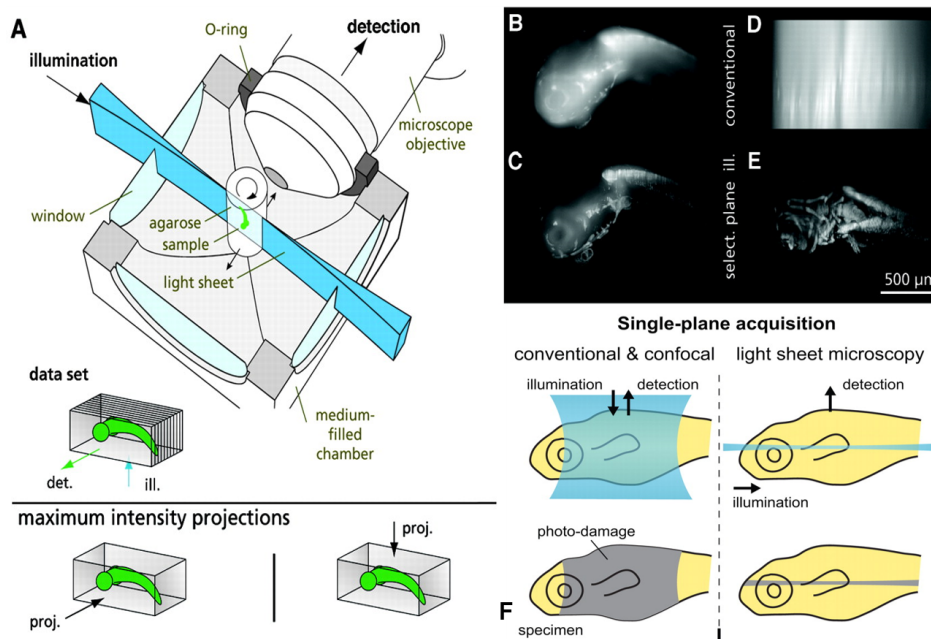


Figure 1.7: Basic configuration of LSFM. (A). The sample is embedded in a cylinder of agarose gel or in a FEP tube. The sample holder is held in a mechanical translation and rotation stage. (B) and (D) show the maximum projections of a Medaka embryo, viewed from the lateral and dorsal ventral positions, using conventional epi-illumination. (C) and (E) show the light sheet illumination versions of (B) and (D), respectively. (F) is an explanation of the reduction in photo-damage to the sample and the mechanism of the optical sectioning used by the light sheet microscope. (A)-(E) are adapted from Ref [91] and (F) is adapted from Ref [107].

LSFM results in much less photo-damage to the sample as opposed to conventional illumination methods (i.e., wide field and confocal illumination), because only a section of the sample is illuminated. This is shown in Figure 1.7 (F). The reduced photo-damage, in addition to the high imaging speed, makes LSFM a great choice for live imaging applications. LSFMs can be categorized into two major groups, as shown in Fig. 4.10. One type of LSFM uses a static light sheet, and the other forms a light sheet by rapidly scanning a circular beam (also known as digital scanned light sheet fluorescence microscopy, or DSLM) [106]. Both approaches have their advantages and disadvantages, which are discussed in a later section.

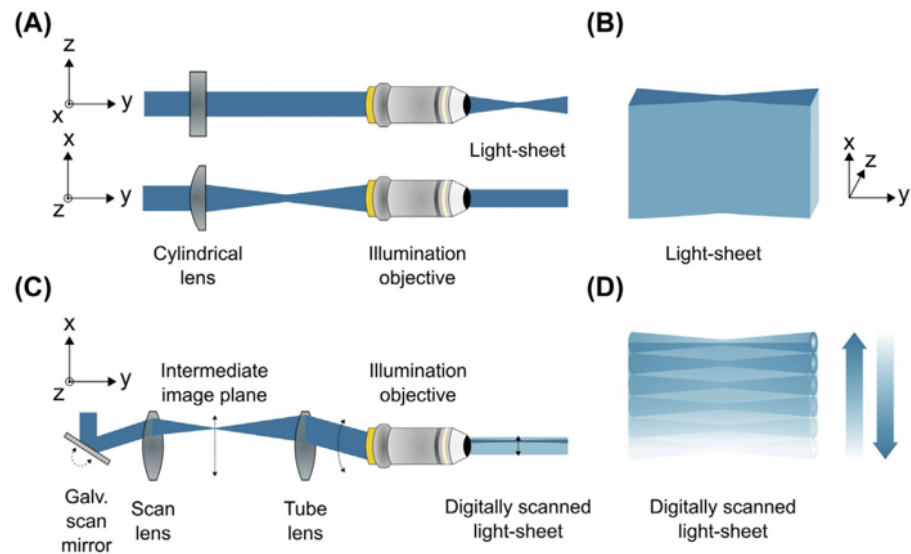


Figure 1.8: Static versus digitally scanned light-sheet. (A-B) Generation of a static light-sheet: while the Gaussian beam stays columnated in the  $yz$ -plane, the cylindrical lens (side view up, top view down) focuses it in the  $xy$ -plane before it enters the illumination objective. This results in an extended beam in the  $xy$ -plane that is focused on the  $z$ -axis (B). (C-D) Generation of a digitally scanned light-sheet: the combination of a galvanometric scan mirror and a scan lens leads to a focused beam in the intermediate image plane between the scan lens and the tube lens. The rotation of the galvanometric scan mirror also corresponds to a rotation in front of the illumination objective, which leads to a translation along the  $x$ -axis in the intermediate image plane, and therefore the translation of the beam in the  $x$ -axis of the actual image plane. The result is a digitally scanned light-sheet (D). This figure is adapted from Ref [113].

## 1.7 Parameters of Light Sheet Microscopy

**Resolution of the light sheet microscope** Due to the wide field imaging nature of LSFM, the lateral resolution of LSFM is primarily governed by the numerical aperture of the detection objective lens, and its axial resolution is determined by the combination of the light sheet thickness and the axial point spread function of the imaging objective lens [59]. The resolution can be described by the following equations:

$$d_{\text{lateral}} = \frac{\lambda_{\text{em}}}{2\text{NA}_{\text{det}}}, \quad d_{\text{axial}} = \left( \frac{2\text{NA}_{\text{exc}}}{\lambda_{\text{exc}}} + \frac{n(1 - \cos\theta_{\text{det}})}{\lambda_{\text{em}}} \right)^{-1} \quad (1.6)$$

Where  $\lambda_{\text{em}}$  is the wavelength of the emission light and  $\lambda_{\text{exc}}$  is the wavelength of the excitation light,  $\text{NA}_{\text{det}}$  and  $\text{NA}_{\text{exc}}$  refer to the detection and the excitation numerical apertures respectively, and  $\theta_{\text{det}} = \arcsin(\text{NA}_{\text{det}}/n)$  is the half-angle of the light collection. According to this equation, the higher the excitation NA, the thinner the light sheet, and therefore the better the axial resolution.

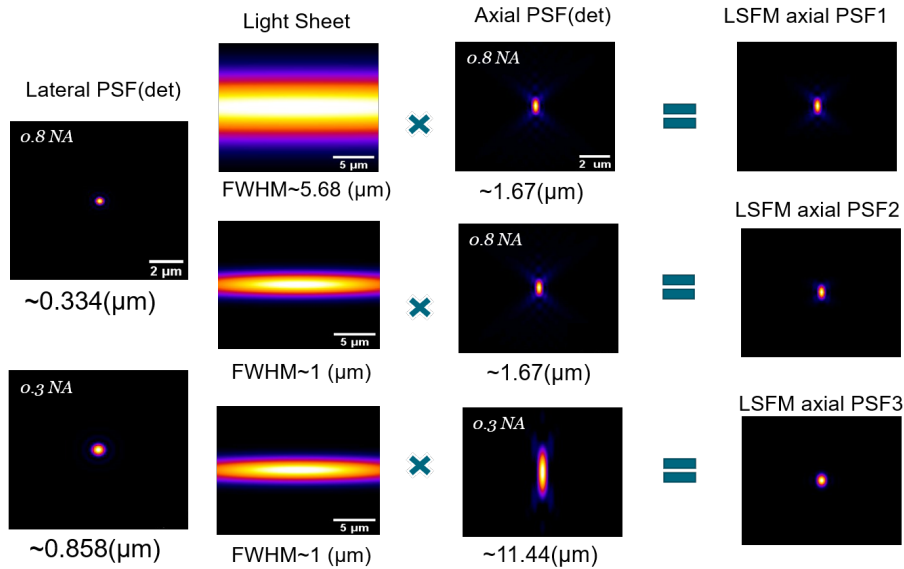


Figure 1.9: PSF simulation of LSFM with different lateral and axial resolutions, and different thicknesses of the illumination light sheet. When a thick light sheet is employed, the axial resolution of the system is primarily determined by the high NA detection objective (0.8NA). This is shown when the thickness of the illumination light sheet is smaller than the axial PSF of the detection objective (0.3NA). The resulting PSF is determined by the thickness of the light sheet.

**Field of view of light sheet microscopy** One would think that in order to achieve a superior axial resolution, the thinnest possible light sheet would be ideal. However, there is a trade-off that takes place between the axial resolution and the field of view (FOV) of the light sheet system, owing to the diffraction of light.

Figure 1.10 shows a static Gaussian light sheet formed by a cylindrical lens, which is commonly used in LSFM. The intensity of the light sheet can be expressed according to equation 1.7. The FOV is the region over which the illumination sheet thickness is no more than  $\sqrt{2}$  times its waist ( $\omega_o$ ), and the length of this region is 2 times the Rayleigh length ( $Z_R$ ) of the beam,  $Z_R = n\pi\omega_0^2 / \lambda_{EX}$ . The beam waist can be estimated using  $\omega_o = \lambda_{EX} / 2NA_{EX}$ .

$$I(x, y, z) = |A_0|^2 \frac{\tilde{\omega}_x}{\omega_x(y)} \cdot \frac{\tilde{\omega}_z}{\omega_z(y)} \cdot \exp \left[ -2 \left( \frac{x^2}{\omega_x(y)} \cdot \frac{z^2}{\omega_z(y)} \right) \right] \quad (1.7)$$

However, when the thickness of the light sheet approaches the wavelength of light, the Gaussian approximation becomes inaccurate. In this case, the scalar diffraction theory can be used to estimate the propagation length of the light sheet  $d_{lightsheet} = \lambda_{EX} / n(1 - \cos\theta_{EX})$ [27].

The archetypal lightsheet microscope uses two objective lenses. One of them is the illumination objective lens and the other is the detection lens. In order to fit two objective lenses in the orthogonal position to each other, objective lenses with long working distances are required. High NA objective lenses normally have short working distances and bulky geometrical shapes, which limits the objective lens selection to lower numerical aperture lenses. This is presented in Figure 1.10 (C)-(D).

## 1.8 Configurations of Light Sheet Microscopy

Over the years, many configurations of light sheet microscopes have been developed to improve performance and accessibility for a variety of different applications [144], from imaging spheroid cultures and single cells for the study of sub-cellular dynamics and structures [145, 126], to tracking neurological morphology and neural signals in embryos and larvae [135, 104, 179], and even imaging cleared human organs [62, 195]. Detailing each and every one of these configurations would be outside the scope of this dissertation, but I will provide an overview of the most common configurations in this section. Most of the developments in light sheet microscopy are variations on these few basic configurations.

**L-shape light sheet microscope** This is the initial setup and the most common configuration for LSFM, as shown in Figure 1.11(A). The light sheet is formed using a cylindrical lens [148, 91]. One drawback of this setup is that the resulting image is affected by stripe artifacts from the scattered and absorbed light due to the sample structure. This can be addressed by rotating the sample using a 4-D stage, where the volumetric images of the sample can be captured from different views taken sequentially. These views can be fused together to overcome the limited penetration depth of each view individually, as well as to improve the resolution of the image after deconvolution [192, 151, 177]. As previously discussed, light sheet microscopy involves a compromise between effective field of view and strength of optical sectioning capacity. The imaging depth and quality can be further improved using a DSLM approach [106] where the scanning beam can be synchronized with the confocal slit on the detector [124].

**T-shape light sheet microscope** This is one way to mitigate stripe artifacts without sacrificing imaging speed. In this configuration, instead of illuminating the sample from one side, the sample is illuminated from both (opposite) directions using two illumination objectives, as shown in Figure 1.11(B). Rather than forming one thick light sheet, two thinner sheets are combined to cover the same size field of view. The light sheet can be quickly dithered within the illumination plane, and the resulting image is formed by fusing the two images illuminated from either side. This technique is also termed multidirectional selective plane illumination microscopy (mSPIM) [89]. The techniques used with the L-shape configuration, such as multi-view fusion [135] and DSLM with confocal slit detection [207], can also be used with this configuration. It is very flexible, and many publications have demonstrated its applicability to mid-size and even larger sample sizes including cleared mouse brain [173, 136, 136, 29], mouse bone marrow [26], chicken embryos [37], organs, and even human tissues [62, 52, 195].

**X-shape light sheet microscope** This setup uses four objective lenses. The first implementation of an X-shape light sheet microscope was demonstrated by Krzic et al, and was named multiview SPIM (MuVi-SPIM). It featured two illumination and two detection objective lenses [114]. A set of four image stacks is acquired using combinations of each illumination and detection pair. With this configuration, full 3D coverage of *Drosophila* embryos is achieved using a scanned Gaussian beam; however, improvements to axial resolution still require at least a single rotation of 90 degrees [150, 165]. A confocal enhanced variant of this configuration was later developed by the same group (Medeiros et al [133]).

Tomer et al then implemented a version of the system (simultaneous multi-view light sheet microscopy:SiMView), with one and two-photon excitation [187]. The latest iteration of the four objective light sheet microscope is IsoView, which employs four custom-made objective lenses, allows simultaneous illumination and detection in all four light paths [30], and uses phase-shifted confocal line detection, or a spectral approach by switching between colors in the orthogonal pathways [150]. This system can image volumes at  $0.25 - 2Hz$ . Isotropic resolution of  $1.1 - 2.5\mu m$  can be achieved after deconvolution without any mechanical rotation of the specimen in IsoView, with a field of view at  $800\mu m^2$ . This configuration is most popular for live imaging of small to mid-sized samples such as *drosophila* or zebrafish embryos or larvae.

**V-shape light sheet microscope** This configuration was first introduced by Wu et al [202] in a setup created for imaging *C.elegans*, as shown in Figure 1.11 (D-E). This setup is known as inverted selective plane illumination microscopy (iSPIM), and was built upon a commercial inverted microscope base with a single illumination and a single detection arm. This system has a resolution of 520 nm in the lateral direction and  $1.7\mu m$  in the axial direction. A dual-view version of this microscope was later developed by the same group. With this system (diSPIM), both arms are used for illumination as well as for detection, and an isotropic resolution of  $\approx 300\text{nm}$  is achieved after fusion and deconvolution. [203]. However, the field of view of the diSPIM system is rather limited ( $30\mu m$  [203] to  $60\mu m$  [115]).

Later, another popular V-shaped light sheet configuration, termed Open-top SPIM [130], was introduced. This configuration included a larger field of view ( $300\mu m$ ), though its resolution was compromised (lateral resolution of  $1.1\mu m$  and axial resolution of  $6.2\mu m$ ). In Open-top SPIM, the objective is located underneath the sample, and the system uses a water prism to compensate for the aberrations introduced when imaging at 45 degrees through a coverglass, as shown in Figure 1.11. Currently, the state-of-the-art LSFM setup known as lattice light sheet microscopy (LLSM) [28, 123] also uses this configuration. This will be discussed in detail later in this dissertation. This is different from most LSFM implementations [90], which require specific sample preparations such as embedding a sample in agarose gel and glass capillary tube or a Fluorinated Ethylene Propylene (FEP) tube [199, 103]. The V-shaped configuration works with conventional sample mounting techniques like petri dish, glass slide, and cover slip mountings.

**Reflective illumination/Tilted illumination light sheet microscope** Due to LSFM's geometric constraints, each of the previous configurations is limited to use with an objective lens having an NA less than 1.1 [24, 123, 28]. Gebhard et al addressed this challenge using a pair of opposing objective lenses ( $40\times 0.8$  NA illumination and  $100\times 1.4$  NA detection) and a 45 degree mirrored cantilever [60, 211]. In this setup, the cantilever reflects the light sheet, coaligning it with the focal plane of the detection objective lens. Greiss et al constructed a version of the reflected light sheet microscope (RLSM) with a micro prism [65] instead of a custom-made cantilever ( $20\times$ , 0.95 NA illumination;  $40\times$ , 1.25 NA detection). This concept was further advanced by Single-objective SPIM (soSPIM) [57], where the illumination beam is launched from the detection objective lens, as shown in Figure 1.11h. The image volume is acquired through a combination of scanning and refocusing the light sheet using a galvo scanner and an electric tunable lens (ETL). Many variants of soSPIM have been developed [102, 132, 209]. Recently, Gustavsson et al demonstrated a combination of LSFM with PSF engineering, used to image mitochondria and nuclear lamina in HeLa cells [71]. In this setup, shown in Figure 1.11g, the authors take a different approach from those mentioned above. The illumination light sheet is tilted with a small angle using a  $10\times 0.28$  NA objective lens, rather than being completely parallel to the detection objective ( $100\times 1.4$  NA). This tilted light sheet concept was also employed in the work published by Fadero et al [42], however, in that work a light sheet was created through lateral interference using a photo mask [42]. Ultimately, both versions of the tilted illumination light sheet require a specialised imaging chamber and suffer from spherical aberrations due the refractive index mismatch between the objective immersion media and the specimen.

**Oblique plane illumination light sheet microscope** The oblique plane illumination configuration has gained much attention in recent years. The very first inclined illumination light sheet using one objective lens for both illumination and detection is known as HILO (Highly Inclined Laminated Optical sheet microscopy). HILO was first implemented in single molecule imaging [186]. However, the HILO setup has some disadvantages. Extra scattered light and fluorescence is introduced into the system, and severe defocus on one side results in a limited field of view, with only  $16\ \mu\text{m}$  usable field of view for a  $6\ \mu\text{m}$  thick light sheet. Dunsby et al addresses these issues by adding an extra pair of objective lenses, in order to remote focus [16, 15] the tilted intermediate image onto the camera sensor [38]. A high NA objective lens is used. Because the

angular extent of a high NA objective lens is close to 90 degrees, this approach is called oblique plane microscopy (OPM).

Bouchard et al later developed the swept confocally aligned planar excitation (SCAPE) microscope, combining a scanning galvanometer mirror with OPM. This allowed for the sweeping of the excitation sheet laterally across a sample with a maintained focus on the moving plane [18]. The SCAPE system can achieve a resolution of  $2\ \mu\text{m}$  laterally and  $5\ \mu\text{m}$  axially with a volumetric imaging speed of 10Hz ( $600 \times 650 \times 134\ \mu\text{m}^3$ ). A disadvantage of this approach, however, is that some part of the numerical aperture is sacrificed in the relay system. In order to capture all of the fluorescent light, the third objective lens must have a half opening angle of up to 90 degrees [49]. An air objective lens with 0.95NA (half opening angle of 71 degrees) cannot be sufficiently tiled without colliding with the secondary objective lens. Many variations of this concept have been explored [116, 80, 110, 206]. For example, Kim et al used a mirror to replace the third objective lens, in order to overcome this geometrical constraint [110]. However, the resulting system is not light-efficient due to the use of a 50 : 50 beamsplitter. Yang et al used a different method to overcome the geometrical constraint with better light collection efficiency. They used a higher refracting index medium (water) to compress the angular spread of the fluorescence light, thereby allowing all light to be captured with a water immersion objective lens [206, 49]. This system is able to perform live imaging of HEK 293T cells in multi-well plates with a resolution of 339nm in x, 316nm in y, and 443nm to 596nm in the axial direction over a  $100 \times 70 \times 20\ \mu\text{m}^3$  volume. In addition, this configuration allows for conventional sample mounting, from using multi-well plates to freely moving organisms. However, the resolution of the system remains diffraction-limited and the requirements for aligning the system are rather complex.

## 1.9 Superresolution Microscopy

As discussed earlier, the resolution of the widefield fluorescence microscope is governed by the wavelength of the light and the NA of the system. A straightforward approach to improving the resolution is adjusting the wavelength of the light. Unfortunately, short wavelengths are damaging to biological specimens and do not allow for deep imaging due to scattering. Another method of increasing resolution is to increase the NA of the microscope. However, commonly available high NA objective lenses are limited to a  $\sim 1.4$  NA. This limits standard widefield fluorescence microscopes to a spatial resolution of 200nm in the lateral and 500nm in the axial direction [205]. A microscopic

technique that improves resolution beyond the diffraction limit is classified as a superresolution technique [10]. Several superresolution fluorescence microscopy techniques have been demonstrated to be capable of resolving biological structures or dynamics which are not resolvable with conventional fluorescence microscopy. Most of these methods are based on wide-field or laser point scanning microscopy layouts [205, 164]. A very early example is confocal microscopy, where a laser beam is focused by an objective lens into a small focal spot within a specimen, then an image is acquired point-by-point, by scanning either the specimen or the laser beam. A pinhole is placed in front of the detector at the image plane of the microscope. This ensures that only the light from the geometrical focal point is being captured and the fluorescence light originating from outside the front focal plane of the objective lens is blocked, as shown in Figure 1.12. In theory, if an infinitesimally small pinhole is used, it is possible to improve the resolution by a factor of  $\sqrt{2}$  [169]. In real-world implementation, the pinhole size is often measured in Airy units ( $AU, 1AU=1.22\lambda/NA$ ). As there is a trade-off between the size of the confocal pinhole and the resulting signal, a pinhole size of about 1AU is often used. Therefore, this approach mostly enhances optical sectioning [141] rather than actually achieving superresolution. Stimulated emission and depletion (STED) [78, III, 21], stochastic optical reconstruction microscopy (STORM) [160, 87], photoactivated localization microscopy (PALM) [10, 127], and structured illumination microscopy (SIM) [68, 70] were later developed to improve transverse and axial resolutions beyond the diffraction limit. Here, each of the techniques favors a different aspect of the imaging condition, for example, resolution, speed, photo-damage, imaging depth, etc.

## 1.10 Stimulated Emission Depletion Microscopy

The concept of Stimulated Emission Depletion Microscopy (STED) was first proposed in 1994 [78] and was later demonstrated experimentally in 1999 [111]. This method can typically achieve a resolution of 20-60nm. Similar to confocal microscopy, STED uses a laser point scanning layout. In addition, it builds upon the phenomenon of stimulated emission, where an excited-state fluorophore encounters a photon that matches the energy difference between the excited and the ground state [86], causing stimulated emission and suppressing the fluorescence emission. In STED microscopy, this suppression of fluorescence occurs in an annulus centered on the excitation beam. In this way, the overall PSF is reduced and the resolution of the imaging system is enhanced. However, the pattern is also limited by diffraction. In order to achieve superres-

olution, the STED laser pattern needs to have a zero intensity at the center and a nonzero intensity at the periphery. This is shown in Figure 1.13. This means that the depleted population is non-linearly dependent on the STED laser intensity as the saturated depletion level is approached. If the STED laser's local intensity exceeds a certain level, essentially all spontaneous fluorescence emission is suppressed [86]. In STED microscopy, the spatial resolution depends on the size of the zero-intensity volume of the fluorescence suppression beam, rather than on the diffraction. The size of the zero-intensity volume of the depletion beam is inversely proportional to its intensity. In this case, the resolution of the STED system is described as

$$d_{\min} = \frac{\lambda}{2NA\sqrt{1 + \frac{I}{I_s}}} \quad (1.8)$$

where  $d_{\min}$  is the full-width half max (FWHM) of the fluorescence spot,  $\lambda$  is the wavelength of the light used to excite the sample, NA is the numerical aperture of the objective lens,  $I$  is the depletion laser intensity, and  $I_s$  is the saturation intensity of the fluorescence molecule.  $I_s$  is dependent on the absorption cross-section and the lifetime of the fluorescent state [75]. The STED depletion pattern is typically generated using a phase mask in the illumination path. A semi-circular  $\pi$ -shift phase mask is used or a phase vortex is created with a circularly polarized beam, which is used to improve the resolution in the lateral direction. In the axial direction, axially confined patterns are created through a  $\pi$ -shift with a circularly polarized beam. A detailed review of different depletion patterns can be found in Ref [178].

To achieve high resolution with STED, the excitation volume must be very small. Therefore, as resolution requirements increase, the time that is necessary to scan each sample also increases. The speed of imaging with STED can be optimized by imaging only the region of interest, as with confocal microscopy. Recent developments in the area of STED microscopy have focused on improving imaging speed or depth. However, due to STED's complexity and the requirement that the two beams be precisely aligned, its application is currently limited to specialized areas, usually in research that involves small, thin samples. Researchers aim to expand the application of STED by using adaptive optics to correct the aberrations from the samples, to increase its capability to thicker samples [191], and to increase the imaging speed using simultaneous excitation patterns [11, 129].

## 1.11 Single Molecule Localization Microscopy

Single-molecule localization microscopy (SMLM) is another group of super-resolution techniques which use a stochastic approach to allow a small subset of isolated fluorescent molecules to be switched on at a particular moment while the majority of the molecules remain in a nonfluorescent, or dark, off state. The fluorescent signals emitted by these single fluorescent probes are captured by a camera, forming individual emission patterns, which are essentially PSFs. The centers of these PSFs can then be pinpointed with high precision [122]. A final image is reconstructed by localizing thousands to millions of such single-molecule emission events. This is illustrated in Figure 1.14. SMLM imaging can achieve a 20-40 nm resolution in the focal plane [122]. This gives it the highest resolution among all three categories of superresolution methods. SMLM includes photoactivated localization microscopy (PALM) [10, 127, 79], stochastic optical reconstruction microscopy (STORM) [160], direct STORM (dSTORM) [73], ground state depletion and individual molecule return (GS-DIM) [51], and DNA-base point accumulation for imaging in nanoscale topography (DNA-PAINT) [157]. Localization approaches can be extended to 3D imaging [100, 81, 189, 140]. The very first implementation of 3D SMLM used a cylindrical lens in the imaging path, so that the shape of the single-molecule image (PSF) varies at different axial positions within the focal volume and the 3D position of the molecule can be localized based on the centroid and ellipticity of the PSF [87, 85]. More recently, additional approaches have been developed, pushing the limits of the 3D imaging range, for example, using a double-helix PSF [147], self-bending PSF [96], and tetrapod PSF [168, 71]. Improvement can be made in the precision of localization, for example, by using interferometric detection techniques like iPALM [171] or 4Pi-SMS [6, 88], by using supercritical-angle fluorescence recovery [19, 35], or by using patterned illumination [7, 67]. Additionally, this approach can be applied to imaging of thick samples by incorporating adaptive optics [181, 182, 23], or by using using confocal or light sheet illumination [71, 196]. Typically, the resolution of 3D SMLM is about 50 to 80 nm in the axial direction [122].

## 1.12 Structured Illumination Microscopy

Structured illumination microscopy (SIM) was first demonstrated in the context of optical sectioning by Neil et al in 1997 [141]. This concept was extended to improve the resolution by a factor of two, surpassing the conventional resolution limit [153, 68]. This improved-resolution SIM is often referred to as SR-

SIM. Compared with other superresolution methods, SR-SIM offers a more modest improvement in resolution ( $\sim 100\text{nm}$ ), but with faster imaging speed, higher signal-to-noise ratio, and gentler treatment of the sample. This makes it the best choice for live imaging applications.

**2-D SR-SIM** The principle of SIM is based on the Moiré effect, which is an optical phenomenon where a lower frequency beat pattern is created by the interference of two finer patterns. In SIM, this is realized by illuminating the sample with a striped pattern. This way, the higher-frequency information, which is normally limited by the passband of the optical system, is mixed into the acquired images at lower spatial frequency. Therefore, the information from the sample can be calculated with knowledge of the illumination pattern. Here, the image actually conveys a measurement of the distribution of fluorescence markers. This can be described by the following equation 1.9.

$$I_{em}(\mathbf{r}) = (I_{ex}(\mathbf{r}) \cdot S(\mathbf{r})) \otimes PSF \quad (1.9)$$

Multiplication in the spatial domain is equivalent to convolution in the Fourier domain. Because the Fourier transform pair of the sin or cos function is  $A[\delta(\omega - \omega_o) \mp \delta(\omega + \omega_o)]$ , and  $I_{ex}$  is described as follows,

$$I_{ex}(\mathbf{r}) = I_o [1 + \cos(\mathbf{k}_o \cdot \mathbf{r} + \phi)] = I_o [1 + 0.5 (e^{i(\mathbf{k}_o \cdot \mathbf{r} + \phi)} + e^{-i(\mathbf{k}_o \cdot \mathbf{r} + \phi)})] \quad (1.10)$$

and because the Fourier transform of  $E(\mathbf{r}) = I_{ex}(\mathbf{r}) \cdot S(\mathbf{r})$  becomes equation 1.11, this means that when sinusoidal patterned illumination is used, the sample information will be shifted and superimposed.

$$\tilde{E}_{em}(\mathbf{k}) = I_o [\tilde{S}(\mathbf{k}) + 0.5\tilde{S}(\mathbf{k} + \mathbf{k}_o)e^{i\phi} + 0.5\tilde{S}(\mathbf{k} - \mathbf{k}_o)e^{-i\phi}] \quad (1.11)$$

The direction of the shift is defined by the stripe direction of the pattern, and the amount of the shift is defined by a distance proportional to the inverse line spacing of the pattern  $k_o$  [68]. Because the coefficients of the sum 1.11 depend on the  $e^{i\phi}$ , the shifted and superimposed  $\tilde{D}_{\pm k_o} = OTF * \tilde{S}(\mathbf{k} \pm \mathbf{k}_o)$  can be separated using a simple linear equation as follows.

$$\begin{bmatrix} \tilde{D}_o \\ \tilde{D}_{\mathbf{k}+\mathbf{k}_o} \\ \tilde{D}_{\mathbf{k}-\mathbf{k}_o} \end{bmatrix} = \frac{1}{3} \begin{bmatrix} 1 & 1 & 1 \\ e^{i\phi_1} & e^{i\phi_2} & e^{i\phi_3} \\ e^{-i\phi_1} & e^{-i\phi_2} & e^{-i\phi_3} \end{bmatrix} \begin{bmatrix} \tilde{I}_{em\phi_1} \\ \tilde{I}_{em\phi_2} \\ \tilde{I}_{em\phi_3} \end{bmatrix} \quad (1.12)$$

Illumination patterns with phases of 0,  $2\pi/3$ , and  $4\pi/3$  are often used. In order to have transversely isotropic resolution, the illumination pattern must

be rotated and multiple images must be taken for each orientation (commonly, three orientations are required, as shown in Figure 1.15). The final reconstructed image is obtained through equation 1.13

$$I_{\text{sr}} = \frac{OTF(\mathbf{k}+\mathbf{k}_o)\tilde{S}(k+\mathbf{k}_o)+OTF(\mathbf{k}-\mathbf{k}_o)\tilde{S}(k-\mathbf{k}_o)+OTF(\mathbf{k})\tilde{S}(k)}{|OTF(k+\mathbf{k}_o)|^2+|OTF(k-\mathbf{k}_o)|^2+|OTF(k)|^2+w^2} \quad (1.13)$$

**3-D SR-SIM** SIM was further developed in a three-dimensional context, to extend resolution in the axial and lateral directions, by Gustaffson et al [70]. The following equation describes the general form of the illumination beam. The pattern comparison between 2-D SR-SIM and 3-D SR-SIM is shown in

$$I_{\text{ex}}(\mathbf{r}_{\text{xy}}, z) = \sum_m I_{\text{ex}_m}(z)J_{\text{ex}_m}(\mathbf{r}_{\text{xy}}) \quad (1.14)$$

According to Ref [70], three major conditions must be fulfilled in order to acquire images that contain super-resolution details: 1) the illumination pattern must be the sum of separable lateral and axial components, 2) the lateral functions  $I_{\text{ex}_m}$  should only consist of a single frequency, and 3) the illumination pattern must be fixed in relation to the focal plane of the microscope. In 3-D SIM, a three-dimensional lattice is created by the interference of three beams. The Fourier transform of the captured data can be expressed as

$$\tilde{D}(\mathbf{k}) = \sum_m O_m(\mathbf{k}) \left[ \tilde{S}(\mathbf{k}) \otimes \tilde{J}_{\text{ex}_m}(\mathbf{k}_{\text{xy}}) \right] \quad (1.15)$$

In this equation,  $J_{\text{ex}_m}$  is a simple harmonic which means that its Fourier transform is equal to  $\sum_m \delta(\mathbf{k}_{\text{xy}} - p_m)e^{i\phi_m}$ .  $\phi$  is the initial phase value of the harmonic  $m$ , and  $p_m$  defines the distance of the shifted object information  $\tilde{S}$  in the reciprocal space. Here,  $p_m = mp$  is a multiple of the fundamental frequency. As indicated above, the structure of the object can be solved for using a  $N \times N$  matrix. Here, the number of images acquired with  $N$  different pattern phases is equivalent to the number of harmonic components. For 3-D SIM, a minimum of 5 images with illumination pattern phases set at  $0, 2\pi/5, 4\pi/5, 6\pi/5$ , and  $8\pi/5$  are used. Once the frequency components are extracted, the final image can be reconstructed using the equation (11) described in Ref [70]. This process is shown in Figure 1.16. Because resolution improvement depends on the illumination pattern frequency, the extension of the region of support in SIM is also limited in this way. Therefore, the maximum resolution enhancement in all directions (lateral and axial) is limited to  $2x$ .

**NL-SIM** This limit can be further overcome in 2-D by employing non-linearities in the intensity response of the fluorophores (for instance, by saturating their absorption). This way, the resulting emissions include a higher frequency, and a theoretically infinite resolution can be achieved. In reality, only a finite number of frequency components are raised above the experimental noise, which determines the final resolution. This method is known as nonlinear SIM (NL-SIM) [92]. The concept was first studied theoretically under the name of saturated patterned excitation microscopy [76], and the first experimental demonstration was published in 2005, showing that it is possible to obtain a lateral resolution of 50nm with dye-filled polystyrene beads [69]. However, the need for strong saturation of the fluorophores requires a high laser intensity ( $\sim 10\text{MW}/\text{cm}^2$ ) [156], which makes this approach not suitable for biological imaging. This issue was eventually addressed using photoswitchable proteins (under  $10\text{W}/\text{cm}^2$ ) [156]. However, the limited photoswitching cycles due to photobleaching, as well as the need for 63 raw images for each reconstructed image (7 phases, 9 orientations, 945s/frame) makes this method too slow to image most cellular processes [119]. Li et al. use an improved photoswitchable protein, skyran-NS, to improve switching cycles to 710 and reduced the number of raw images down to 25 (5 phases, 5 orientations, 350ms) with a slightly higher laser intensity ( $20 - 100\text{W}/\text{cm}^2$ ). This makes it a viable option for live-cell imaging.

NL-SIM has a unique appeal compared to SMLM and STED. It can achieve a much larger imaging area than SMLM and STED, with a reasonable number of images required to reconstruct a high-resolution image. However, it lacks the main advantages of linear SIM (speed and strength of live-sample imaging over a large field of view with non-specialized labeling). Therefore, linear SIM currently remains the main workhorse of live-cell imaging in most applications. This is due to the improvement in imaging speed of SIM by the implementation of liquid crystal-based spatial light modulators (SLM) [50, 112, 155]. Fiolka et al. created a version of 2-D SR-SIM combined with total internal reflection fluorescence microscopy (TIRF-SIM) using SLM. However, they only demonstrated its resolution improvement on 50nm fluorescent microbeads ( $\sim 91$  nm lateral resolution) and did not report any speed improvement. Kner et al. first demonstrated a TIRF-SIM system that can perform live-cell imaging at a speed of 11 frames per second (fps) using conventional fluorescent labels over  $32 \times 32 \mu\text{m}^2$  FOV [112]. Later, a 3D-SIM version of the same setup was used to image HeLa cells at a speed of 5s per volume [167], and a version with multicolor imaging capability is able to image filopodia and lamellipodia in living neurons at rates of 8.5s per volume. The imaging speed of SIM is further improved to 79 (fps) using a rolling shutter sCMOS camera over a  $16.5 \times 16.5 \mu\text{m}^2$  FOV in 2-D [174].

Since 3-D imaging with SR-SIM involves sequential acquisition of vertical image stacks, this is further limited to imaging of slower dynamics. Abrahamsson et al. combined SR-SIM with multifocus microscopy [3] using a custom-designed grating [2] to increase the 3-D imaging speed of SIM. This concept is also realized using a multi-plane prism [36], and is able to achieve a volumetric imaging speed of 1.3Hz.

**LSFM-SIM** Most SIM systems use epi illumination, and out-of-focus light constrains SIM to imaging mostly thin samples with a FOV less than  $40\text{-}50\ \mu\text{m}$  and axial range less than  $10\ \mu\text{m}$ . TIRF was a solution to this issue, however, TIRF only allows for imaging of a part of the sample close to the coverslip. LSFM addresses this and improves SIM's ability to image thicker samples, such as *Drosophila* embryos and zebrafish embryos. The early combination of light sheet illumination with optical sectioning SIM [141] involved using a coarse illumination pattern (wave length of the illumination pattern less than or equal to  $\lambda/\text{NA}$ ). The striped pattern is created either by a Ronchi grating [22] or by modulating laser intensity in a DSLM configuration [105].

Planchon et al. presented a version of LSFM-SIM using a stepped Bessel-Gauss beam to create a finer excitation pattern [149] with the reconstruction algorithm described in Ref [101]. They imaged live and fixed U2OS cells, LLC-PK1 cells, and HeLa cells with a  $40\text{-}60\ \mu\text{m}$  FOV over a  $40\text{-}50\ \mu\text{m}$  range (0.8NA, excitation and detection objective,  $\sim 300\text{nm}$  resolution in axial and one lateral direction). Later, an improved version of Bessel SR-SIM LSFM was demonstrated by Gao et al. In this setup, unlike in their previous work, an array of seven parallel Bessel-Gauss beams is generated using a diffractive optical element. This microscope has an excitation and detection objective lens pair (0.65NA and 1.1NA). The processing algorithms of 3-D SR-SIM were implemented in this work [58, 59]. They demonstrated the performance of the microscope by imaging live *C. elegans* embryos and *Drosophila* embryos, achieving a volumetric resolution of  $194 \times 238 \times 419\ \text{nm}^3$ . However, the illumination pattern shown here was only one-dimensional.

In 2015, lattice light sheet microscopy (LLSM) was published by a group led by Eric Betzig, under a similar concept to their Bessel SR-SIM LSFM configuration [28]. However, SLM was placed at the conjugated image plane to the excitation objective lens. Then, SLM was used to create optical lattices in two dimensions (both within the xy plane and along the axial direction) and the confinement of the lattice was also optimized through constructive and destructive interference of the light beams. LLSM allows for two operating modes. One uses a dithered interfered light sheet where the system has a resolution of  $230\text{nm}$

in  $x$  and  $370\text{nm}$  in  $z$ . The other operating mode uses a SR-SIM approach to achieve a volumetric resolution of  $150\text{ nm} \times 230\text{ nm} \times 280\text{ nm}$  ( $\leq 100\mu\text{m}$  FOV) with three to five images with phase shifted illumination [201]. The LLSM uses a V-shaped light sheet configuration, which limits the illumination pattern to a single orientation. This causes the system to have a non-uniform resolution in the lateral direction.

Coherent structured illumination LSM (csiLSFM) is another approach that combines light sheet microscopy with SR-SIM. This method, unlike LLSM, achieves a transverse isotropic resolution down to  $100\text{nm}$ . This is accomplished by creating a standing wave pattern using counter propagating beams from two excitation objective lenses. The csiLSFM offers flexibility in controlling the orientation of the illumination patterns. However, the axial resolution is  $8\times$  poorer than the lateral resolution ( $\sim 800\text{nm}$ ). In addition, the pattern generation in a non-common path configuration makes it very sensitive to any perturbation by the sample. This system has not been widely adopted.

### 1.13 Objectives of This Dissertation

The ability to capture large regions of the neural network in living model organisms, such as zebrafish and fruit flies, at a subcellular scale will further advance neurological research. Among all of the available options, LLSM currently is the most suitable choice for this goal. Despite its non-uniform resolution and limited imaging depth ( $\leq 50\mu\text{m}$ ), LLSM is being widely adopted. However, it is most often operated in the dithered mode with a rather strict sample mounting requirement (sample must be adhered to a small  $5\text{mm}$  coverslip). There is currently no approach that effectively combines SR-SIM with light-sheet to achieve isotropic resolution improvement on thick, multi cellular samples. In this project, we aim to provide a microscopy platform that will effectively combine SR-SIM and LSFM. With this system, the user should be able to capture images over an area of the nervous system more than  $100\mu\text{m}$  in larval stage samples at subcellular resolution ( $161$  to  $241\text{ nm}$  in all lateral directions,  $336$  to  $458\text{ nm}$  axial).

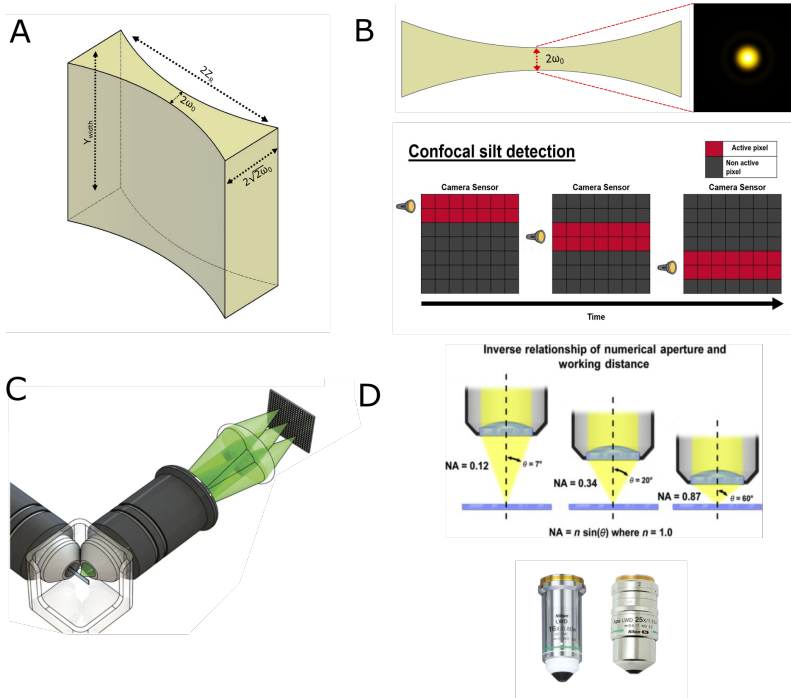


Figure 1.10: (A). Schematics of a light sheet, with the area of  $Y_{\text{width}} \times 2Z_r$  depicting a possible FOV of detection.  $Z_r$  is the extent of the Rayleigh range along the axial direction, i.e., the distance to which the beam waist is increased by a factor of  $\sqrt{2}$ . (B). In scanning light sheet microscopy, the beam scanning speed is synchronized with the rolling shutter of the camera, and the thickness of the beam can be used to estimate the confocal slit width. (C). The archetypal light-sheet microscope: paired, orthogonal optical paths provide plane-wise illumination (blue) and wide-field fluorescence detection (green). (D). Illustration of the relationship between the collection half angle, numerical aperture, working distance of a microscope objective, and comparison of low and high NA objective lenses. (C) is adapted from Ref [150], and (D) is adapted from Ref [158, 25].

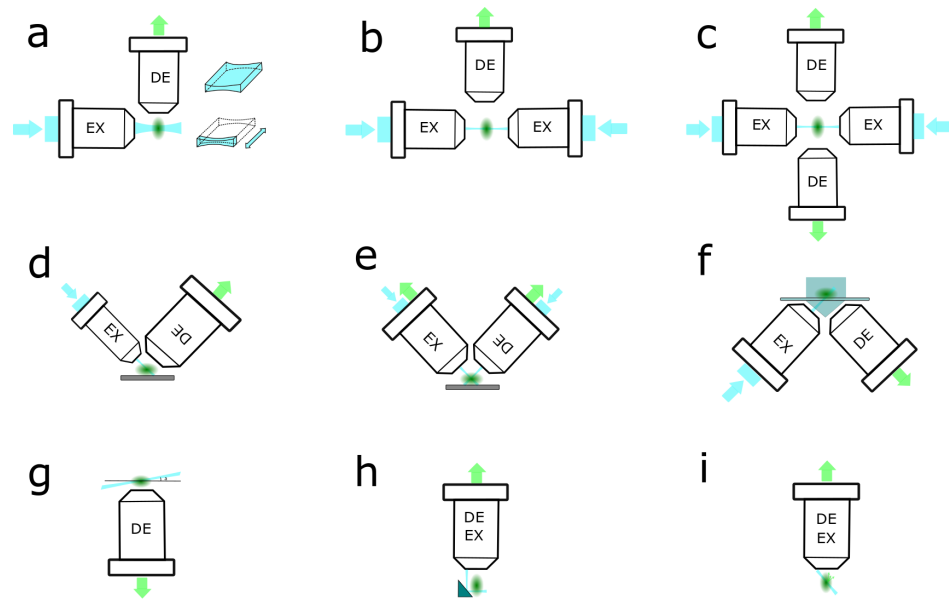


Figure 1.II: LSFM configurations. (a). L-shape LSFM with a single illumination and a perpendicular detection arm. (b) T-shape LSFM with opposite directional illumination arm. (c) X-shape LSFM with four illumination/imaging arms. (d) V-shape LSFM with single illumination arm and detection arm. (e) V-shape LSFM with dual side illumination and detection. (f) V-shape open top LSFM. (g) LSFM with a tilted illumination light sheet. (h) Reflected single objective LSFM. (i) Oblique plane illumination LSFM.

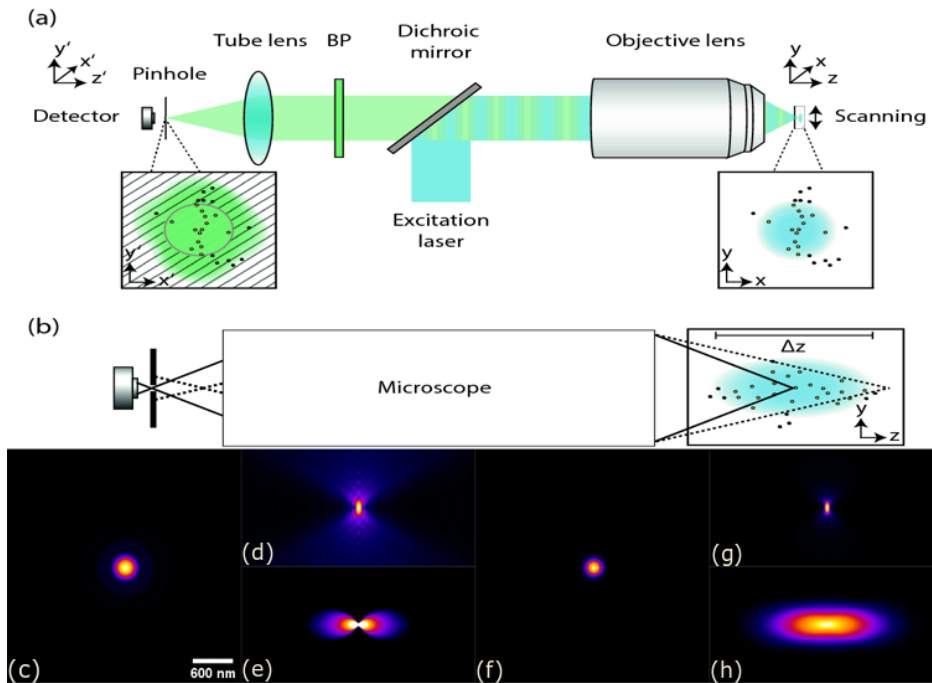


Figure 1.12: Basic confocal microscope layout is shown in (a-b). Simulated three-dimensional point spread functions and corresponding optical transfer functions. (c-e) Wide-field microscope. (f-h) Confocal microscope. In both cases, the numerical aperture of the objective is 1.2 and the refractive index of the medium is 1.333. The wavelength of the emitted light is assumed to be 520 nm. Figure (a-b) is acquired from Ref [40].

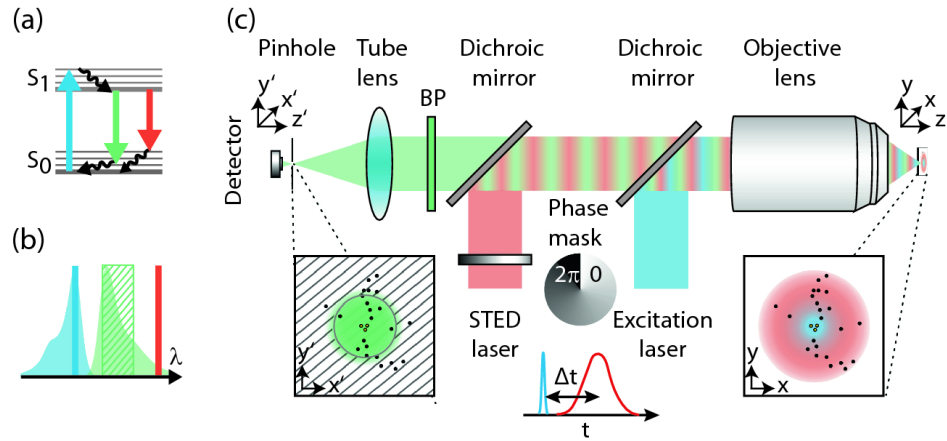


Figure 1.13: The principle of stimulated emission depletion (STED) microscopy. (a) Jablonski diagram of a fluorescent molecule. In addition to the processes of excitation and spontaneous emission, stimulated emission is now used to switch off excited molecules in a targeted way. (b). Absorption and emission spectrum of a fluorescent molecule. The depletion laser is shifted to the far right of the emission spectrum of the fluorophore. (c). In comparison to the confocal microscope, an additional depletion laser is now superimposed with the excitation beam. A helical phase mask imprints a phase retardation from  $0-2\pi$  onto the STED beam, that when imaged into the sample plane, creates a doughnut-shaped depletion pattern. The right inset shows the overlap of the excitation and STED beams in the focal plane. Wherever the STED intensity is sufficiently high, excited fluorophores are driven into their off-state. Therefore, fluorescence is only emitted from sample regions where the STED intensity is negligible. This fluorescence is separated from the laser light and imaged onto a point-detector. Most STED microscopes utilize pulsed lasers for excitation and depletion. The central inset illustrates that a time delay between the excitation and STED pulses is necessary for effective suppression of the fluorescence. Figure is reprinted from Ref [40].

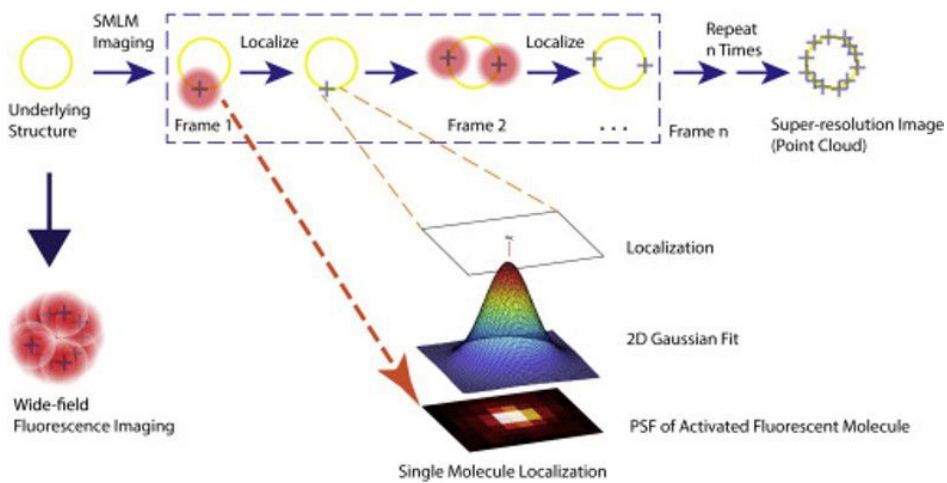


Figure 1.14: The principle of single molecule localization microscopy (SMLM). Labeling the yellow circle (i.e., a biological structure below the diffraction limit) efficiently with fluorescent dye to be imaged with a fluorescence microscope. The conventional diffraction-limited wide-field microscope produces a blurred image. SMLM imaging produces a super-resolved image that is constructed from a set of time-separated images, where in each time frame image, a sparse set of excited labeled proteins can be localized using Gaussian PSF to form the final point-cloud super-resolution image of the structure. Figure is reprinted from ref [109].

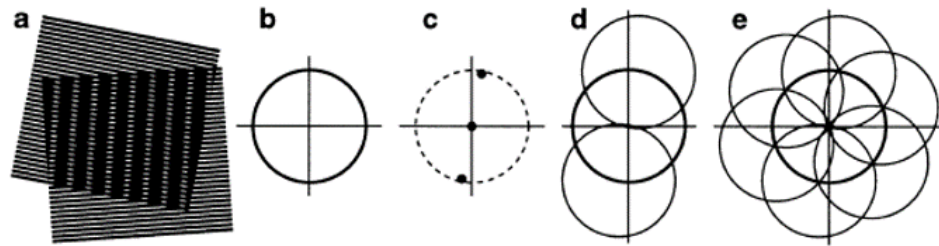


Figure 1.15: Concept of resolution enhancement by structured illumination. (a) If two line patterns are superposed (multiplied), their product will contain Moiré fringes (seen here as the apparent vertical stripes in the overlap region). (b) A conventional microscope is limited by diffraction. The set of low-resolution information that it can detect defines a circular ‘observable region’ of reciprocal space. (c) A sinusoidally striped illumination pattern has only three Fourier components. The possible positions of the two side components are limited by the same circle that defines the observable region (dashed). If the sample is illuminated with such structured light, Moiré fringes will appear, representing information that has changed position in reciprocal space. The amount of that movement corresponds to the three Fourier components of the illumination. The observable region will thus contain, in addition to the usual information, moved information originating from two offset regions (d). From a sequence of such images, with different orientations and phases of the pattern, it is possible to recover information from an area twice the size of the normally observable region, corresponding to twice the normal resolution (e). Figure acquired from Ref [68].

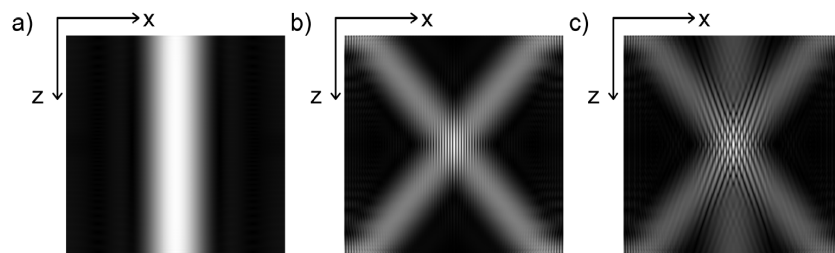


Figure 1.16: Comparison of the illumination patterns between (a) the WF microscope, (b). 2D SR-SIM microscope, and (c). 3-D SR-SIM microscope. This image is acquired from Ref [70, 163].

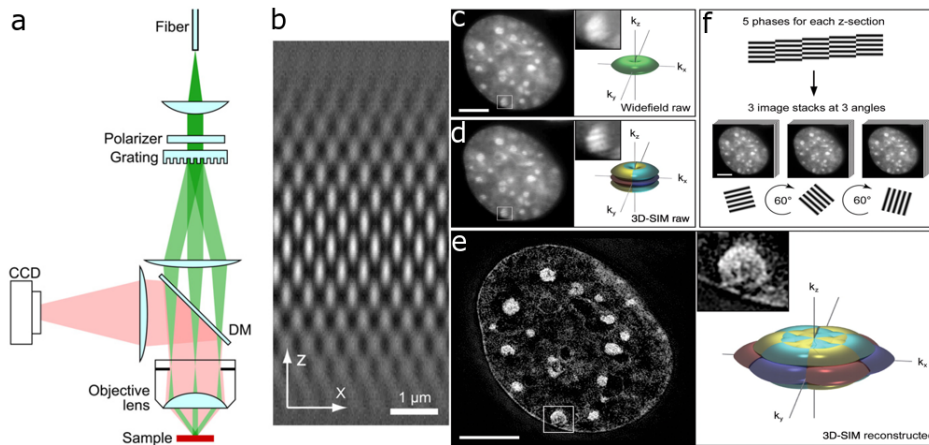


Figure 1.17: (a) Simplified diagram of three-dimensional structured illumination microscope. (b). Three-dimensional lattice is generated using three beam interference. Cross section through a DAPI-stained C<sub>2</sub>C<sub>12</sub> cell nucleus acquired with conventional wide-field illumination (c) and with structured illumination (d). The same cross section of the reconstructed 3D-SIM image, showing enhanced image details, is shown in (e). The increase in resolution is shown in frequency space on the right, with the coverage extending two times farther from the origin. Scale bars indicate 5 μm. (f). Five phases of the sine wave pattern are recorded at each z position, allowing the shifted components to be separated and returned to their proper locations in frequency space. Three image stacks are recorded with the diffraction grating sequentially rotated into three positions 60° apart, resulting in nearly rotationally symmetric support over a larger region of frequency space. This image is acquired from Ref[70, 163]

# CHAPTER 2

## ZEBRAFISH NEURAL IMAGING WITH LIGHT SHEET MICROSCOPY

A fundamental problem in biomedical science is understanding the 3D structure of the brain and other organs at the cellular level. Large, thick specimens and live model organisms such as zebrafish, *C. elegans*, and *D. melanogaster* are widely used for studying organ development, human diseases and the nervous system. A central goal of modern neuroscience is to obtain a mechanistic understanding of higher brain functions under healthy and diseased conditions [54]. Zebrafish is a vertebrate organism that holds promise for understanding brain function and neurological disorders, due to its small size and transparency at larval stages. Further, zebrafish offer a wide range of genetic tools and advantages for neurophysiological approaches [54].

Several groups have demonstrated the superior high temporal performance of light sheet systems in both 2D and 3D [4, 146, 45]. Various configurations of LSFM have been developed and applied to different sizes of samples. These include single cell imaging [71, 132, 83], small multicellular samples such as *C. elegans*, *D. melanogaster*, and zebrafish embryos [91, 58, 187], samples which are hundreds of microns in size such as *C. elegans* [143] and zebrafish larvae [4], and even samples up to a few centimeters in size such as whole mouse embryos [37] and human prostate tissue [62]. Even though LSFM provides a high temporal resolution and excellence in optical sectioning, the resulting images are greatly affected by the thickness of the sample, especially when applied to large and semi-opaque samples. Scattering introduces extra background light into the resulting image, which leads to a lower signal to noise ratio (SNR) and reduced contrast.

A number of methods have been proposed to address this issue, such as using the non-diffracting Bessel [45, 149, 43] and Airy [193, 208] beams for excitation. Unfortunately, the side lobes of the Bessel and Airy beams also introduce extra out-of-focus light, which worsens the sectioning performance of the system. Using confocal slit detection or two-photon excitation in conjunction with a Bessel or Airy beam can help minimize this problem. However, because these measures result in a higher light dose on the sample, they also result in an increased rate of photo bleaching and increased risk of photodamage to the sample [150][24]. An alternative approach is combining structured illumination microscopy (SIM) [141] with LSFM. SIM was first employed in conventional widefield fluorescence microscopy as an optical sectioning method which works by projecting a sinusoidal illumination pattern onto the sample and reconstructing the optically sectioned image using three images with a phase difference of  $2\pi/3$ [141]. SIM has been combined with LSFM by replacing the light sheet created by a cylindrical lens with a scanned Gaussian or Bessel beam that can be modulated to create an SI pattern [149, 22, 105, 84]. This approach is referred to as digitally scanned light sheet microscopy (DSLIM). For optical sectioning, the three sinusoidal patterns are most commonly combined using the root mean square (RMS) reconstruction algorithm [141]. HiLo microscopy has also been combined with LSFM as an alternative reconstruction algorithm [134, 166]. Previously, we have shown that combining the SIM images using a linear reconstruction algorithm (LR-SI) produces images with a flatter frequency response and better image fidelity at low signal intensities [183]. In this study, we combine LR-SI with DSLIM [108]. LR-SI has previously been combined with LSM to study early stage *C. elegans* embryos and other samples with linear dimensions of  $\sim 50\mu\text{m}$  or less [58]; here, we apply LR-SI to zebrafish larvae with a lateral dimension of  $\sim 500\mu\text{m}$ . Additionally, we combine digital scanning and structured illumination (SI) with electronic confocal slit detection (eCSD) [148]. This approach achieves a final optically sectioned image with a signal to noise ratio 5.6 times higher than the RMS method, while using the same number of frames. We evaluate the performance of our DSLIM system comparing RMS-SI and LR-SI with different parameters, imaging fluorescent bead phantoms and thick biological samples (zebrafish larvae), and comparing the contrast enhancement. We apply this approach to imaging neural activity in PTZ treated 7 day post fertilization (dpf) zebrafish larvae using a GCaMP indicator and demonstrate two-color imaging at 7 frames per second.

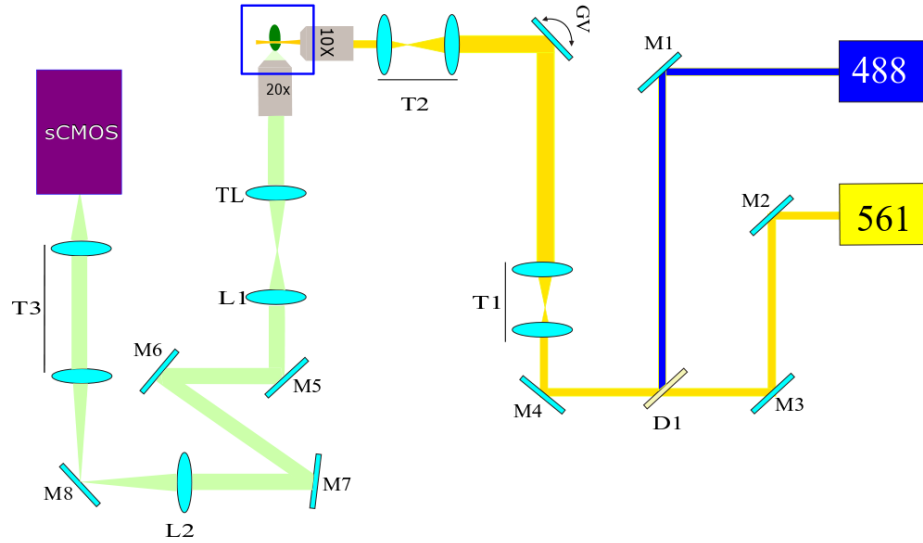


Figure 2.1: Optical setup of the system. A  $10\times 0.3\text{NA}$  water dipping objective is used as the illumination objective lens and a  $20\times 0.5\text{NA}$  water dipping objective is used as the detection objective lens. M1-8: Mirrors; D1, Dichroic Mirror; T1:  $2\times$  magnification lens pair (25mm and 50mm efl); T2  $5/3$  demagnification lens pair (50mm and 30mm); T3  $2/3$  demagnification lens pair (300mm and 200mm efl); TL: Tube lens (180mm efl); L1-2: Relay lenses ( $f_1=100$  or 80mm;  $f_2=200$ mm); GV: 2-axis galvo mirror.

## 2.1 Optical System Design

The system, shown in Fig.2.1, is a modified version of the Open design SPIM [33]. The system described here was developed to image zebrafish larvae expressing the GCaMP<sub>5</sub> calcium indicator and red fluorescent protein (RFP). We use two lasers, a 488nm laser (Coherent OBIS LX 50mW) and a 561nm laser (Coherent OBIS LS 50mW) to sequentially excite the fluorescence. The lasers are combined by a dichroic mirror (Thorlabs DMLP505T) for multi-color imaging, and they co-propagate into the sample. First, a telescope lens pair expands the laser beam by a factor of two. The beam is then directed onto a dual-axis galvo-mirror scanner (Thorlabs GVSM002). After the galvo-mirror scanner, the light passes through a  $0.6\times$  reducing telescope lens pair which re-images the galvo onto the back pupil of the illumination objective lens (Olympus UMPLFLN10  $\times/W$  3.3mm WD, 0.3NA). The light forms a Gaussian beam with a  $6.5\mu\text{m}$  FWHM waist at the focal plane of the objective which is scanned to form a

scanning light sheet. The detection objective lens (Olympus, UMPLFLN 20 $\times$ /W, 3.3 mm WD 0.5NA) collects the fluorescent light, and the image formed by the tube lens (Olympus U-TLU 180mm efl) is relayed by two 4f systems onto the sCMOS camera (Hamamatsu Orca Flash 4.0v2). The final magnification of the system is 33.3 by using a 80mm focal length lens as L<sub>I</sub>. The back pupil plane of the imaging objective lens is projected onto deformable mirror (M6, 4.4mm clear aperture). The 33.3 magnification gives an effective pixel size of 195nm and FOV of 399.36 $\mu$ m. A multi-bandpass filter (Semrock FFO1-514/605/730 – 25) is placed in front of the camera. The two relay systems serve to both increase the magnification and provide access to the back pupil plane for an Adaptive Optics system, which will be discussed in Chapter 4. The sample holder is placed in a 4D translation stage (Picard industries USB 4D-STAGE) so that the sample position can be adjusted relative to the illumination and detection unit. We use the stage translation approach to acquire 3D data. The sample is moved along the z-axis of the detection objective lens and a series of cross-sectional images of the sample are captured. The galvo scanner is driven by a saw-tooth voltage waveform using a DAC shield (Digilent Analog Shield) and Arduino microcontrollers. The light sheet mode of the camera was used, in

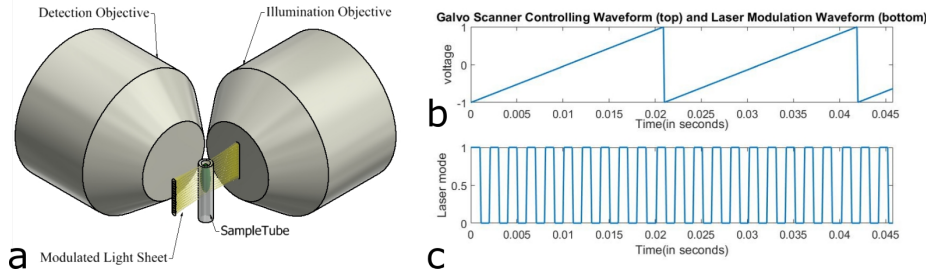


Figure 2.2: Implementation of DSLM-SI. (a) Illustration of the structured illumination light sheet configuration. (b) Controlling waveform of the galvo scanner for a  $500 \times 500 \mu\text{m}^2$  field of view (FOV). (c) The laser modulation waveform with  $k_0 = 0.0427 \mu\text{m}^{-1}$  is shown.

which lines of pixels are read from the top of the sensor to the bottom. Fig.2.2 shows the sawtooth waveform which is used to drive the galvo scanner. This wave form is synchronized with the signal generated by the rolling shutter of the camera. The width of the rolling shutter is set to the full width half maximum (FWHM) of the Gaussian beam in pixels. This way, only the activated area of the sensor is illuminated, and the background light is further decreased. The laser beams are alternately turned on for each vertical scan so that information from both channels is acquired in an interleaved manner. For high-speed, large field of view functional imaging, the exposure time for each pixel line is set to  $1\mu\text{s}$  and a  $19\mu\text{s}$  delay occurs between each line exposure. A delay of 0.73 ms

between each vertical scan is also added. By using 1024 lines of pixels, we are able to achieve a 20.96 ms interval time between each frame, corresponding to 23.57 frames per second (fps) imaging speed for two channels. The system has a resolution of 510nm laterally and  $4.1\mu\text{m}$  axially in the green channel. For the purpose of enhancing the optical sectioning power of the system, we tested various sets of TI lens pairs ( $2\times$ ,  $3\times$ , and  $5\times$  magnifications). This allows us to change the effective NA of the illumination objective lens, so that we can obtain a thinner sheet (FWHM:  $7\mu\text{m}$ ,  $4\mu\text{m}$ ,  $2.8\mu\text{m}$ ), shown in Fig.2.3. The microscope is controlled through a Dell precision 5810 Tower with 32GB RAM and custom-developed LabVIEW program. The synchronization signal is achieved through two Arduino microcontroller boards and a chipKit u32 microcontroller board with a DAC shield. One of the Arduino boards is equipped with DAC shield which is responsible for controlling the galvo scanner. The interrupt pin of the board is connected to the h-sync signal of the camera, allowing for the synchronization of the beam position. The other arduino board is responsible for counting the pixel line number and modulating the laser on/off state.

## 2.2 Structured Illumination and Image Reconstruction

The structured illumination pattern is formed by modulating the illumination laser beam. As the laser beam scans along the y-axis of the detection objective lens's focal plane, an Arduino microcontroller is used to digitally modulate the laser intensity to create the SI pattern. This approach allows us the flexibility to rapidly change the SI frequency so that the optimum optical sectioning power can be achieved. We acquire three images sequentially for each channel with a pattern phase difference of  $2\pi/3$  between sequential images.

After acquiring images of the sample, we employ both the RMS method [25] and the LR-SI method [31] to reconstruct the optically sectioned images [141]. The RMS method is given by Eq. 2.1, the wide field (WF) image is given by Eq. 2.2, and the LR-SI image is given by Eqs. 2.4 or 2.5.

$$I_{sectioned} = \sqrt{(I_{\varphi_1} - I_{\varphi_2})^2 + (I_{\varphi_2} - I_{\varphi_3})^2 + (I_{\varphi_1} - I_{\varphi_3})^2} \quad (2.1)$$

$$I_{wf} = \frac{1}{3} (I_{\varphi_1} + I_{\varphi_2} + I_{\varphi_3}) \quad (2.2)$$

In the LR-SI method, the shifted copies of the  $\tilde{D}_{\pm k_0}(\vec{k})$  can be separated with Eq. 2.3, in which  $\varphi_1 = 0$ ,  $\varphi_2 = 2\pi/3$ ,  $\varphi_3 = 4\pi/3$  and  $\mathcal{F}^{-1}\{\}$  stands for inverse Fourier transform.

$$\begin{bmatrix} D_0 \\ D_{+k_0} \\ D_{-k_0} \end{bmatrix} = \frac{1}{3} \begin{bmatrix} 1 & 1 & 1 \\ e^{i\varphi_1} & e^{i\varphi_2} & e^{i\varphi_3} \\ e^{-i\varphi_1} & e^{i\varphi_2} & e^{i\varphi_3} \end{bmatrix} \begin{bmatrix} I_{\varphi_1} \\ I_{\varphi_2} \\ I_{\varphi_3} \end{bmatrix} \quad (2.3)$$

$$I_{LR-SI_{nonzero}} = \mathcal{F}^{-1} \left\{ \frac{[\tilde{H}^*(\vec{k})\tilde{D}_0(\vec{k}) + \tilde{H}^*(\vec{k}+\vec{k}_0)\tilde{D}_{+k_0}(\vec{k}+\vec{k}_0) + \tilde{H}^*(\vec{k}-\vec{k}_0)\tilde{D}_{-k_0}(\vec{k}-\vec{k}_0)]}{[|\tilde{H}(\vec{k})|^2 + |\tilde{H}(\vec{k}+\vec{k}_0)|^2 + |\tilde{H}(\vec{k}-\vec{k}_0)|^2 + w^2]} \right\} \quad (2.4)$$

The scattering component of the signal is heavily concentrated near zero spatial frequency. Therefore, to remove the scattering, we can calculate the LR-SI reconstruction without the zero-order term, Eq. 2.5. This method will be referred to as LR-SI-non.

$$I_{LR-SI_{nonzero}} = \mathcal{F}^{-1} \left\{ \frac{[\tilde{H}^*(\vec{k}+\vec{k}_0)\tilde{D}_{+k_0}(\vec{k}+\vec{k}_0) + \tilde{H}^*(\vec{k}-\vec{k}_0)\tilde{D}_{-k_0}(\vec{k}-\vec{k}_0)]}{[|\tilde{H}(\vec{k}+\vec{k}_0)|^2 + |\tilde{H}(\vec{k}-\vec{k}_0)|^2 + w^2]} \right\} \quad (2.5)$$

The parameter  $w$  in Eq. 2.4 and Eq. 2.5 is manually adjusted to achieve the optimal reconstructed image. The reconstruction algorithm is programmed using Python with additional packages including Numpy and Scipy.

## 2.3 Beads Sample Preparation

We use dye phantoms, sub-diffraction fluorescent beads and biological samples to test the performance of our system. For fluorescent dye phantom preparation, first we mix the dye with DMSO into a 1.3mM stock solution, then dilute the stock fluorescent dye (ThermoFisher scientific Alexa Fluor 488 or Alexa Fluor 568) in 0.2% agar in the ratio of 1 to 500. We then load the mixed solution into a FEP tube (Valco-TFEP 130; OD 1.59mm, ID 0.76mm) for imaging. Both ends of the tube are plugged with 3% agar gel.

We prepare bead phantoms with different sizes of beads. Here, 200nm yellow-green (ThermoFisher Scientific F8811) fluorescent beads, 200nm red fluorescent beads (ThermoFisher Scientific F8810) and 1 $\mu$ m yellow-green fluorescent beads (ThermoFisher Scientific F8823) are used. The beads are first diluted with DI water (18.2 M $\Omega$ /cm) in a ratio of 1:1000 separately as stock solutions. We mix the stock together with 0.2% agar gel in a ratio of 20 to 1. Then, we inject the agar bead solution into an FEP tube and plug both ends of the tube with 3% agar gel.

## 2.4 Zebrafish Sample Preparation

We imaged 3 different samples– wildtype, wildtype treated with PTZ, and a *gad1b* null mutant. The genotype of the wildtype fish is *elavl3:GCaMP5g; gad1b:RFP;mitfa<sup>w2/w2</sup>*. Here, we followed the protocol described in [199]. The transgenic zebrafish larvae were paralyzed with alpha-bungarotoxin ( $125.25\mu\text{M}$   $\alpha$ -BTX). For fish that were not already genetically mutated to experience abnormal neural events, additional 15mM PTZ was added to the environment to induce the abnormal neural condition. For fixed samples (structural imaging), samples were bathed in diluted tricane solution, which consists of 0.4% tricane solution that has been diluted with E3 media in a ratio of 42 to 1000. The fish were then placed in a 0.2% agarose solution mounted in the FEP tubing. Both ends were plugged with 3% agar gel.

## 2.5 Data Analysis

We calculated the signal-to-background ratio (SBR) and SNR for both the beads image and the sample image across all methods. For the beads images, we first calculated the background value using the mean intensity value of five different dark, featureless regions (5050 pixels) around the image. The noise is calculated by taking the average of the standard deviations from the above five regions. The signal is calculated by taking the maximum intensity in each of five randomly selected regions of interest (ROI), each  $20 \times 20$  pixels, and then dividing by the background value to produce a ratio. For the biological sample images, we applied the same method. The difference was only that the ROIs were larger ( $200 \times 200$  pixels), and the backgrounds were also larger ( $500 \times 500$  pixels). For the functional data analysis, Fig. 2.6, the intensity value of each time point is the sum of all pixels of the ROI. The background value is established by averaging the intensity value over a 10 second period where no intensity fluctuation is observed and the noise is the standard deviation over the period. The signal to background ratio is calculated by taking the peak intensity over the background value, and the SNR is calculated using the peak intensity over the noise.

## 2.6 Results and Discussion

In LSFM, the thickness of the sheet is directly related to the optical sectioning performance of the system. A thinner beam will introduce much less out-of-focus light into the system and allow us to achieve a higher z-axis resolution. The thinner beam is also directly related to the modulation depth of the SI

pattern because the ideal sectioning strength corresponds to a spatial frequency  $k_0 = \frac{NA}{\lambda}$ . For our system, the ideal SI pattern wavelength is  $\sim 1\mu\text{m}$ , smaller than the Gaussian Beam Waist. Therefore, a thinner beam will allow us to achieve much better contrast. Fig. 2.3 shows different beam profiles for different amounts of initial magnification of the 488 nm laser. The Rayleigh length of the beam is directly proportional to the square of the beam waist ( $Z_R = \frac{\pi w_0^2}{\lambda}$ ), which means that the FOV is inversely proportional to optical sectioning strength. Three different beam waists were tested (BM1, BM2, and BM3) by expanding the laser beam by  $2\times$ ,  $3\times$ , and  $5\times$  using different lenses in the Ti lens pair in Fig. 2.1. BM1 has a full width half maximum (FWHM) of  $6.60 \pm 0.18\mu\text{m}$  and a corresponding Rayleigh length of  $305\mu\text{m}$ , BM2 has a FWHM of  $4.38 \pm 0.16\mu\text{m}$  with a Rayleigh length of  $110\mu\text{m}$ , and BM3 has a FWHM of  $3.85 \pm 0.15\mu\text{m}$  with a Rayleigh length of  $40\mu\text{m}$ .

Fig. 2.3 (c)–(e) demonstrate the different frequency patterns created in the Alexa 561 dye phantom. Fig. 2.3 (f)–(h) show the Fourier transforms of Fig. 2.3 (c)–(e). Fig. 2.3 (i)–(k) show the theoretical modulation depth and the experimental results with the fluorescent dye phantom. Here, we used the 48-pixel pattern ( $9.36\mu\text{m}$ ), which provides the best modulation depth with the  $6.60\mu\text{m}$  beam waist, which is critical for later reconstruction. Fig. 2.4 compares the optical sectioning performance of the widefield DSLM system to RMS-SI, LR-SI, and LR-SI-non, using images of the 200nm YG fluorescent bead phantom acquired by our system. Fig. 2.4(a)–(c) are  $99.84 \times 99.84\mu\text{m}^2$  regions from the  $399.36 \times 399.36\mu\text{m}^2$  image. The PSF is measured using the intensity profile of the fluorescent beads. The lateral PSF is plotted in Fig. 2.4 (i), and Fig. 2.4 (j) is the axial point spread function. The DSLM results in a full width half maximum (FWHM) of  $693 \pm 25$  nm in the y-axis and  $4.64 \pm 0.59\mu\text{m}$  in the z-axis, while the FWHM of the PSF with RMS-SI is  $679 \pm 22$  nm and  $4.43 \pm 0.48\mu\text{m}$ . That of the LR-SI image is  $534 \pm 23$  nm and  $3.91 \pm 0.56\mu\text{m}$ , and that of the LR-SI-non is  $499 \pm 20$  nm and  $3.70 \pm 0.60\mu\text{m}$ . The resolution with LR-SI is better due to the Wiener filter in Eqs. 2.4 and Eqs. 2.5 which boosts the higher frequencies. We calculated the signal to noise ratio (SNR) of each method; the LR-SI-non image shown in Fig. 2.4(d) has an SNR of 386, whereas the images in Figs. 2.4(a), 2.4(b), and 2.4(c) have SNRs of 68, 113, and 124, respectively. LR-SI-non yields a SNR 5.6 times higher than the wide field image and 3.4 times higher than the widely adopted RMS-SI method.

Then, we tested our system with thick biological samples, zebrafish larvae, using a  $11.7\mu\text{m}$  illumination pattern with the  $2\times$  magnification lens pair (beam waist  $4.38 \pm 0.16\mu\text{m}$ ). Fig. 2.5 illustrates the gadrb: RFP expression in a 7-day old zebrafish larva's central nervous system, acquired in the DSLM-SI mode. In

Fig. 2.5(a)-2.5(d), from left to right, are the WF, RMS-SI, LR-SI and LR-SI-non images. Enlarged cutouts from Fig. 2.5(a-d) are shown in Fig. 2.5(e-h) and the contrast enhancement is demonstrated through the line intensity profile at the location noted in Fig. 2.5(e) for each of the methods. The line intensity profile is shown in Fig. 2.5. The Wiener parameter is set to 0.31 for linear reconstruction, resulting in a smoother profile for LR-SI compared to WF and RMS-SI. The LR-SI-non has better contrast in comparison with LR-SI, due to the removal of the zero order term during the reconstruction process which eliminates the scattering component. Fig. 2.6 shows three different time points during a two-minute video clip, comparing the four different methods. From top to bottom, the series of images shows the WF, RMS-SI, LR-SI and LR-SI-non methods, respectively. From left to right, the interval between each time point is 0.5 second. Here, the system has a raw imaging speed of 47.7 fps. The optically sectioned image require 3 images to reconstruct one sectioned image, this will give us a frame rate of 15.9 fps. Our system acquires two color images sequentially, which result in an effective imaging rate of 7 fps. Fig. 2.6 shows that neural activity can be captured by our system in two colors.

The intensity change is plotted as a function of time in Figure 2.6. LR-SI-non has a signal to background ratio of 2.8 and LR-SI has a signal to background ratio of 2.4, which shows that LR-SI-non has higher peak signals relative to the background. However, the LR-SI-non also results in lower signal to noise ratios compared to LR-SI (91 compared to 350). In Fig. 2.6, neural events can be observed at  $t \cong 0s$ ,  $t \cong 75s$  and  $t \cong 97s$ . The optic tectum of the larval zebrafish is a major part of the mid-brain and consists of a large number of unmyelinated axons. This results in a relatively uniform fluorescent region in the image. This region is largely contained within the lower frequency bandwidth. Removal of the zero order term during the reconstruction process results in a lower intensity of the signal, which leads to lower SNR in the ROI.

When imaging large samples, absorption and scattering structures inside the sample in the excitation light path cause stripe artifacts. [120]. Fig. 2.7 shows 2D slices from a 3D stack at a range of depths as a comparison between different methods. Here, we observed that stripe artifacts become much more noticeable as we image deeper into the sample. This is due to the extra tissue, which introduces more scattered light. In addition, the stripe artifacts are much more obvious in RMS-SI and LR-SI-non, because the stripe artifacts are part of the high frequency structure of the image [89]. Fig. 2.7 shows the x-z planes of the 3D volume, illustrating the comparison between all four methods that we described above. LR-SI-non, Fig. 2.7, yields a stronger optically sectioned image. However, the stripe artifact is more apparent in comparison with Fig.

2.7(c). This is noted with a blue arrow in Fig. 2.7(c)-(d). Various computational methods [120, 93] have been developed to mitigate the stripe artifacts, however, the large amount of data in LSM images exponentially increases the computational cost of these methods [63]. Multidirectional SPIM [89] is a promising method for alleviating stripe artifacts, however, it is not compatible with SI. Self-reconstructing beams have been shown to mitigate stripe artifacts and are compatible with DSLM-SI and, therefore, could be used in combination with DSLM-SI and LR-SI reconstruction [43]. The effect of optical aberrations on SI has been studied previously, and the aberrations have been shown to decrease pattern contrast and decrease the SNR of the reconstructed image [184]. By using FEP tubing to mount our samples, we have minimized the effect of spherical aberration in our system, as can be seen by the measured axial width of the PSF, which is in good agreement with the theoretically expected PSF width from a well-corrected 0.5NA objective ( $2\lambda/NA^2 \approx 4.0\mu m$ ). Aberrations could be further controlled through the use of AO.

## 2.7 Conclusion

In conclusion, we have demonstrated the combination of linear SI with LSM to image neural activity in the central nervous system of 7 dpf zebrafish larvae. Using linear SI, we can image 2-D planes in two colors at 7 fps. Linear SI shows higher SNR than both conventional DSLM and RMS-SI. In highly scattering sections, the scattering signal can be eliminated by removing the zero-order term in the linear SI reconstruction. Linear SI with the zero order removal also shows superior axial sectioning compared to RMS-SI in our setup, where the axial resolution of the imaging objective is comparable to the thickness of the light sheet. As the imaging plane is moved deeper into the sample where the sample is thicker, stripe artifacts become apparent due to absorption and scattering of the excitation beam. To address this problem, multiple computational approaches [120, 93] could be applied. In the following chapter, I will discuss the approaches that we developed to reduce the stripe artifacts that are compatible with DSLM-SI.

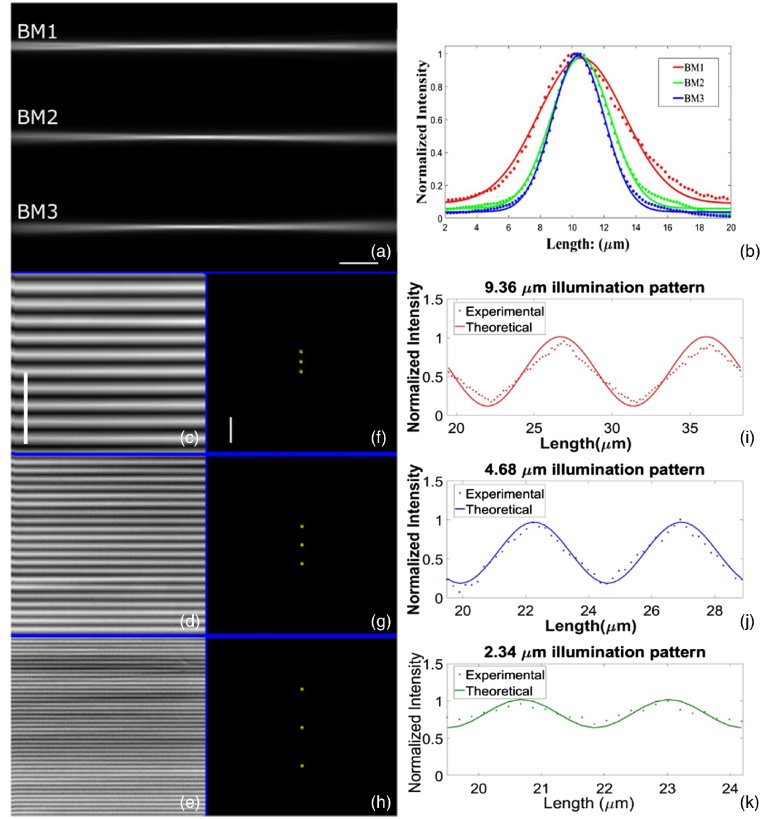


Figure 2.3: Illumination beam profile characterization using Alexa 488 dye phantom. (a). Beams BM1, BM2, BM3 are formed by using  $2\times$ ,  $3\times$ ,  $5\times$  magnification lens pair respectively. The scale bar is  $50\ \mu\text{m}$ . (b). Intensity profile at the beam waist. (c)–(e) SI patterns generated using the  $2\times$  lens pair. SI patterns of  $9.36$ ,  $4.68$ , and  $2.34\ \mu\text{m}$ . The FoV is  $99.84 \times 99.84\ \mu\text{m}^2$ , cutout from the  $399.36 \times 399.36\ \mu\text{m}^2$  image. Scale bar is  $40\ \mu\text{m}$ . (f)–(h) Frequency space representations of (c)–(e), respectively. Scale bar is  $0.3\ \mu\text{m}^{-1}$ . (i)–(k) Normalized intensity plots of the cross-section of the images in (c) and (e). Dotted line is the experimental result and the solid line is the theoretical value.

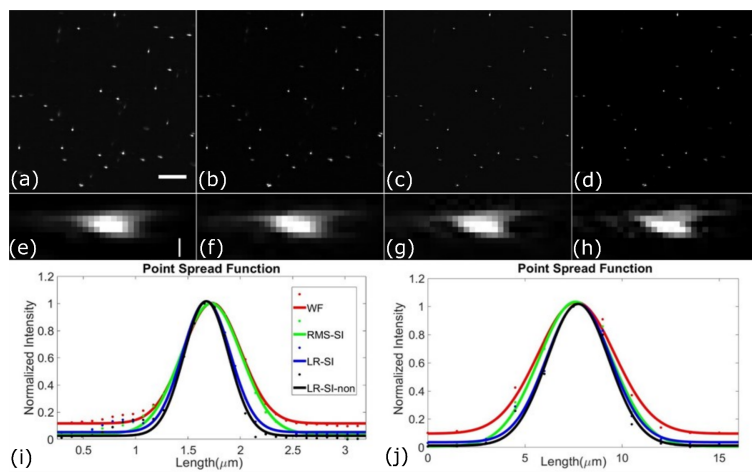


Figure 2.4: Comparing performance with different methods: (a) WF, (b) RMS-SI, (c) LR-SI, and (d) LR-SI-non. Image size  $99.84 \times 99.84 \mu\text{m}^2$  and scale bar  $20 \mu\text{m}$ . (e) - (h) Axial point-spread function measured with beads phantom using the methods mentioned above. Image size  $3.22 \times 18 \mu\text{m}^2$  and scale bar  $5 \mu\text{m}$  (i) Intensity profile of lateral point-spread function along the y-axis. (j) Intensity profile of axial point-spread function of the system

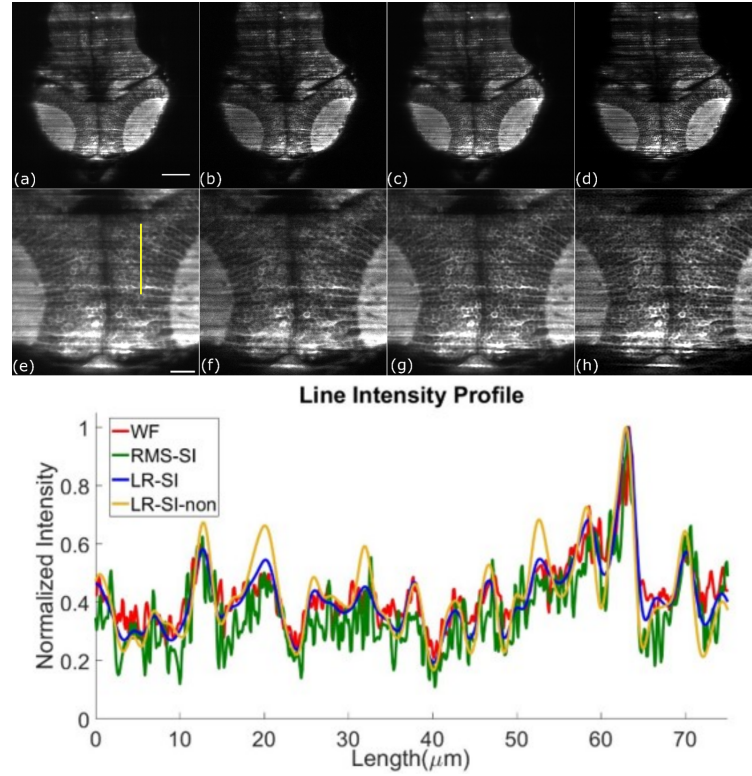


Figure 2.5: Maximum intensity projections of 7-day old *elavl3:GCaMP5g; gad1b:RFP; mitfa<sup>w2/w2</sup>* zebrafish larva. (a)–(d) are WF, RMS-SI, LR-SI and LR-SI-non reconstructed images of the red channel of zebrafish larva’s central nervous system, respectively. WF and RMS images are scaled up  $2\times$  bicubicly to match the pixel count of the LR-SI method. The image size is  $500 \times 500\mu m^2$  and scale bar shown in (a) is  $75\mu m$ . (e)–(h) are  $183.4 \times 183.4\mu m^2$  cutout from (a)–(d) and the scale bar shown in (e) is  $25\mu m$ . Normalized intensity profiles are plotted along line at the location noted in the Figure 6(e) for each of the reconstruction methods. The Wiener parameter ( $w$ ) is set to 0.31 for the linear reconstruction.

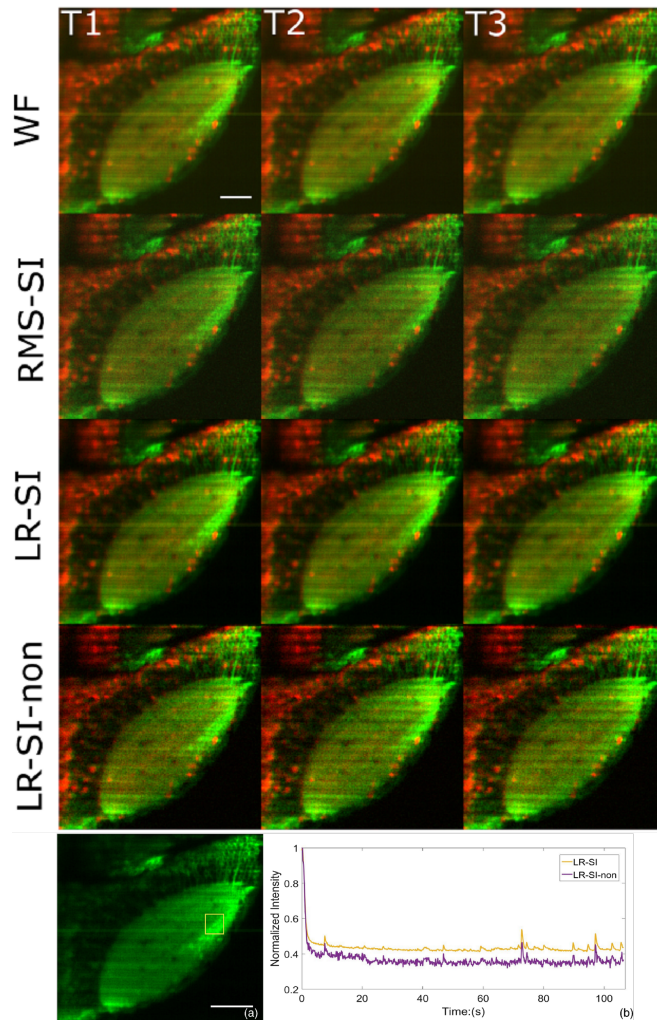


Figure 2.6: 7-day old *elavl3:GCaMP5g; gad1b:RFP; mitfa<sup>w2/w2</sup>* zebrafish larva treated with 15-mM PTZ at three different time points.  $195\mu\text{m} \times 195\mu\text{m}$  cutouts from  $199.7 \times 399.4\mu\text{m}^2$  images are shown. The scale bar is  $30\mu\text{m}$ , and the images are acquired with an illumination pattern of  $9.36\mu\text{m}$  at a speed of  $\sim 48\text{raw fps}$ , corresponding to seven reconstructed two-color fps. The interval between each time point is 0.5 s. The bottom row shows an intensity change of the ROI noted in (a), plotted as a function of time. LR-SI non shows higher peak signals relative to the background compared to LR-SI. However, the LR-SI-non results in lower signal to noise ratios relative to the LR-SI method.

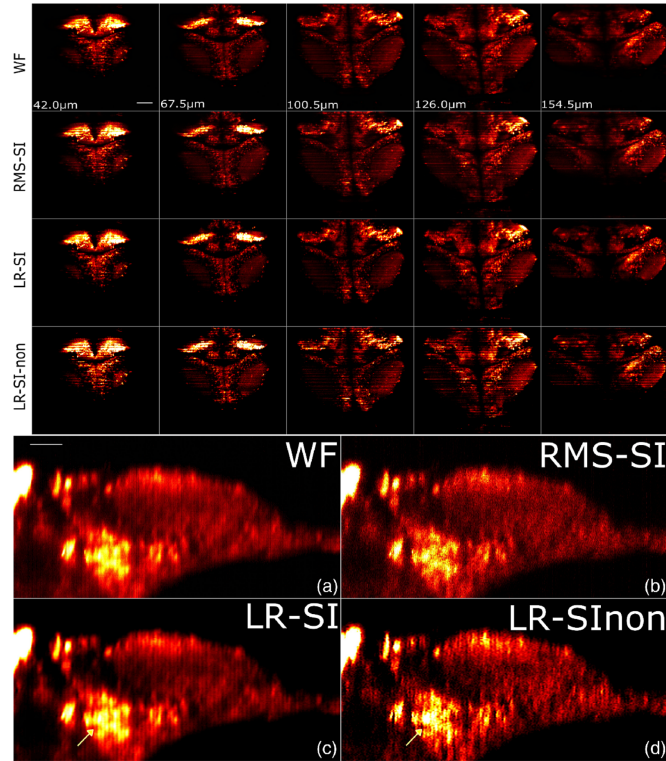


Figure 2.7: Slices from a 3D-image stack of 7-day old zebrafish larva DSLM-SI. From the top to bottom row: WF, RMS-SI, LR-SI, and LR-SI-non. Each column is a different depth into the sample. Comparison of optical sectioning performance. x-z planes from 3-D stack shown.

# CHAPTER 3

## CORRECTING ARTIFACTS IN LIGHT SHEET MICROSCOPY IMAGING

When imaging large, semi-opaque biological specimens with LSM, the structures inside the sample will often cause variations in absorption and scattering as the light sheet travels through the specimen. This leads to optical aberrations and non-uniformity in illumination [89, 200, 63]. This issue has been addressed by using approaches such as multi direction illumination [89, 180, 157], or self-reconstructing light beams such as the Bessel beam [44, 47, 61], or the Airy beam [193, 190]. Unlike the Gaussian beam which is formed by the superposition of plane waves with different inclinations and the angular distribution, these beams are result of the linear superposition of plane waves arranged on the surface of a cone [137]. Therefore the beam will retain its profile even when it is partially obstructed at one point.

Unfortunately, none of these methods are compatible with DSLM-SI. Shadowing artifacts can also be reduced through various computational methods [93, 204]. However, LSM often generates a large number of data sets [5], which results in high computational costs [63]. Recently, a method compatible with DSLM-SI has been proposed that uses a cylindrical lens with DSLM to increase the angular diversity of the illumination beam along the z-axis [63]. This approach, multi-directional digital scanned light-sheet microscopy, has been demonstrated with confocal line detection to reject scattered light.

In this chapter, I will discuss an approach for alleviating stripe artifacts that is compatible with DSLM and DSLM-SI, and we demonstrate a new SI reconstruction approach that further reduces stripe artifacts in the reconstructed image. We demonstrate that the combination of these approaches reduces stripe

artifacts by 20% in line profile standard deviation compared to DSLM-SI alone when imaging the central nervous system of 3 – 4 dpf zebrafish larvae.

### 3.1 Stripe artifact reduction for DSLM-SI

This approach works by quickly dithering the scanning Gaussian beam over a small angle in the axial direction of the detection objective as shown in Fig. 3.1.

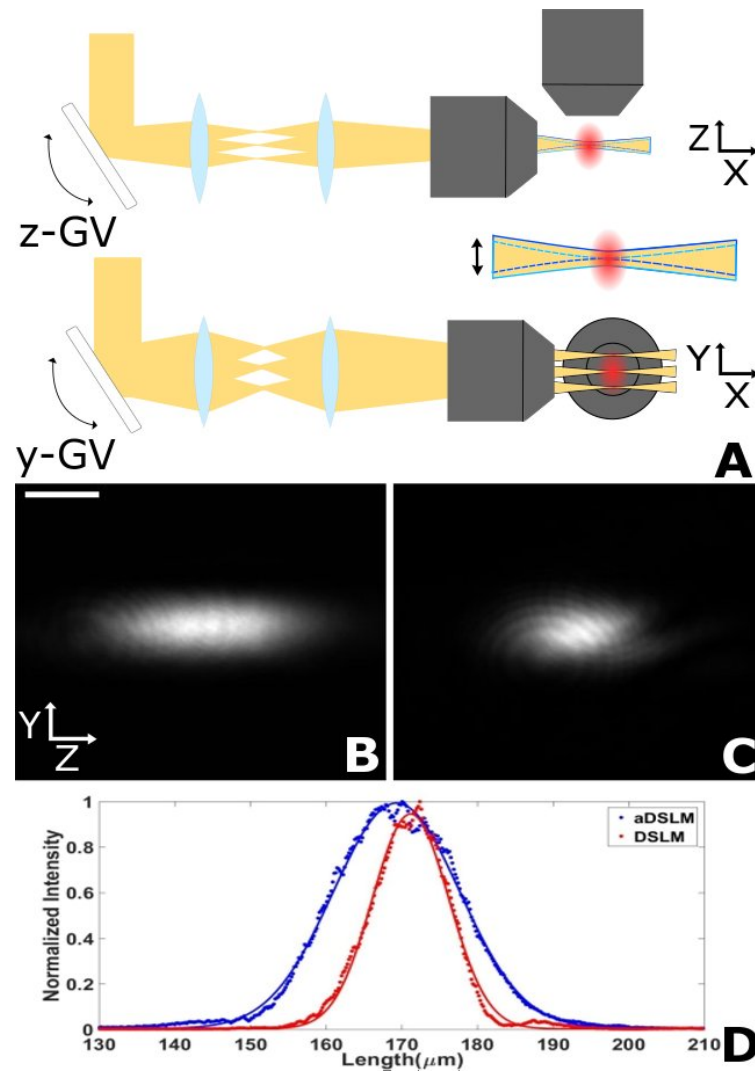


Figure 3.1: (A) Mechanism of axial dithering DSLM. (B) aDSLIM Beam. (C) DSLM Beam. (D) Comparison of beam profiles in the axial direction. FWHM are  $11.83\mu\text{m}$  and  $7.14\mu\text{m}$  respectively. Scale bar is  $10\mu\text{m}$  in (B).

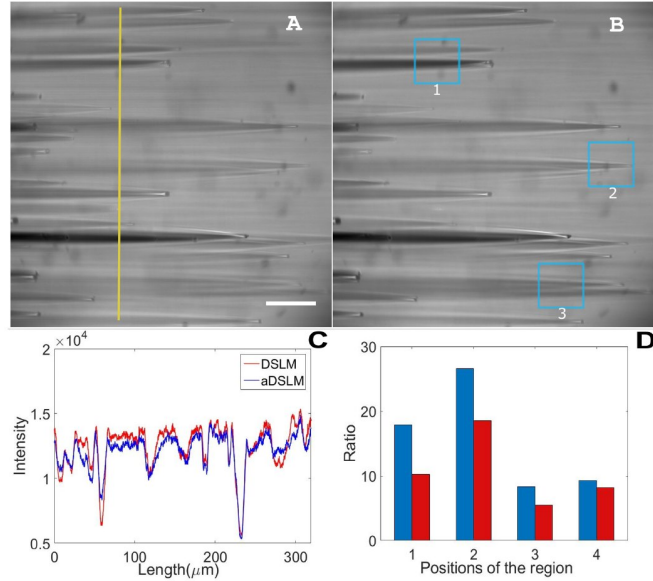


Figure 3.2: Comparison of aDSLm and DSLm using a dye phantom. (A) aDSLm. (B) DSLm. (C) Line profiles along the line indicated in (A). (D) The ratio ( $\alpha$ ) of mean intensity to standard deviation at locations 1,2,3 in (B). 4 is the  $\alpha$  of the entire image. (blue: aDSLm, red:DSLm). Scale bar is  $50\mu\text{m}$ .

As in [63], the axial width of the beam is increased slightly, but the use of a galvo system to axially scan the beam allows for optimization of the dithering angle for each sample. Here, we use less than 0.03 degrees of dithering to minimize the effective thickness of the illumination sheet so that optimum sectioning can be achieved. To achieve uniform illumination, the axial dithering frequency must be large compared to the line scan rate of the camera. We use a dithering frequency of more than 1 KHz in combination with an exposure time of 3.12 ms per line of pixels, this means that the light beam is dithered 3 times axially for each line of the pixels during the exposure period. Fig. 3.1 (b) and (c) show the Gaussian beam profile with and without axial dithering. Line profiles are shown in Fig. 3.1(d). The beam width in the axial direction is increased by a factor of 1.66.

We first compared aDSLm to DSLm without Structured Illumination using a sample created by embedding micro glass spheres (9-10  $\mu\text{m}$ , Sigma-Aldrich 440345) in a fluorescent dye phantom (1.3mM ThermoFisher scientific Alexa Fluor 568 in 2% agarose), Fig. 3.2. As shown in the figure, the glass spheres create large unilluminated stripes in the fluorescent sample. Line profiles are shown in Fig. 3.2(c). Comparing aDSLm to DSLm, Fig. 3.2 (a) and (b), it can be seen

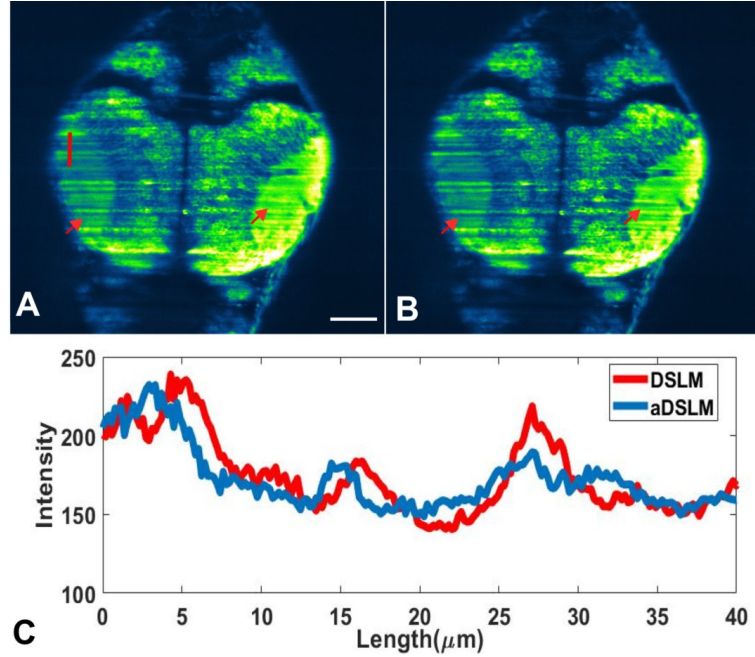


Figure 3.3: Imaging of zebrafish larva. (A) aDSLIM. (B) DSLM. (C) Line intensity profile (averaged over 10 pixels) at location noted in (A). Arrows point to regions where striping is strong in (B). Scale bar is  $50\mu\text{m}$ , Sample is illuminated from right side.

that aDSLIM increases the ratio ( $\alpha$ ) of mean intensity to standard deviation by a factor of 1.46 on average, Fig. 3.2(d). Next, we imaged zebrafish larvae  $156\mu\text{m}$  deep in the  $z$ -direction. All samples are *elavl3:GCaMP5g;gad1b:DsRed;mitfa<sup>w2/w2</sup>* 3 to 4 day post fertilization zebrafish larvae [124]. Here, we image the larval mid-brain with the green fluorescent protein, GCaMP5g, which indicates calcium activity in neurons. Both methods were tested on three different samples. We show that axially dithering the scanning beam can successfully suppress the striping artifacts seen in light sheet imaging of the zebrafish central nervous system, Fig. 3.3. Fig 3.3 (A-B) are taken with aDSLIM and DSLM respectively. The two methods were compared by measuring the difference between the standard deviation(SD)s of the resulting line profiles for each sample. Compared to DSLM, the SDs of the line profiles for aDSLIM are reduced by 18.86%, 20.40% and 20.94%, resulting in an average of 20%.

To create structured illumination excitation, we used the DSLM-SI method which was described in the previous chapter. Here, the wavelength of the illumination pattern is  $4.68\mu\text{m}$ . By employing axial dithering, We show that the

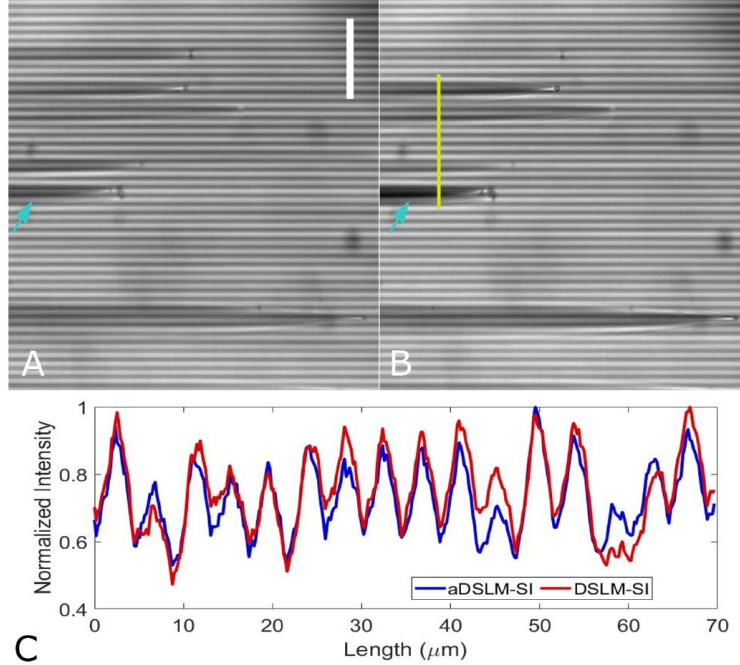


Figure 3.4: Comparison of aDSLMI-SI (A) and DSLMI-SI (B) using a dye phantom. The illumination pattern wavelength is  $4.68\mu\text{m}$ . (C) The line intensity profile plotted at location noted in (B). The blue arrow points to a region where the stripe pattern is notably absent in the DSLMI-SI image. Scale bar is  $40\mu\text{m}$ .

effect of this approach can reduce stripe artifacts in the final image, as shown in Fig. 3.4. The axially dithered DSLM (aDSLMI) SI pattern, Fig. 3.6 (a), is more uniform in amplitude and phase as compared to the DSLMI SI pattern, Fig. 3.6 (b). In structured illumination microscopy (SIM), inconsistent illumination will result in residual fluctuations in the reconstructed image [162].

We then imaged 200 nm fluorescent beads (ThermoFisher Scientifics F8811) embedded in 2% agarose, showing that with aDSLMI we can achieve a resolution comparable to that of DSLMI. Here, we took the SI data and then created the widefield stack and the SI stack. The reconstruction equations can be found in Chapter 2. In Fig. 3.5, aDSLMI has a lateral resolution of  $722 \pm 26\text{nm}$  and axial resolution of  $4.55 \pm 0.43\mu\text{m}$ . DSLMI has resolution of  $688 \pm 25\text{nm}$  laterally and  $4.21 \pm 0.28\mu\text{m}$  axially. We follow the approach of [183] using linear reconstruction to achieve an optically sectioned image, and compared the bead intensity profile for aDSLMI-SI and DSLMI-SI. DSLMI-SI and aDSLMI-SI result in a profile with a full width half maximum (FWHM) of  $534 \pm 23\text{nm}$  and  $581 \pm 24\text{nm}$  laterally,  $4.11 \pm 0.22\mu\text{m}$  and  $4.20 \pm 0.37\mu\text{m}$  axially. By

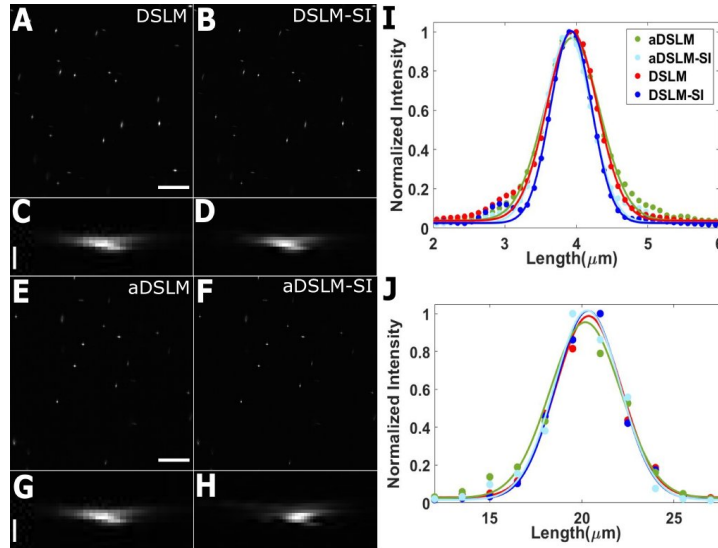


Figure 3.5: Point spread function (PSF) comparison using beads phantom. (A),(B),(E),(F) show the lateral PSF. Pixel size  $97.5 \times 97.5 \text{ nm}^2$ . (C),(D),(G),(H) show the axial PSF. Pixel size of  $0.0975 \times 1.5 \mu\text{m}^2$ . (I) and (J) are the intensity profiles of the lateral PSF and axial PSF, respectively. Scale bars in A and E are  $20 \mu\text{m}$  and scale bars in C and G are  $4 \mu\text{m}$ .

employing axial dithering, the resolution of the system increased by less than 5% laterally and 8% axially. The Wiener parameter is adjusted by inspecting the final image and is set to 0.31 for all the linear SI reconstructions.

### 3.2 Adaptive linear SR-SI reconstruction

When computing the reconstructed image in structured illumination, another source of artifacts is inaccurate estimation of the reconstruction parameters [70]. Traditionally, a uniform patterned illumination across the entire image is assumed. Therefore, the reconstruction parameters are calculated using the entire image. This works in DSLM-SI for small samples and when using the Root Mean Square (RMS) reconstruction method, which does not depend on accurate knowledge of the SI pattern wavelength [141]. But it has been demonstrated that linear SI reconstruction works better than the RMS method [183], and the Gaussian beam in DSLM can be shifted when traveling through large biological samples leading to non-uniform pattern wavelength and phase shifting in different sub regions of the 3 SI images. Here, we use an adaptive linear reconstruction approach to address this issue.

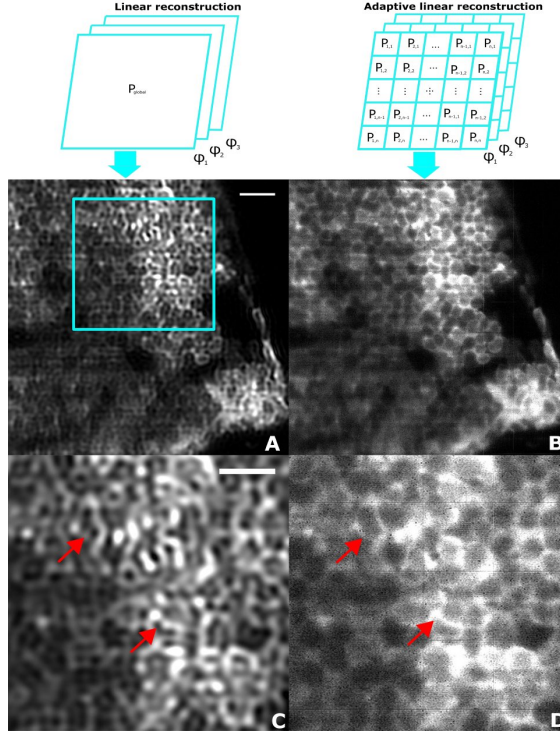


Figure 3.6: Imaging of zebrafish larvae. (A) Uniform LR-SI. (B) Adaptive LR-SI. (C) and (D) are enlargements of (A) and (B) respectively at the location of the box in (A). Arrows indicate regions where the distortion of the uniform LR-SI result is evident. The scale bars in A and C are  $30 \mu\text{m}$  and  $10 \mu\text{m}$  respectively. Sample illumination is from the right side.

This method works by first segmenting the three SI images with different phases into smaller sub-image sets ( $P_{\varphi_i, n, n}$ ), then calculating the angle, SI pattern wavelength, and phase for each set of subimages. In this way, the reconstruction parameters are estimated locally to account for the heterogeneous illumination pattern. Each sub image is computed with the local parameters. Then, all of the sub images are tiled together based on their original positions to form the final image. The size of the subregions should be as small as possible. This will allow us to measure the local reconstruction parameter in the most accurate way. However, the size of the subregion should also be large enough to contain features of the sample. If the subregions are too small, accurate reconstruction parameters cannot be achieved because the frequency space images are not resolved enough. Here, subregions with 64 by 64 pixels are used. The above approach is illustrated in Fig. 3.6. Fig. 3.6 (a–b) shows the optically sectioned image using the linear reconstruction method [183] and

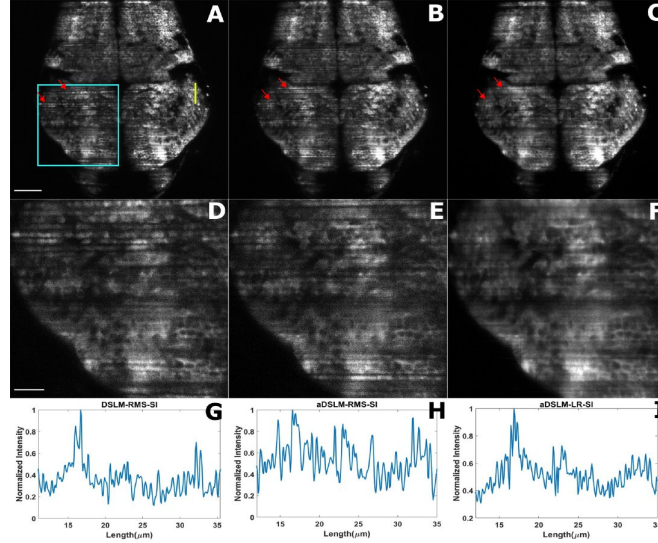


Figure 3.7: (A),(B) and (C) are RMS-DSLMSI, RMS-aDSLMSI, and adaptive-aDSLMSI respectively. (C),(D) and (E) are respective close-ups of the box area shown in (A). Arrows point to areas where the stripe artifact is especially strong on the RMS-DSLMSI image. (G-I) Respective line profiles at the position indicated in (A) by the yellow line. Scale bar in (A) is  $50\mu\text{m}$  and  $20\mu\text{m}$  in (D). Sample is illuminated from right side.

adaptive linear reconstruction. Fig. 3.6 (c–d) is the enlarged region noted in Fig. 3.6 (a–b). When using global reconstruction, the borders between cells are distorted, while in 3.6(d), the edges are well-defined. The figure shows how adaptive linear reconstruction not only reduces stripe artifacts but also reveals greater detail in the image. Here, no blending between each subregion is used, however, a cosine window can be used to blend the edge of the subregion so that the final assembled image will have a smooth transition between each tile.

Finally, we compared adaptive linear aDSLMSI with the widely adopted RMS method [141], both with and without axial dithering. Fig. 3.7 (a–c) are RMS DSLMSI, RMS-aDSLMSI and adaptive-aDSLMSI, correspondingly. Reduction in stripe artifacts can be observed in the positions noted with red arrows. The artifacts decrease with each figure from left to right. Fig 3.7 (d–f) are box cut outs from Fig. 3.6 (a–c) at the location noted in Fig 3.7 (a). The line intensity profile is plotted for each method for the line location in Fig. 3.7 (a). In Fig. 3.8, we calculated the ratio ( $\alpha$ ) of mean intensity to standard deviation at the different locations noted in Fig. 3.8 (a) and plotted in Fig. 3.8 (b). aDSLMSI-LR-SI has an average 38.1% increase in  $\alpha$  compared to DSLMSI-RMS-SI due

to the reduction in stripe artifacts. Fig. 3.8 (c–e) are the power spectra of the respective methods. The peaks in the power spectrum due to striping are circled. Compared to RMS DSLM-SI, the magnitude of these peaks is reduced by a factor of 1.5 using RMS-aDSLMSI and a factor of 4 using adaptive-aDSLMSI.

In conclusion, we have demonstrated a new approach to reducing the stripe artifacts in DSLM by dithering of the illumination beam axially. This approach can be easily implemented without any additional optics. This method can be combined with structured illumination without reducing the pattern frequency and achieves a more sinusoidal intensity distribution. In addition we demonstrated that adaptive linear structured illumination can successfully reduce the stripe artifacts and improve image quality. Here, the imaging speed is rather slow, primarily due to the slow dithering speed of the galvo mirror. Because the line exposure time should be long enough for multiple dithering cycles, this can be addressed with a fast resonant scanner to further improve the dithering rate.

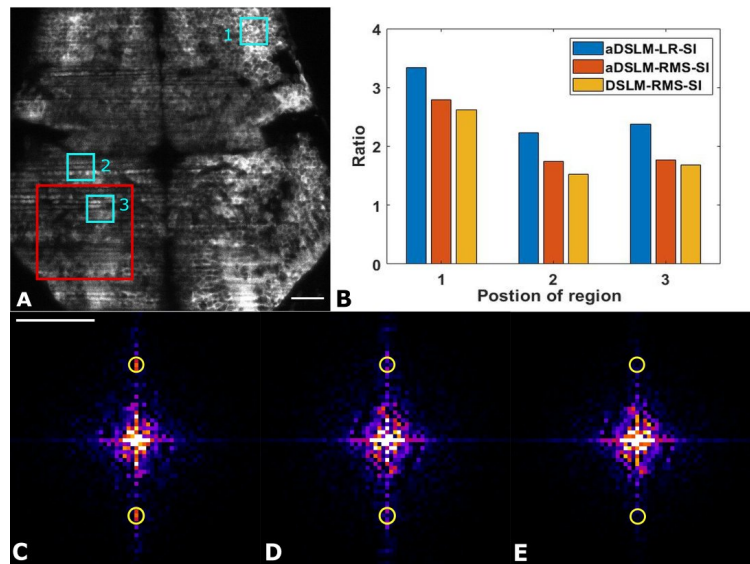


Figure 3.8: Performance comparison using 3-dpf zebrafish larva. (A) RMS-SI image and the region of interest locations. (B) Ratio of mean intensity to SD for the different methods at the regions indicated by blue boxes in (A). (C)-(E) Power Spectra of the region indicated by the red box in (A). Scale bar is  $30\mu\text{m}$  in (A), and  $0.2\mu\text{m}^{-1}$  in (C). Sample illumination is from the right side.

# CHAPTER 4

## VOLUMETRIC LIGHT SHEET MICROSCOPY WITH AN ELECTRICALLY TUNABLE LENS AND ADAPTIVE OPTICS

In optical microscopy, aberrations significantly decrease the performance of the imaging system. Therefore, these systems often fail to reach the diffraction-limited resolution. Sources of optical aberrations can be categorized into two major categories, system aberrations and sample-induced aberrations. System aberrations mainly occur due to imperfections in the optical elements and their misalignment, and sample-induced aberrations are due to the biological specimens' geometrical shapes and the heterogeneous nature of the refractive index inside the specimen.

In current biological research, thick ( $> 50\mu m$ ), larval-stage organisms are often used as models. Unfortunately, with LSM the image quality suffers from optical aberrations even though only a section of the tissue is illuminated at the focal plane of the imaging objective lens. This issue affects the LSM in the illumination path as well as in the optical detection path. The resolution and contrast of LSM images worsen as the imaging plane moves deeper into the sample. In this chapter, I will discuss the implementation of AO correction on the emission side of the LSM, as well as AO correction with ETL for volumetric imaging.

## 4.1 Light Sheet Microscopy with Adaptive Optics

Adaptive optics (AO) can be used to correct the optical wavefront distortion in fluorescence microscopy [95, 12]. AO uses a dynamic element, such as a deformable mirror (DM) or a liquid-crystal spatial light modulator (SLM) to modify the optical wavefront, undoing the distortion caused by the sample or by imperfections in the optical elements and their alignment [13]. This has been shown with many different microscopy techniques, such as confocal microscopy [77], wide field microscopy [99], STORM microscopy, [182, 181], structured illumination microscopy [184, 182], multiphoton microscopy, and LSFM [198, 123]. AO has had a significant impact on biological optical microscopy. It has allowed for imaging at greater depths into specimens and has improved the resolution and contrast of the final resulting images. The combination of AO with LSFM will certainly address the existing challenges with LSFM. In the following section, I will discuss the implementation of sensorless AO with LSFM.

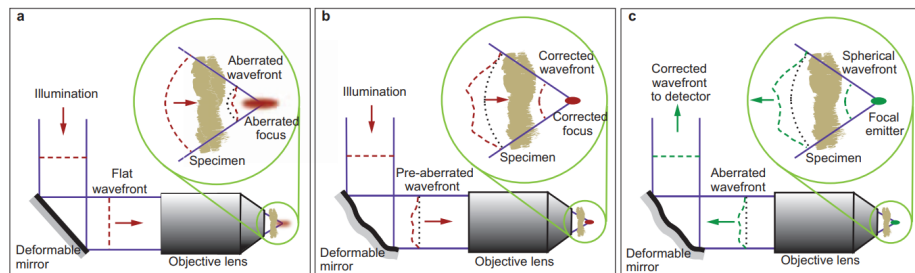


Figure 4.1: (a) illustration of aberration affecting the focus of the illumination light. (b) shows AO correction of the excitation light. (c) shows AO corrections on the imaging path. This figure is reprinted from [13].

Wavefront-sensorless AO is a popular method of aberration correction in microscopy. Instead of measuring the wavefront directly, sensorless AO systems infer the aberrations from a sequence of image measurements taken with changes applied to the adaptive element. The best image quality is achieved by optimizing the correction settings iteratively. The predominant effect on the illumination side of the LSFM would be deflection of the light sheet away from its nominal plane. This means that the layer illuminated by the light sheet no longer lies in the focal plane of the imaging objective lens [13]. This will primarily cause light scattering and first-order defocusing. The defocusing can be corrected simply by refocus the imaging plane to the light sheet [161] or by using a galvo mirror to control the tilt of the illumination sheet, compensating

for the deviation of the light sheet [159]. However, more complex optical aberrations in the imaging path still remain to be solved in the application of LSFM to imaging of thick specimens.

LSFM uses a wide-field detection scheme. Normally, an extended scene is captured on the camera, making the implementation of sensorless AO to LSFM much easier than a sensor-based approach, where there are complexities involved with a guide star [97] and implementation is costly [123]. The sensorless AO uses a sharpness metric evaluate quality of the signal captured by the detection sensor. In general, a set of 3 – 5 measurements which are acquired with different amplitudes of each Zernike mode on the deformable mirror. Then the measured values are fitted to a quadratic function to determine the optimum correction value [181]. The application of AO correction to the detection side of the LSFM was first shown by Bourgenot et al [20]. Bourgenot’s work shows the AO correction mostly on the aberration caused by the mounting glass capillary. This work showed that with sensorless AO, it is possible to improve image quality over 3D imaging volume.

## 4.2 3D Imaging of Light Sheet Microscopy

With LSFM, a 3D imaging volume of the sample can be acquired using a series of 2D images along the optical axis of the imaging objective lens. This is commonly achieved by moving the sample across the illumination plane. This approach is rather slow and introduces additional mechanical stress to the delicate biological sample. A faster approach is using a galvo scanner to scan the light sheet through the sample. However, this requires the focal plane of the imaging objective must also be scanned to coincide with the illuminated plane. Here, the detection objective lens is mounted on a piezo stage to capture an in-focus image while the light sheet is scanning. [143, 152, 188, 118]. The stage scanning will take about 40 seconds (0.0247Hz) for a imaging volume with  $200\mu\text{m}$  axial range since the stage requires a long time to be stable after each step. The piezo stage method will be about 30 times faster (0.8Hz) than the sample moving approach when taking the same imaging volume size [4].

A popular method for accelerating the volumetric imaging speed involves using an electrical tunable lens (ETL) in the detection path of the LSFM [212, 94, 139]. This method has several advantages over other methods. For instance, it eliminates the mechanical movements of the sample or of the detection objective lens. Also, no post-processing step is required, in contrast to the depth of focus extension methods [39]. Fahrback et al first combined these two methods in order to investigate the beating heart of a zebrafish [46], reaching a volumet-

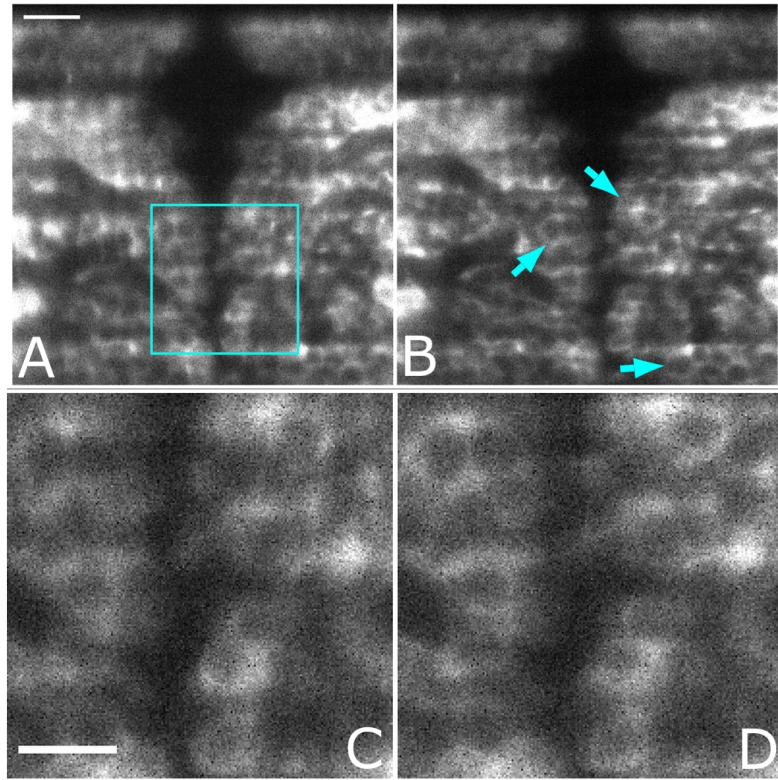


Figure 4.2: 3-day old *elavl3:GCaMP5g; gad1b:RFP; mitfa<sup>w2/w2</sup>* mutant zebrafish larva AO comparison, maximum intensity projection in green channel is showed here. 7 iterations are used to achieve a converged result. (A) Without AO correction. (B) With AO correction. (C) Expanded view of boxed region in (A). (D) Corresponding expanded view of (B). Image size  $99.84 \times 99.84 \mu\text{m}^2$ . Scale bar in A is  $15 \mu\text{m}$

ric imaging speed of 30Hz over a  $100 \mu\text{m}$  range. Although the introduction of an ETL allows for increased imaging speed, it also leads to aberrations [55, 39, 176]. The aberrations vary across the imaging area, and as the ETL is tuned to larger focal power values, the aberration increases radially from the center of the image outwards toward the marginal region of the image. A large coma aberration can be observed in Fig. 4.3. This strains the usable field of view and scan range [46, 39]. Under-sampling the PSF with a lower-NA objective lens is a common way to avoid this effect [46, 56, 161]. The aberrations are increased when a higher-NA objective lens is used. To compensate, a smaller field of view and shorter tunable range of the ETL can be used [102, 197, 121]. To improve

image quality, deep learning-based deconvolution algorithms also have been implemented [31]. However, a shortcoming of the deconvolution approach is that it is incapable of recovering lost phase information or residual artifacts after deconvolution [131].

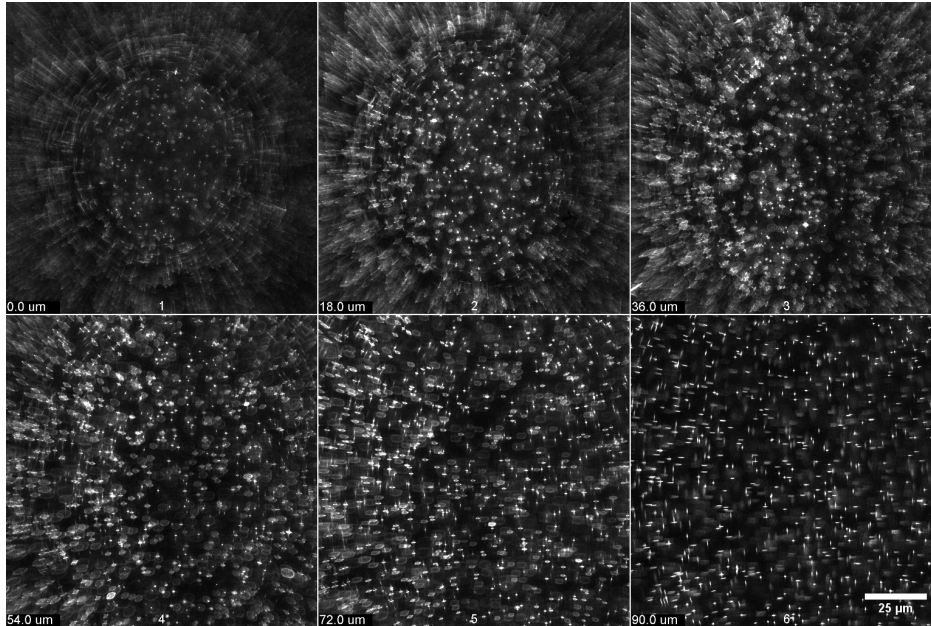


Figure 4.3: Demonstration of aberration caused by electrical tunable lens as function of focal power using fluorescent beads sample.

Here, we show a LSFM system that combines sensorless AO and ETL for volumetric imaging, where the AO reduces the aberration introduced by the ETL along the optical axis as well as reducing off-axis aberrations. This system can improve the signal-to-background ratio by a factor of 3.5 across the entire field of view of the system, as compared to no AO correction. In addition, we show that this system is fast enough to capture neural activities in the central nervous system of 5-7 dpf zebrafish larvae with  $500 \times 500 \mu\text{m}^2$  FOV at a speed of 7s per volume.

### 4.3 Optical Setup

In this work, we modified the optical layout described in the previous chapter to incorporate an ETL. The layout of this LSFM system is shown in Fig. 4.4. In the illumination path, the laser beam is expanded through a set of achromatic doublet lens pairs by a factor of 1.5 (Thorlabs AC254-075-A-ML, Thorlabs AC127-025-A-ML), then a cylindrical lens (Thorlabs ACY254-050-A) is used

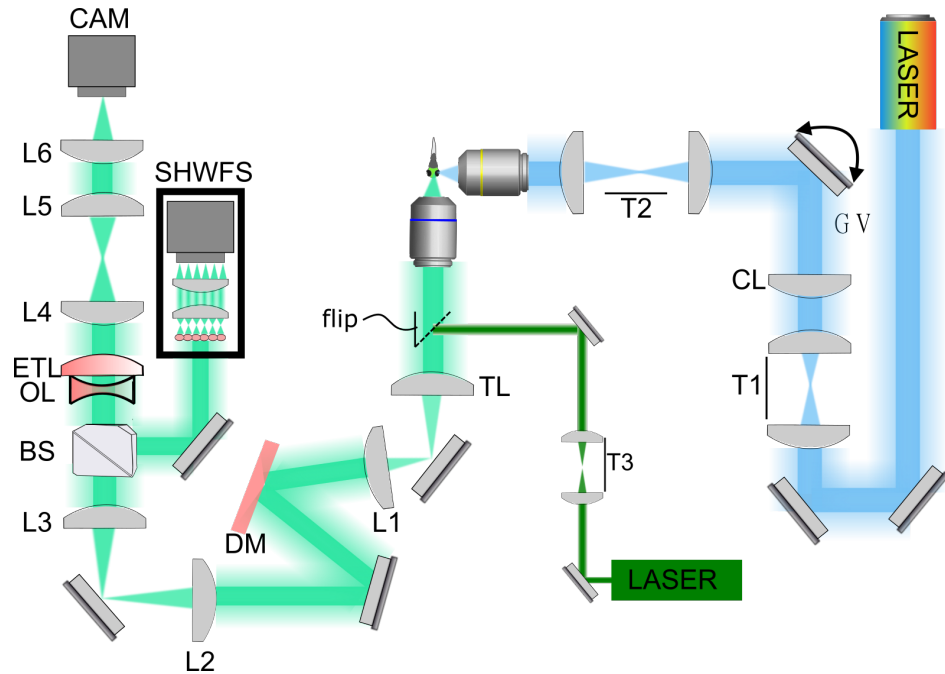


Figure 4.4: Schematic of the optical setup. A  $10 \times 0.3$  NA water dipping objective was used as the illumination objective and a  $40 \times 0.8$  NA water dipping objective was used as the detection objective lens. DM stands for deformable mirror; T1:  $2\times$  magnification lens pair (25mm and 50mm efl); T2:  $5/3$  demagnification lens pair (50mm and 30mm); TL: Tube lens (180mm efl); A green He-Ne laser and T3: magnification lens pair (25mm and 200mm efl) is used to calibrate the home-built Shack-Hartmann Wave front Sensor L1-2: Relay lenses ( $f_1=100$ mm;  $f_2=200$ mm). L3-4: Relay lenses ( $f_4=300$ mm and  $f_3=200$ mm); L5-6 is a magnifying lens pair (300mm and 150mm efl) to give a overall magnification of 26.67 for the final image. CL, cylinder lens (50mm efl). OL is the offset lens ( $-75$ mm efl) and ETL is the electrical tunable lens.

to form a line-shaped beam profile at the back pupil of the illumination objective lens. A two-axes galvo scanner (Thorlabs GVSM002) directs the laser beam into another pair of lenses with a magnification of 0.6 (Thorlabs AC127-030-A-ML, Thorlabs AC127-050-A-ML). Then a 0.3 NA water dipping objective lens (Olympus UMPLFLN 10XW) is used to create a light sheet at the focal plane of the 0.8 NA detection objective lens (Olympus LUMPLFLN 40XW). The image is formed by a tube lens (Olympus U-TLU), then the back pupil of the detection objective lens is imaged onto a deformable mirror (Boston Micromachines Multi-3.5-DM) with a 100mm achromatic doublet lens (Thorlabs AC508-100-A-ML). After the deformable mirror, the pupil of the detec-

tion objective lens is further relayed onto a Shack-Hartmann wavefront sensor (SHWFS) as well as onto a electrical tunable lens (ETL, Optotune EL-10-30-TC) using L2, L3 and a beamsplitter cube (Edmund optics 45 – 417,200 mm; Edmund optics 45 – 418,300mm ; Thorlabs BS013). An offset lens (-75mm eff) is used to adjust that the tuning range of the ETL  $-3.50 \text{ m}^{-1}$  to  $6.67 \text{ m}^{-1}$ . Then L4 (ACT508-200-A-ML) is used to form an image. L5 and L6 (Thorlabs AC508-300-A-ML, AC508-150-A-ML) are used to give the system a overall magnification of 26.67. A sCMOS camera (pco edge 4.2, Cam2 in Fig. 4.4) is used for the SHWFS [117, 125].

## 4.4 ETL and Galvo Mirror Calibration

A sparse beads phantom is used to calibrate the ETL-light sheet microscope. The general procedure for ETL calibration involves driving the ETL as the illuminating light sheet is parked at sequential locations along the axis of detection. The tunable range of the ETL in our system is approximately  $164 \mu\text{m}$ , which can be calculated from Equation (4.1) where the range of  $\frac{1}{F_{ETL,eff}}$  is given above.

$$\delta Z = \frac{-1}{M_{det}^2} \cdot \frac{1}{F_{ETL,eff}} \cdot \left(\frac{L_1}{L_2}\right)^2 \cdot L_3^2 \quad (4.1)$$

We park the light sheet using the galvo scanner at 30 different positions within the imaging range, for each position of the light sheet, 50 camera exposures are captured during scanning of the ETL, and the ETL is driven with a sine wave. Due to hysteresis of the ETL, the optimal settings of the ETL for each light sheet position are slightly different depending on whether the ETL is being driven to higher optical power or to lower optical power. After these image stacks are captured, each of the stacks is evaluated to determine the sharpest image setting for each of the light sheet positions, shown in Figure. 4.5.

## 4.5 Multi-Region AO Corrections

We used a sensorless approach to determine the optimal setting for the deformable mirror [14]. Here, a set of images is acquired using a deformable mirror set to different Zernike modes with a range of amplitudes (3-5 different amplitudes). These images captured by the sCMOS camera are evaluated using different image sharpness metrics, and the values provided by the metrics are fit to a quadratic function to determine the optimum amplitude for each Zernike mode [181]. Three sharpness metrics are used interchangeably, and this

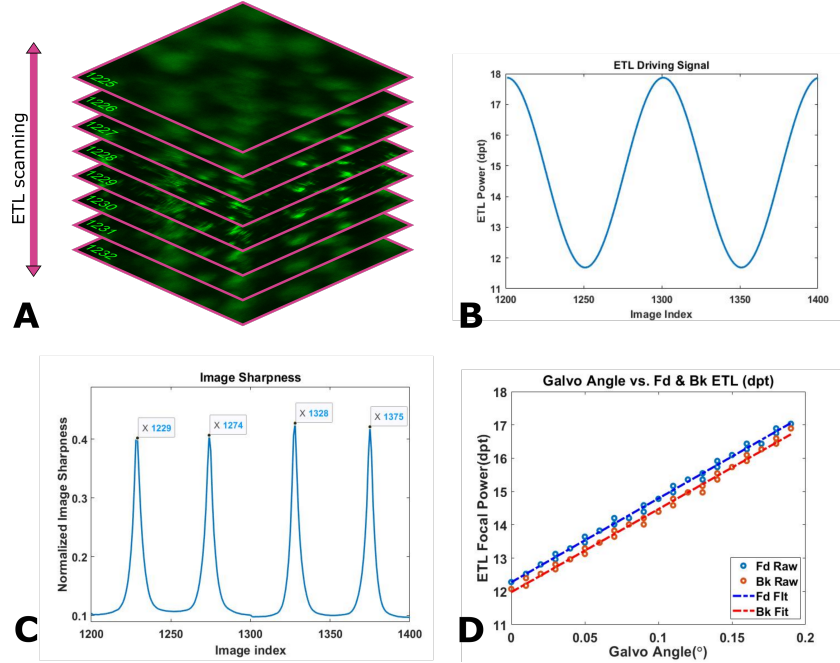


Figure 4.5: (A) Representation of dual direction scanning of the ETL for a parked light sheet position. (B) Sinusoidal driving signal of the ETL. (C) Shows plot of image sharpness vs. frame index. (D) Calibrated ETL focal length as a function of galvo settings.

is evaluated by the user empirically. These sharpness metrics are shown in Fig 4.6(C). We correct from  $Z_4$  to  $Z_{14}$ , a total of 10 Zernike modes [142].

Here, we divide the image into multiple sub-regions, then use the sensorless approach to map out the optimum AO correction settings for each sub-region for the given axial settings of the ETL. The same procedure is then repeated along multiple axial positions. The size of the sub-region for obtaining the AO settings as well as the radial distance of the sub region from the center of the image can be adjusted and evaluated by the user. Typically, a three quadrant division is used, where each region of interest is  $256 \times 256$  pixel<sup>2</sup> and the radial distance of the region of interest is  $97.6\mu\text{m}$  (400 pixels) in length. Further, the aberration caused by the electrical tunable lens is within the correction capability of the DM up to  $Z_{14}$ . Once the AO settings are determined, they will be applied as the volume is being acquired. This procedure is shown in Fig.4.5(B). The final image is generated through image fusion. The image fusion process involves taking multiple separate images, then cutting a section from each image, and then combining the sections together to make one fused image.

## 4.6 Sample Preparation

In this work, we use sub-diffraction fluorescent beads and biological samples to test the performance of our system. We prepare bead phantoms with 200nm yellow-green (ThermoFisher Scientific F8811) fluorescent beads. The beads are first diluted with DI water ( $18.2 \text{ M}\Omega/\text{cm}$ ) in a ratio of 1:100. Then, we mix the stock together with 3% agarose gel in a ratio of 250 to 1. A micro capillary tube is then used to draw the solution and hold the sample after the gel has been gently extruded.

For live zebrafish imaging, we followed the procedure described in [124], where we first paralyse 4-7-day post fertilization PTU treated transgenic zebrafish larvae using alpha-bungarotoxin ( $125.25 \mu\text{M } \alpha\text{-BTX}$ ) or Tricaine. Then we place the fish in a 3% low melting point agarose solution and load it into a glass capillary. For neural activity imaging, we use the procedure described in our previous work [124], treating the sample with PTZ before the imaging session.

## 4.7 Signal-to-Background Ratio Comparison

In this work, we compare the peak signal to background ratio (SBR) between the images acquired with and without AO across the imaging field along the axial range. We first calculated the mean intensity value of four different dark regions measuring  $150 \times 150 \text{ pixels}^2$  around the corner of the images, and used the average value as the background value of the image. Then, the peak signal value of a  $256 \times 256 \text{ pixels}^2$  sliding window is measured across the entire image with a step of 50 pixels. The SBR is then calculated along the center of the image horizontally as well as vertically.

## 4.8 Image Fusion

We divide the image into 4 regions, and 5 axial ranges with different AO settings. Therefore, for each z step, 4 images are captured with different AO corrections. The final raw image stack contains a total of 400 images. For every final fused image, we cut out a section of the images with its corresponded AO corrected region to merge with the other images for each z step, and no blending is used in this process.

## 4.9 Results and Discussion

In this work, we first tested the performance of our system with a fluorescent bead sample, where we acquired an image volume stack using multi region AO corrections and compared it with the volume acquired without AO corrections. The image field is divided into four sections, and the corresponding correction wavefronts are shown in Fig. 4.7(g). Then, we calculated the signal to SBR across center of the FOV both vertically and horizontally for each  $z$  slice of the image stack. We then sum the SBR of the image stack along the  $z$ -axis. We achieved an overall SBR with multi region AO correction for ETL-LSFM that than is 3.40 times higher along the vertical direction and 3.68 times higher along the horizontal direction than w/o AO corrections. This result is shown in Fig. 4.7(h). The enlarged image is plotted in Fig.4.8. A border location is selected, which is marked in Fig. 4.7a, and multiple  $z$  positions are plotted to show that the resolution of the system is improved with mapped AO using a beads sample. Three different  $z$  positions are shown here. Next, we applied this approach to zebrafish larvae over a  $400 \times 400 \times 96 \mu\text{m}^3$  volume. The maximum intensity projection over the  $96 \mu\text{m}$  is shown in Fig. 4.9, where (a) and (b) show before and after AO correction respectively. The improvement of the details can be noted in the locations which are indicated by the arrows. Without AO correction, the cell bodies of the neurons are elongated. This may lead to false interpretation in later analysis. After the correction, a much more spherical shape of the neuron cell body is achieved.

In this system, the DM and ETL are synchronized using software commands, which limits the overall imaging speed to 7 second per volume ( $17.5\text{ms}/\mu\text{m}$ ). This is primarily due to the lack of electrical inputs of the DM. A faster method could be implemented using DM as the master signal generator for other devices in the system or a conjugated AO approach to reduce the number images needed for each  $z$  step. This approach can be further combined with other software based image correction methods, such as spatially varying deconvolution or a deep learning method.

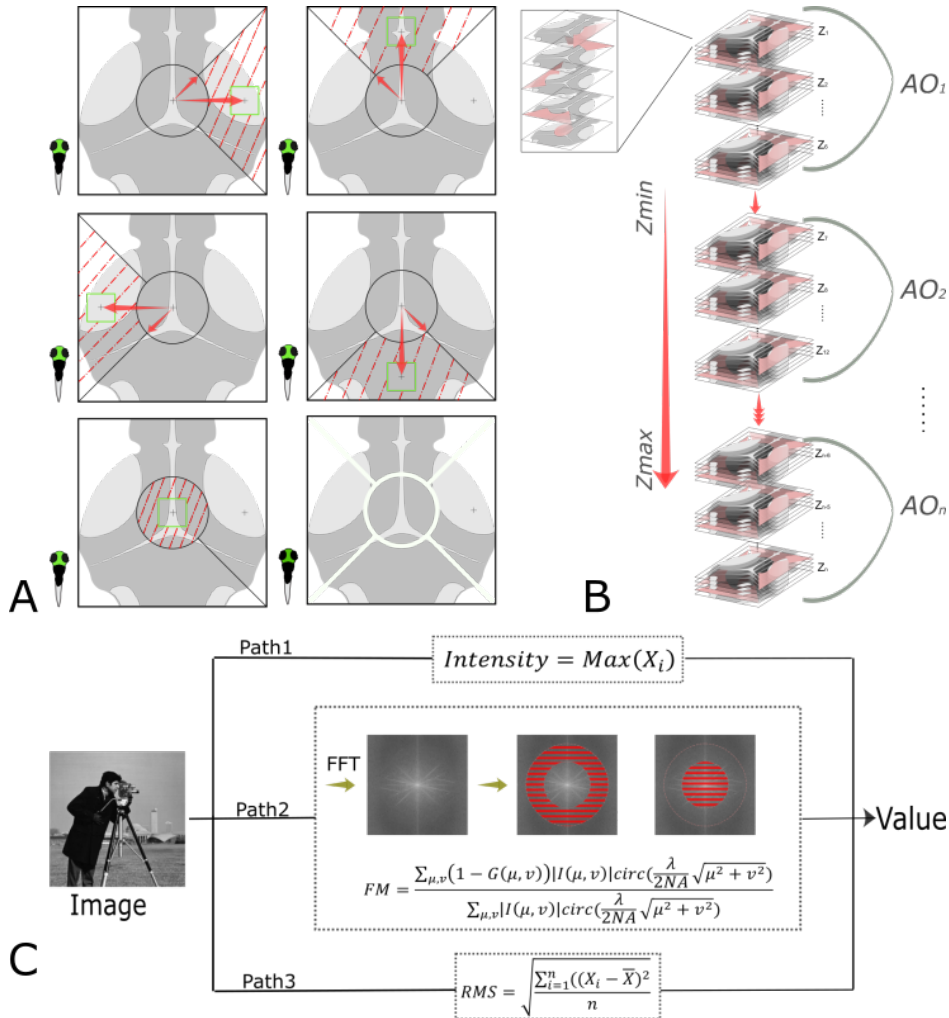


Figure 4.6: Multi-correction AO for ETL-LSFM. (A) Shows the image being divided into different regions, where each region's AO correction setting is obtained using a sensorless approach. (B) Explains that a set of multi-region AO settings is collected along the axial imaging range. (C) Shows the image sharpness metrics used for mapped AO, where the metric is selected based on its performance for different samples and regions.

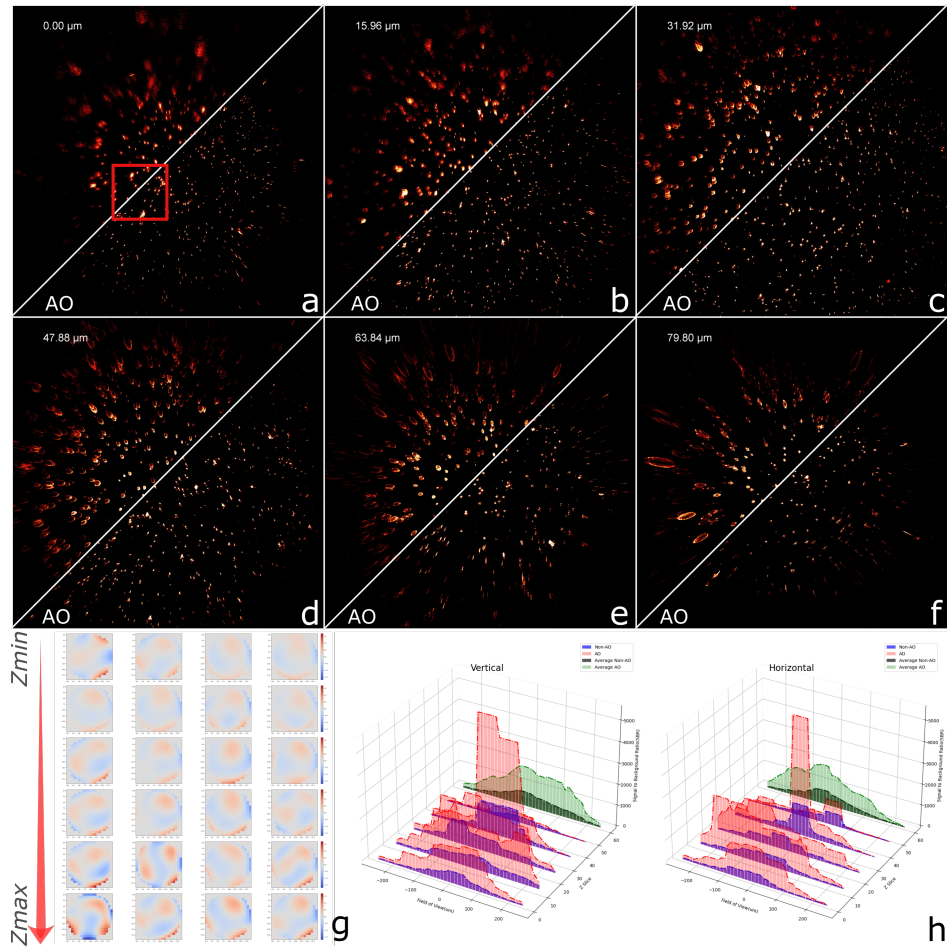


Figure 4.7: Multi-correction AO for ETL-LSFM on beads. (a)-(f) Shows the beads images acquired with and without AO, using three divided regions at different axial positions in a 3D stack (every  $16 \mu\text{m}$ ). (g) Shows the reconstructed wavefront using mapped AO settings for different regions along the axial scan of the ETL. (h). Shows the SBR comparison of an image volume at 6 different axial positions.

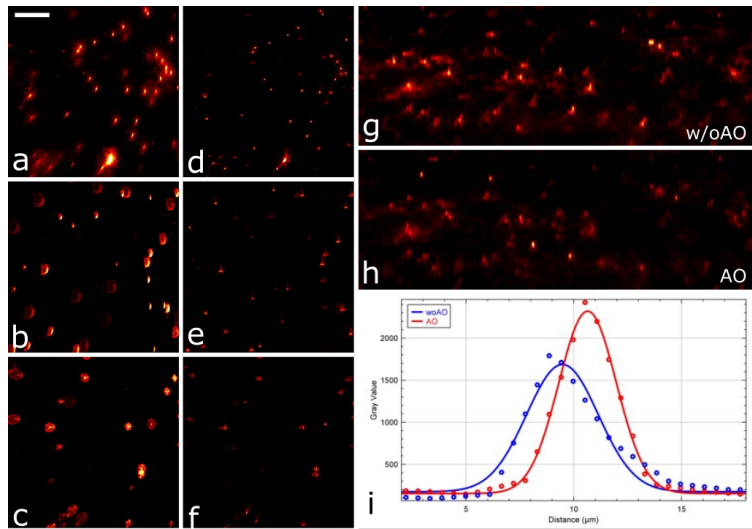


Figure 4.8: *dlx6:GFP nacre<sup>-/-</sup>* mutant zebrafish larva AO comparison, maximum intensity projection over 96 microns is shown here. (a) Without AO correction. (b) With AO correction. The scale bar is (a) is 100  $\mu\text{m}$ .

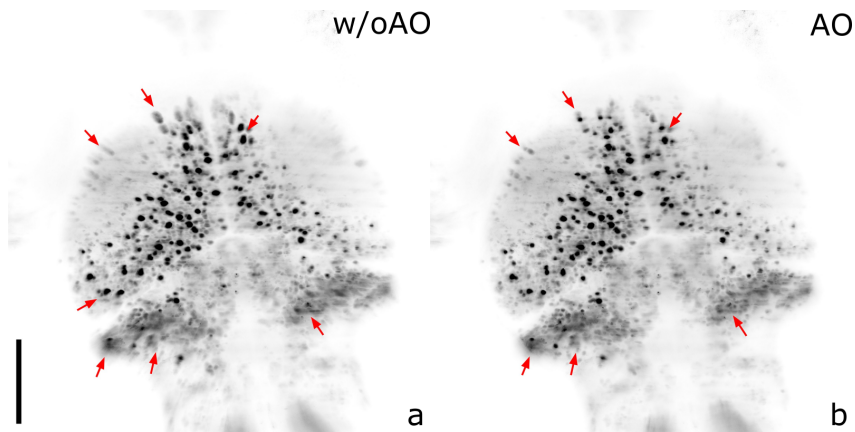


Figure 4.9: *dlx6:GFP nacre<sup>-/-</sup>* mutant zebrafish larva AO comparison, maximum intensity projection over 96 microns is shown here. (a) Without AO correction. (b) With AO correction. The scale bar is (a) is 100  $\mu\text{m}$ .

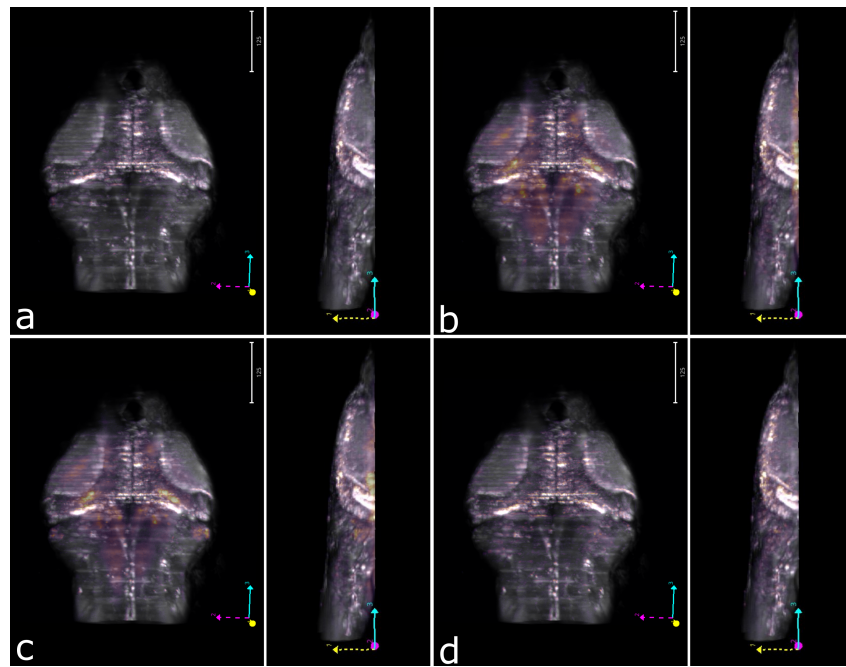


Figure 4.10: A 6dpf PTZ treated zebrafish larva is imaged over  $400 \times 400 \times 100\mu\text{m}$ . Each volume contains 36 images and is acquired with a spacing of  $2.78\mu\text{m}$ . A 5 ms exposure time was used for this data. (a)-(d) are four consecutive time points to demonstrate that our system is able to capture abnormal neural activities of the central nervous system of the zebrafish larva.

# CHAPTER 5

## SINGLE OBJECTIVE MULTI-DIRECTION ILLUMINATION LIGHT SHEET MICROSCOPY

LSFM is the best method for high-speed imaging of thick, live samples over a large field of view. The requirement for longer working distance objective lenses that limits the resolution to the cellular level in the lateral direction and reduces its resolution by a factor of 2 to 3 in the axial direction ( $\approx 0.6\mu\text{m}$  laterally,  $4\mu\text{m}$  in axial direction with a 0.5 NA objective lens). Previously, Keller et al [114] attempted to solve this problem while maintaining a high imaging speed, using four objective lenses and four cameras to achieve a 430 nm resolution over a  $266\mu\text{m}$  field of view. A different approach is combining SIM with LSFM to boost the system's spatial resolution. At the same time, this could also extend the imaging depth of the SIM and increase tolerance to the sample thickness. The lattice light sheet microscope (LLSM), developed by Betzig et al., uses a custom-made illumination objective lens that fits together with a 1.1 NA detection objective lens to achieve subcellular resolution but sacrifices the field of view. In LLSM, structured illumination was used in the context of the single-direction illumination pattern. This means that the resolution gain is not isotropic (lateral resolution of 150nm in x, 230nm in y, and 280nm axial resolution, over  $80\mu\text{m}$  field of view). In order to fully take advantage of SIM, a set of illumination patterns with at least three orientations are needed. LLSM is not designed to achieve sub-cellular resolution while maintaining large fields of view, and is insufficient for certain research endeavors.

For example, it cannot resolve individual axons while also viewing the entire mid-brain of the zebrafish larva. In order to differentiate between individual overlapping axons in the larval zebrafish central nervous system, the resolving power of an imaging system should be less than 200nm, because the diameter of these axons is around 400nm. Further, the above solutions require complicated sample mounting procedures. The cost and complexity of these systems renders them virtually inaccessible. In this chapter, We will present and describe a single-objective LSFM that is combined with structured illumination microscopy (SR-SIM) using commercially available micro-prisms and an objective lens. This system allows for imaging of thick multi-cellular specimens with multi-direction illumination with a measured resolution of 417nm in lateral direction and 1.64 $\mu$ m in axial direction under LSFM mode, under LSFM-SIM mode a 313nm lateral resolution with 1.64 $\mu$ m axial resolution is achieved.

## 5.1 Optical Design

Here, we combine SR-SIM and LSFM in a single objective configuration. This configuration works by using a reflective surface to create a light sheet. It was first shown by Galland et al [57]. Further variations [209, 102, 132] have been developed for cellular imaging. Instead of a single prism, we used multiple to create multi-directional illumination LSFM. We steer the beam to the different prisms with a tip/tilt mirror. This allows for the creation of patterns at different orientations, so that we can achieve isotropic SIM and be more robust to stripe artifacts induced by the sample structures.

Fig.5.1 shows the simplified optical design of the microscope. A Cobolt Skyra laser from Hubner Photonics was used, which has three wavelengths (488nm, 561nm, 638nm). The laser emits a beam with a 0.7mm diameter ( $1/e^2$ ), which is then focused by a 35mm lens and filtered by a 50 $\mu$ m pinhole. After the pinhole, a 50mm lens is used to collimate the laser to 1mm diameter. A 100mm cylindrical lens then focuses the laser light into a line profile. The line profile should have a length of 1mm and a width of 62 $\mu$ m at the focus of the cylindrical lens, according to  $2\omega_0 = \frac{4\lambda f}{\pi D}$ . The cylindrical lens is mounted on a motorized rotation stage. Additionally, a two-axis translation stage is used to adjust the position of the rotation stage. T1 (35mm,150mm) and T2 (125mm,250mm) are two sets of magnifying lens pairs used to enlarge the beam to 8.57mm in length and 0.532mm in width at the spatial light modulator (SLM). In this system, the laser light is modulated using a combination of a polarized beam splitter (PBS), and a half wave plate together with the SLM, the SLM acts as a half-waveplate with a fast axis that switches between s-polarization

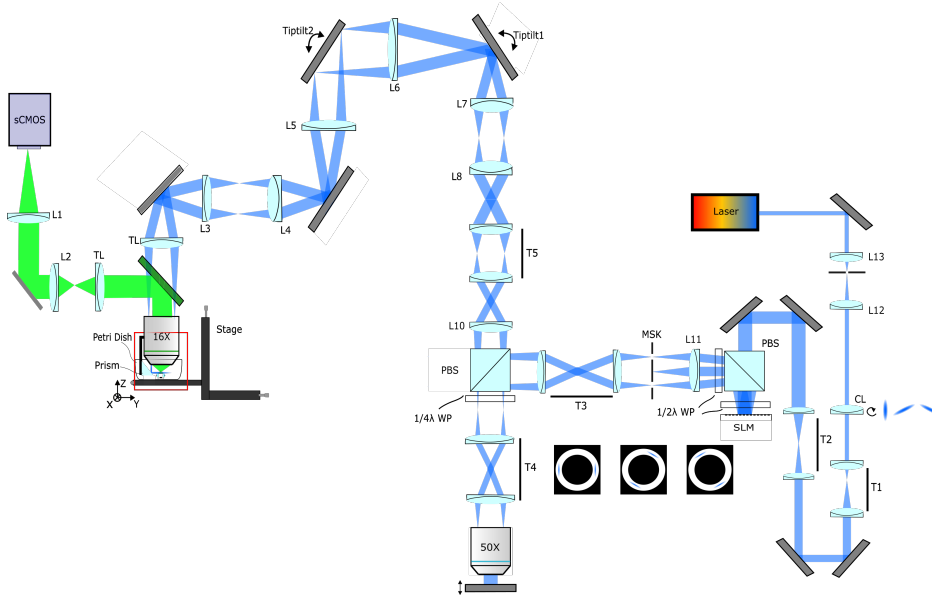


Figure 5.1: Schematic of the simplified optical setup. A Nikon  $16 \times 0.8\text{NA}$  water dipping objective was used as the illumination as well as the imaging objective lens, and a  $0.6 \text{ NA } 50\times$  Nikon air objective lens was used to construct the remote focusing system. L1: 300mm, L2 = L4 = L5 = L8: 100mm, L3: 80mm, L6: 75mm, L7:30mm, L10: 150mm, L11: 200mm, L12: 35mm, L13: 50mm, T1:35mm,150mm, T2:125mm,250mm, T4:100mm,100mm, T3 = T5: 200mm,200mm, CL:100mm

and p-polarizations. L11 is a 200mm focal length lens to collimate the diffracted light onto the conjugated back pupil of the objective lens. A mask with an annular structure is used to block the unwanted diffracted light. Then, two sets of relay lens pairs (T3: 200mm and T4: 100mm ) are used to image the diffracted light onto the back pupil of a  $50 \times 0.6 \text{ NA}$  remote focusing objective lens (Nikon TU Plan ELWD).

In order to have the light sheet beam waist at the center of the imaging area, we employed remote focusing. A two objective lens remote focusing configuration was used. A more detailed explanation of the remote focusing system will be given in the section 5.3.1. A PBS with a quarter waveplate is used to ensure all of the light passes through. A mirror is placed at the front focal plane of the remote focusing objective, mounted on a piezo stage, so that the focus for the illumination objective lens can be adjusted. L10 is a 150mm focal length lens, and T5 consists of a 200mm focal length lens pair. The image plane of the objective lenses is transferred on to a tip tilt mirror by L8 and L7, which are

100mm and 30mm lenses. The mirror will allow us to adjust the tip and tilt of the light sheet at the front focal plane of the illumination objective lens. Then, a 75mm focal length lens is used to image the conjugated back pupil plane of the objective lens onto a second tip tilt mirror, which allows for steering the beam at the front focal plane of the objective lens. This is further relayed onto the illumination objective lens using a pair of 100mm lenses (L4 and L5) and a 80mm lens. Here, a 200mm tube lens is used in combination with the 16x objective lens. For the imaging path, after the 200mm focal length tube lens (TL), the final image is magnified by a factor of 3 using a pair of lenses (L1: 300mm, L2: 100mm). The overall magnification from the SLM to the front focal plane of the 16 $\times$  objective lens is 66.67 and the magnification between the remote focusing objective imaging plane and the illumination objective lens meets the condition of the remote focusing, which is 1.33. The overall magnification of the imaging path is 48 $\times$ , this will give an effective pixel size of 135nm. The resulting imaging area on the camera is 277 $\mu$ m.

## 5.2 Designing the Field of View

As previously discussed, the field of view is always inversely proportional to the thickness of the light sheet. This is shown in Fig 5.2. Therefore, choosing a light sheet that is large enough to cover the desired imaging area becomes very critical. A sheet with a larger-than-necessary field of view would lower the optical sectioning performance of the microscope. We aim to develop a light sheet capable of imaging a field of view around 200 $\mu$ m, meaning that the thinnest suitable light sheet should not be less than 5 $\mu$ m thick ( $Z_R = \frac{\pi\omega_0^2}{\lambda}$ ). In order to achieve sub-200nm lateral resolution, an objective lens with a moderately high numerical aperture is necessary. According to the equation  $d_{\text{lateral}} = \frac{\lambda}{2NA}$ , the NA of the imaging objective lens should be no less than 1.28. However, all of the commercially available high-NA objective lenses ( $NA \geq 1.2$ ) have very short working distances. This makes them unsuitable for imaging thick multi-cellular samples. For this reason, we will use SIM to achieve sub 200 nm resolution with a moderate NA long working distance objective. Further, as previously discussed, the conventional sample mounting procedure used with multiple-objective systems is complex and time-consuming, inspiring us to develop a LSFM system that uses only one objective and allows for simpler and more cost-effective sample mounting.

The single objective configuration (soSPIM) using a micro-reflective cavity was first shown by Galland et al [57]. This concept was originally borrowed from reflective light sheet microscopy, where a reflective surface (polished can-

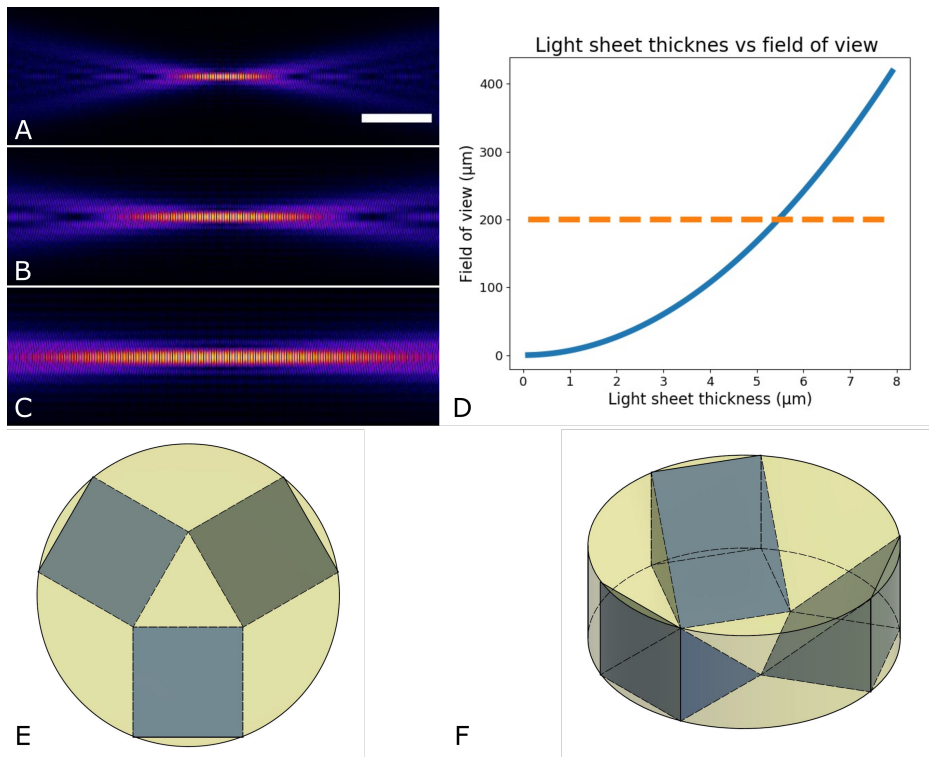


Figure 5.2: Illustration of light sheet thickness and field of view (FOV). Here, FOV is calculated using double the Rayleigh range. (A)-(C) shows the absolute value of the electric field amplitude of a light sheet with FOV of  $10\mu\text{m}$ ,  $20\mu\text{m}$ ,  $40\mu\text{m}$  respectively. (D) shows that the thickness of the light sheet is inversely proportional to the FOV. (E)-(F) show that  $500\mu\text{m}$  prisms can be fit into the imaging volume (in yellow) of the objective lens.

tilever) was first introduced to overcome the geometrical limit of fitting two high-NA objective lenses together, in order to further improve the performance of localization-based super resolution LSM [24]. This approach was successful in generating an ultra-thin light sheet and improving light-collecting efficiency [60].

In the single-objective configuration, only one objective lens is used as both the illumination and the detection objective lens. A micro-prism is used to direct the illuminating sheet laterally at the sample plane so that the beam is coaligned with the focal plane of the objective. Therefore, in order to be able to image throughout the sample, we chose a 0.8 NA water dipping objective lens (CFI75 LWD 16X W) which has a 3mm working distance and a field of view of 1.375mm. This actual field of view of the objective lens can be acquired

from the datasheet of the objective lens or by using the formula described in Eqn. 5.1, where FN refers to the field number of the objective lens, and M is the magnification of the objective lens.

$$FOV_{Actual} = \frac{FN}{M} \quad (5.1)$$

For our setup, instead of using a single prism, three micro-prisms are used to direct the light from multiple directions. These prisms are positioned 120 degrees apart from each other. Here, we need to make sure that the prisms are sized and positioned appropriately to fit into the FOV of the objective lens, so that the illumination area and imaging depth in the system are sufficient to image thick, multi-cellular specimens. The most ideal configuration consists of three  $500\mu\text{m}$  prisms, positioned as an equilateral triangle. This allows for an imaging volume with a depth of  $500\mu\text{m}$ , as shown in Figure.5.2

### 5.3 3D Imaging with Reflected Light Sheet Microscopy

One common issue with such a configuration is that the light sheet length is rather limited. Because the beam waist would be positioned at the prism, the effective area being illuminated by the light sheet is only half of the Rayleigh range.

Therefore, the beam waist needs to be shifted to the center of the imaging area. In order to accomplish this, we implemented remote focusing where the beam waist position can be adjusted with minimal aberration introduced [16, 17].

### 5.4 Remote Focusing for 3D Imaging

Figure 5.5 shows an emitter placed at some location that is  $\mathbf{r}$  away from the focus of the lens. This will result in a path length difference (PD) compared to the light that is traveling from the focal point of the lens. The PD can be calculated using Equation 5.2 [15].

$$PD = |\mathbf{w}| - F = |\mathbf{f} - \mathbf{r}| - F = (F^2 - 2\mathbf{f} \cdot \mathbf{r})^{0.5} - F \quad (5.2)$$

Here,  $\mathbf{f}$  is the vector from a general focal point to the principal surface of the lens. Its magnitude is F.  $\mathbf{w}$  is the vector from the emitter to the principal surface

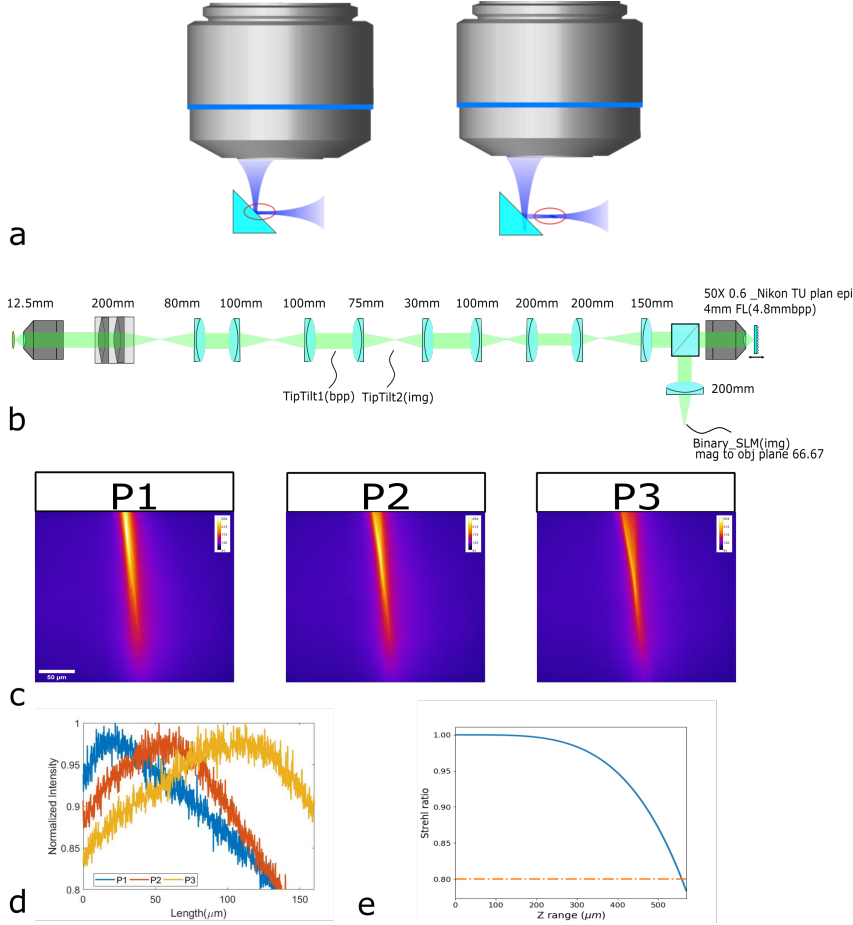


Figure 5.3: (a). Illustration of light sheet beam waist shifting. (b). Optical design of remote focusing. (c) Gaussian beam waist shifting at three different positions  $50\mu\text{m}$  apart from each other. (d) Normalized line intensity profile along the illumination direction. (e) Simulation of the Strehl ratio as a function of point source position using 0.45 illumination NA in water for 488nm laser.

of the lens.  $\mathbf{r}$  is the vector describe the displacement between these two points, its magnitude is  $r$ .  $\mathbf{f}$  in spherical polar form is  $F(\sin\theta\cos\phi, \sin\theta\sin\phi, \cos\theta)$ . Here, only the on axis case is considered, and we can write the PD in the following form:

$$PD = F\left\{1 - \frac{2}{F}z\cos\theta + \frac{r^2}{F^2}\right\}^{0.5} - F \quad (5.3)$$

After expansion, the PD can be expressed as, when  $r \ll F$

$$PD \approx -\frac{\mathbf{f} \cdot \mathbf{r}}{F} = -z\cos\theta \quad (5.4)$$

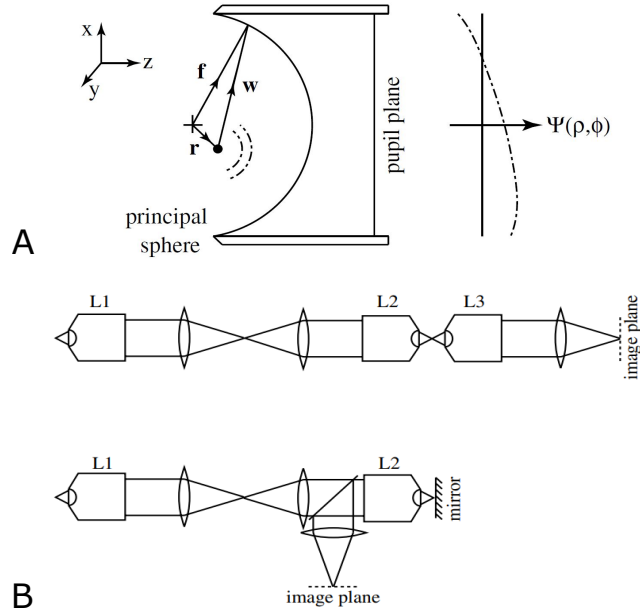


Figure 5.4: A. diagram of a general microscope system. B. diagram of remote focusing systems using three objective lenses and two objective lenses.

Using the PD we can express the wavefront phase profile using Equation 5.5, since  $\sin\theta = \rho\sin\alpha$ , where  $\alpha$  is the semi aperture acceptance angle of the lens,  $\rho$  is the normalized pupil radius ( $0 < \rho < 1$ )

$$\Psi(\rho, \phi; z) \approx kn\sin\alpha \left\{ z\sqrt{\frac{1}{\sin^2\alpha} - \rho^2} \right\} \quad (5.5)$$

Here  $n$  is the refractive index and  $k$  is vacuum wavenumber of the light. When a remote focusing is constructed as shown in Figure. 5.4. The phase profile of the pupil function from the objective lens can be written as:

$$\Psi_1(\rho_1, \phi) = kn_1\sin\alpha_1 \left\{ z\sqrt{\frac{1}{\sin^2\alpha_1} - \rho_1^2} \right\} \quad (5.6)$$

and if the second objective lens uses a different immersion media. The phase profile from the second objective lens can be written as follows:

$$\Psi_2(\rho_2, \phi) = kn_2\sin\alpha_2 \frac{n_1}{n_2} \left\{ z\sqrt{\frac{1}{\sin^2\alpha_2} - \rho_2^2} \right\} \quad (5.7)$$

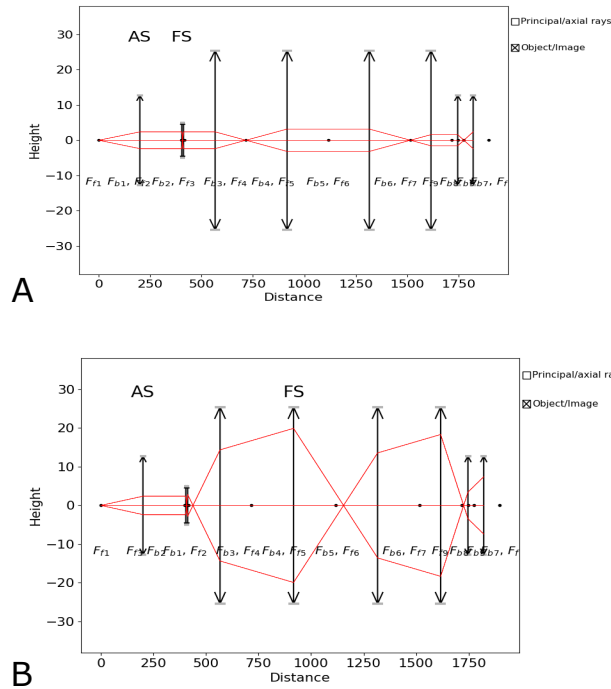


Figure 5.5: Diagram of optical ray tracing shows that 2 inch optics are needed. The angle of  $F_{f1}$  is 1.365 degrees, which corresponds to the diffraction angle when the highest grating frequency is used for this system. This simulation is simulating from the conjugated image plane (SLM) to lens in front of tip-tilt mirror that is conjugate to the front focal plane of the illumination objective lens, This simulation consist a 200mm lens (D=1inch), a pair of 50× objective lenses, 150mm, a set of 200mm lenses and a 100 mm lens that are 2 inch in diameter. Then a 30mm and a 75mm lens with 1 inch diameter. Optical ray tracing of the remote focusing system without axial shift. (b) Optical ray tracing of the remote focusing system with 750 $\mu$ m axial shift.

In a perfect remote focusing system, as shown in Figure 5.4  $M = \frac{\rho_1}{\rho_2} = \frac{\sin \alpha_2}{\sin \alpha_1}$ , an image of the emitter can be formed at the focal plane of the second objective lens without aberration. Thus, this process can also be thought of as two separate microscope systems back-to-back, such that the first magnifies the object by a factor  $M_1$  and the second demagnifies it by  $M_2$ . In this situation, both the lateral and axial magnifications of the microscope combination yield the same value of  $n_1/n_2$ , as required for perfect imaging of the three-dimensional domain. In effect, the spherical aberration introduced by the first system is directly compensated for by that introduced by the second. Since a water immer-

sion objective lens is being used as the primary objective lens, the magnification ( $M_{RR}$ ) between the remote focusing objective lens imaging plane and the primary objective lens's focal plane needs to be equal to the ratio of the immersion media refractive indices [15].  $n_1$  is the refraction index of the immersion media of the primary objective lens (1.33 for water) and  $n_2$  is the refraction index of the remote focusing objective lens (1 for air).

$$M_{RR} = \frac{n_1}{n_2} \quad (5.8)$$

Figure 5.3 shows the optical design of the remote focusing system. This system is tested with a fluorescent dye sample, showing a focus shift of the Gaussian beam waist across three positions with a  $50\mu\text{m}$  difference from P1 to P2, and from P2 to P3. Figure 5.3 shows that we are able to shift a Gaussian beam at least  $500\mu\text{m}$  with a 0.45 illumination NA, resulting in a light sheet with a thickness of  $542\text{nm}$ .

Since the structured light will be created by a spatial light modulator, we need to make sure that the largest pattern frequency can be used in the system, because as the remote focusing is performed, the beam waist position also changes in relation to the focal plane of the objective lens. The diffracted light will either converge or diverge as it passes through our optical system. Therefore, we need to make sure that the light will not be clipped by the lenses in between the objective lenses as the beam waist of the light sheet is shifted. In order to verify the design, a ray tracing simulation is performed, shown in Figure 5.4.

## 5.5 Illumination Synchronization

Here, the SLM is a binary microdisplay, which means that each pixel of the SLM can exist in only one of two states, on or off. The pixel is switched on and off by changing the polarity of the electrical field across it. In this way, the incident light is switched in polarization so it exits the other face of the beamsplitter cube. To prevent damage to the Liquid Crystal (LC), the net bias across the pixel must equal zero over time. This means that time between the pixels being an on state and off state should be equal for each activation period. Therefore, we must synchronize the SLM with the pixel state using the laser and the camera exposure to capture one image. Figure 5.6 shows how the illumination of the microscope is synchronized.

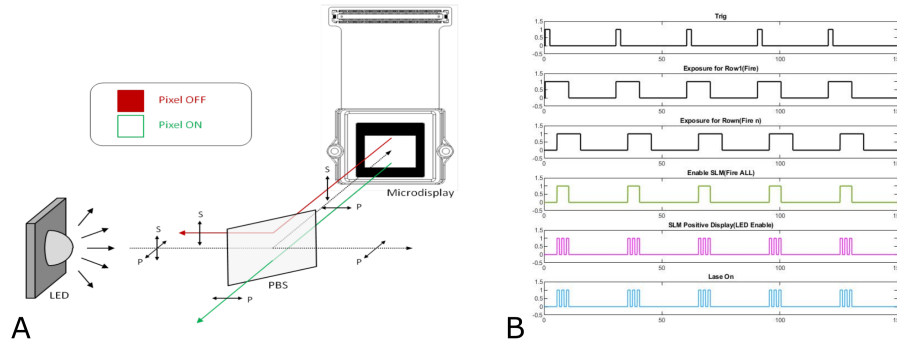


Figure 5.6: (A) Illustration of binary SLM amplitude modulation of the illumination light. (B). Microscope synchronisation trigger sequence. (A) is acquired from Forth dimension displays manual.

## 5.6 Multi-Direction Light Sheet Illumination

As mentioned earlier in the chapter, the light sheet will be directed using three prisms that are mounted at the focal plane of the objective lens. This also requires that the beam is oriented to the correct direction for each prism. Since the SLM is being operated in the amplitude modulation mode, the orientation of the light sheet can be changed by switching the display pattern on the SLM. This would allow us to switch the illumination angle rapidly. This is achieved using a microcontroller board (TriggerScope 4). However, the light throughput is rather low for this approach. In order to overcome this issue, we used a rotation stage and achromatic cylindrical lens to rotate a focused line profile on the SLM. A comparison is shown in Figure. 5.7 where we imaged fluorescence dye sample (10mM Alexa 488 mixed with 1% argrose gel in the ratio of 1 : 100) with the same laser intensity and camera exposure time (20 mw,100 ms exposure time). Here, the measured intensity is increased by a factor of 3. Figure.5.8 shows the multi-direction light sheet illumination working principle, where a laser beam with a line profile is oriented in 0, 120, 240 degrees. Then the laser beam is steered at the conjugated back pupil plane of the objective lens, so that the beam is reflected by hypotenuse of the micro prism that is coated with aluminum.

The cylindrical lens can create a  $8.57 \times 0.532mm^2$  line profile at the SLM, which is conjugated to the front image plane of the illumination objective lens. This translates to a sheet  $4.65\mu m$  in thickness (FWHM). This can be further adjusted by controlling the number of the on-state pixels of the SLM in the

width direction of the light sheet. In addition to adjusting the thickness of the light sheet, different structured patterns can be displayed to create illumination patterns so that SIM can be implemented for all directions.

In order to quantify the light sheet thickness, a fluorescent dye sample is used to measure the light sheet thickness as well as the width. Here, the light sheet has a thickness of  $4.768 \pm 0.177 \mu\text{m}$  and a width of  $63.93 \pm 4.76 \mu\text{m}$  in FWHM. This value is close to the designed parameter of the light sheet, which should have a thickness of  $4.697 \mu\text{m}$  in thickness and  $75.65 \mu\text{m}$  in width. This result is shown in Figure 5.9 The multi-direction light sheet illumination is shown using a fluorescent dye sample mixed with yellow-green fluorescent beads.

## 5.7 Imaging Area of the Multi-Direction Light Sheet

In conventional light sheet microscopy, the imaging area is defined by the light sheet width as well as by the Rayleigh range in combination with the overall magnification of the sensor size. Currently, the over all magnification of our setup is  $48\times$ . This will result in a  $276.5 \mu\text{m}$  FOV with a pixel size of  $135\text{nm}$ . The light sheet is  $75 \mu\text{m}$  in width and  $278 \mu\text{m}$  in length. When multi-direction illumination is implemented, the penetration depth increase. Here, we use the average of multiple images from different illumination directions to fuse into one final image. This is shown in Figure 5.10.

## 5.8 Point Spread Function of the System and 3D Imaging

Here, we imaged  $200\text{nm}$  yellow-green fluorescent micro-spheres to quantify the performance of the microscope. 10 beads are selected at random locations. The average FWHM is  $417 \pm 23\text{nm}$  in the y lateral direction,  $406 \pm 17\text{nm}$  in the x lateral direction, and  $1.64 \pm 0.09 \mu\text{m}$  in the axial direction. The representative line profile is plotted in Figure 5.11 and the box plot shows the random selection of 10 measurements across the  $10 \mu\text{m}$  image stacks is shown in Figure 5.11(C). We also imaged a cerebellum organoid, which was fixed on day 7 with 4% PFA and stained for neuronal marker Tuji1 with Alexa 488 dye. A maximum projection over  $20 \mu\text{m}$  is shown here.

## 5.9 Structured illumination with LSFM

This will provide the boost in isotropic resolution necessary to fully realize the potential of the system. Here, we use fluorescent dye phantom to show that a sinusoidal pattern can be created from three directions 120 degrees apart from each other. In order to show this, a shorter pattern wavelength is used here. A 20 pixel pattern at the SLM with a wavelength of  $1.22\mu m$  is shown in Figure. 5.13. We use a line profile to show a set of three phases. Further, we imaged a fluorescent beads sample and we show that the system is able to achieve a resolution boost of 1.2x in all lateral directions. Further, a line intensity profile is compared with single-direction LSFM illumination in Figure.5.13. We achieved a FWHM measurement of  $317 \pm 32nm$  with 10 measurements of 200nm beads. The theoretical resolution should be 268nm after a 1.2 times resolution boost. A finer pixel pattern can be used to further improve the resolution a to  $2\times$  boost, however a 4 micron light sheet requires a mask with tight tolerance at the conjugated back pupil plane. The current rotation stage for the cylindrical lens has a axial wobble of 0.103 degree, which will translate to a shift of  $500\mu m$  at the SLM. This will cause displacement of the diffraction order from its designed position, which will not pass through the mask as result. However, a light sheet with a shorter Rayleigh range uses a mask with larger openings, which will result in less necessity for accuracy of the stage for the cylindrical lens.

Currently, this system is capable of imaging a thick biological specimen over a  $277\mu m$  FOV with axial range of 50. The system has a  $1.2\times$  resolution boost isotropically in SIM mode, and is synchronized using both electrical signals and software commands from the computer. A faster imaging speed can be achieved by using only electrical signals for all the parts of the microscope.

## 5.10 Investigation of Isotopic Resolution

In this section, I present the results of a working simulation of the LSFM-SIM microscope that is in conformity with the theoretical principles upon which this technique relies. To demonstrate the working of the microscope, I programmed a computer model in Python that simulates the effective PSF and OTF of the system using different structured illumination patterns. The resolution of the system can be adjusted based on the application needs. The highest isotropic resolution of the system without tiling the illumination light sheet is shown in Figure. 5.15. The system should be able to achieve a lateral resolution of 151nm and axial resolution of 767nm using a 5 pixel square lattice. A greater isotropic

resolution of 167 nm over 476nm can be achieved when a 6 pixel hexagonal lattice pattern is used.

## **5.II Conclusion**

In conclusion, we have demonstrated a single objective light sheet microscope. This instrument can use the conventional mounting for biological imaging, and is the first of its kind which has successfully combined super resolution structured illumination with LSM. We tested the performance of the system using fluorescence beads sample, and we can achieve a resolution of 312nm in all lateral directions, with an axial resolution of  $1.4\mu\text{m}$ . We further show that this microscope is capable of imaging thick, multi cellular specimens with great penetration depth.

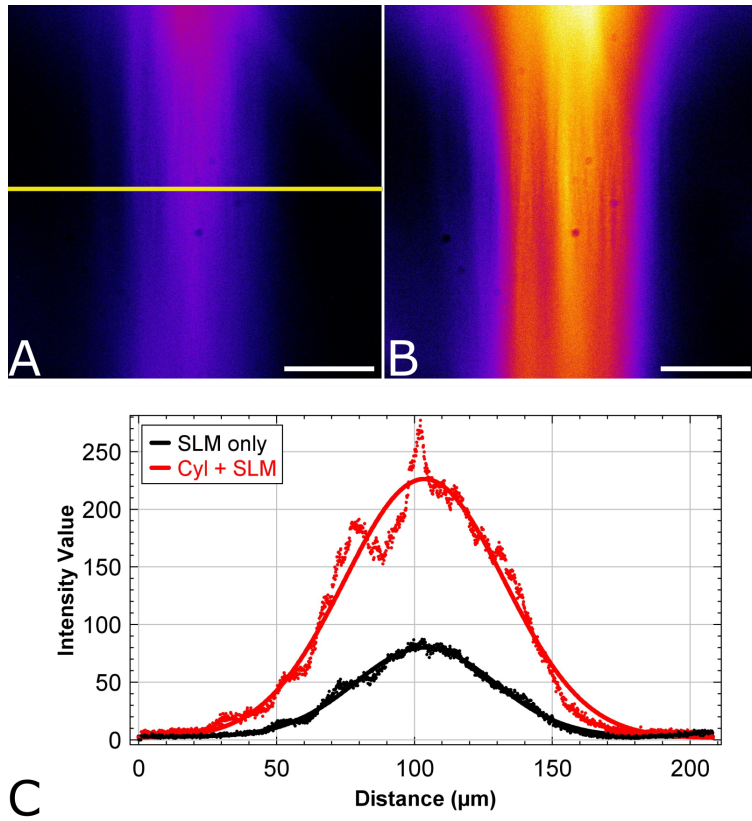


Figure 5.7: (A) light sheet created using SLM only. (B) light sheet created using cylindrical lens and SLM. (C) line intensity profile plots at location noted in (A) for both cases. The thickness of the light sheet is  $5\mu\text{m}$  and the scale bar is  $50\mu\text{m}$

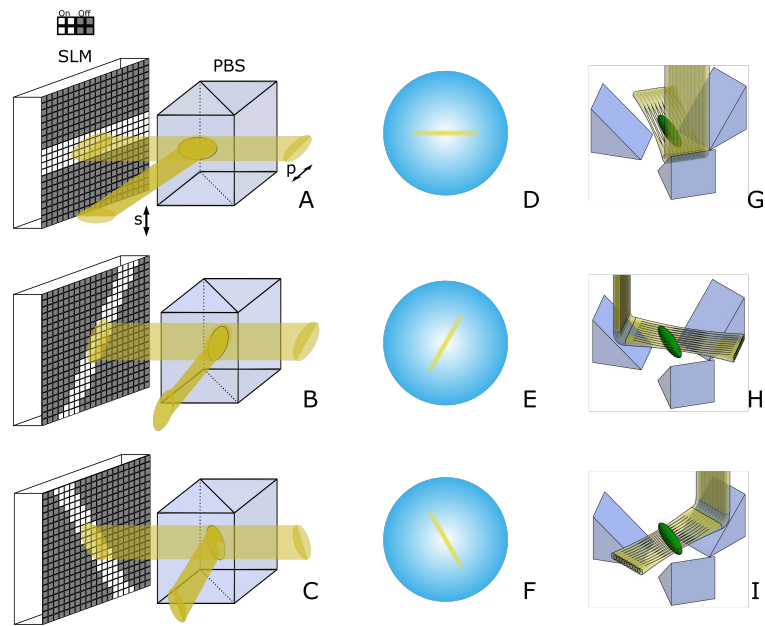


Figure 5.8: (A)-(C) Illustration of light modulation of the SLM for multi-direction illumination. (D)-(E) Diagrams showing the excitation beam in the objective back pupil plane for a thin sheet in each of the three beam directions. (G)-(I) Simplified drawing showing the placement of the prisms below the objective, an SI light sheet (yellow) and the sample (green).

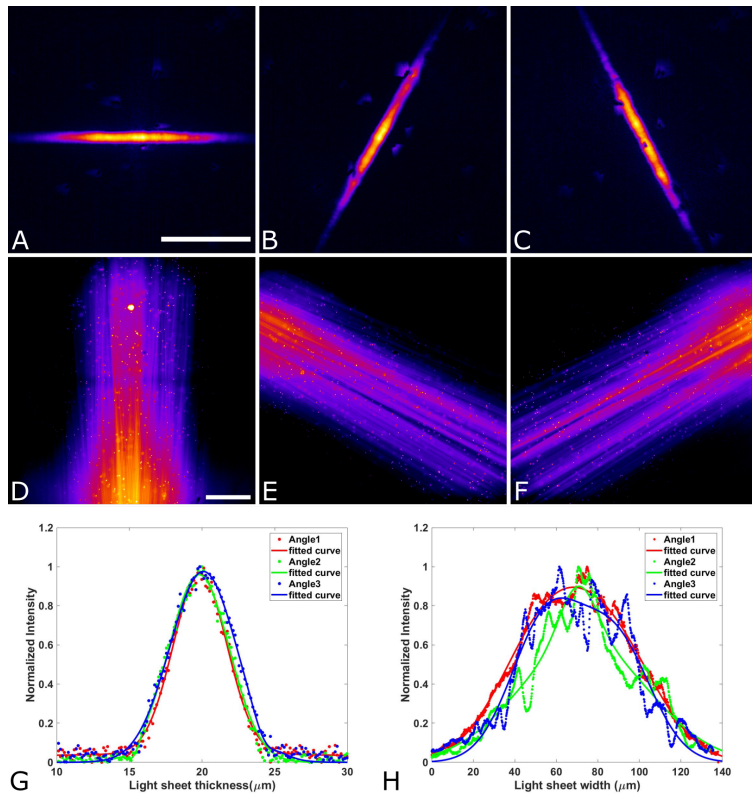


Figure 5.9: (A)-(C) Light sheet profile for three illumination directions (Angle 1, Angle 2, Angle 3). (D)-(E) Illuminating light sheet with respect to (A)-(C). (G) Normalized line intensity profile of the light sheet thickness for three different angles, FWHM  $4.768 \pm 0.177 \mu m$  (H) Normalized line intensity profile of the light sheet width for three angles, FWHM  $63.93 \pm 4.76 \mu m$ . Scale bar in (A) and (D) is  $50 \mu m$ .

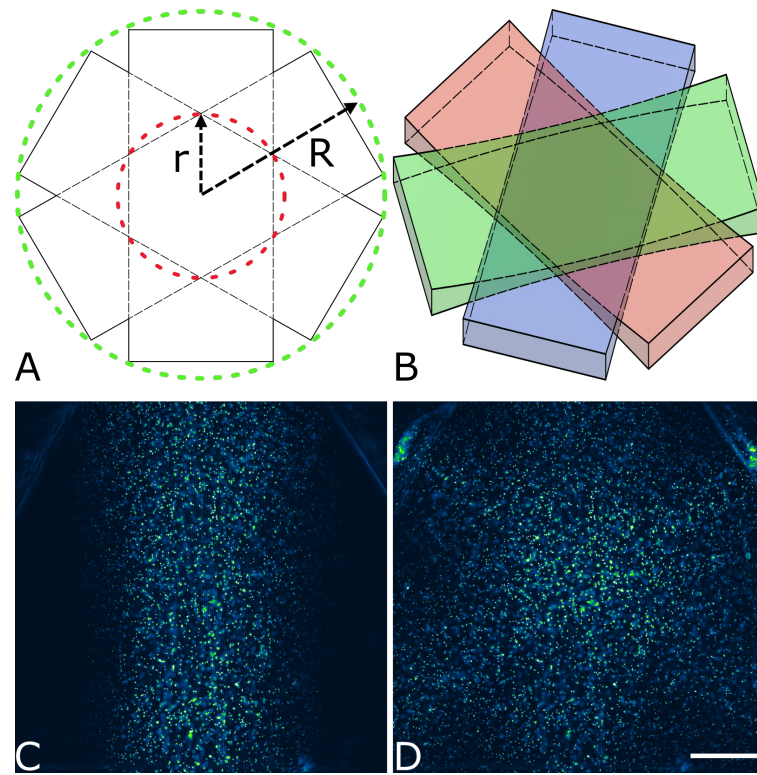


Figure 5.10: (A)-(B) Illustration of the imaging area coverage. The red dotted circle indicates the conventional single-direction light sheet coverage and the green dotted circle indicates the multi-direction imaging area coverage. (B). 3D cartoon shows the overlap of the three illumination angles. Angle 1 in blue, Angle 2 in red, Angle 3 in green. (C)-(D). Comparison of multi-direction illumination coverage compared to single-illumination light sheet imaging area coverage. Scale bar is  $50\mu m$ .

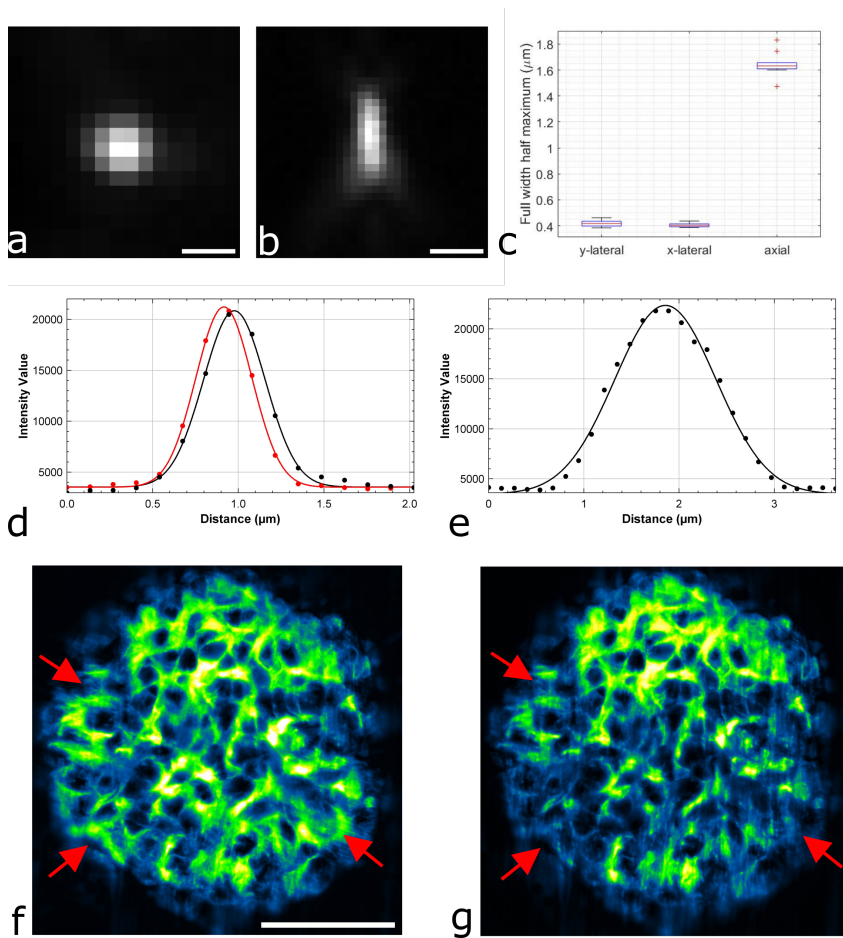


Figure 5.11: (a)-(b) lateral and axial point spread function. (c). box plot of the 10 measurements of the lateral and axial profile of the point spread function. (d) representative line profile of lateral point spread function, horizontal in red and vertical in black. (e). line profile of axial point spread function. (f) maximum intensity projection of  $20\mu m$  image stack of 7 day organoid with multi-angle illumination (g). maximum intensity projection of  $20\mu m$  image stack with uni-direction illumination light sheet. Scale bar is  $1\mu m$  in (b)

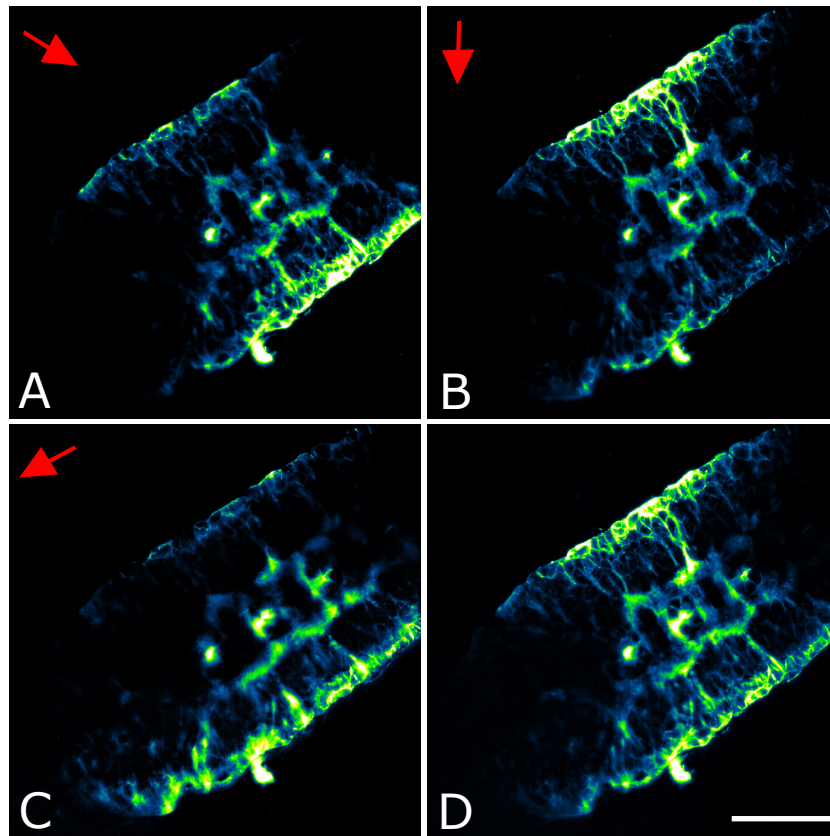


Figure 5.12: (a)-(c). maximum intensity projection of  $50\mu m$  image stack with three directions light sheet illumination, the red arrow is indicating the illumination direction of the light sheet. (d). shows the fused imaging with multi-direction illumination. Scale bar is  $50\mu m$  in (d)

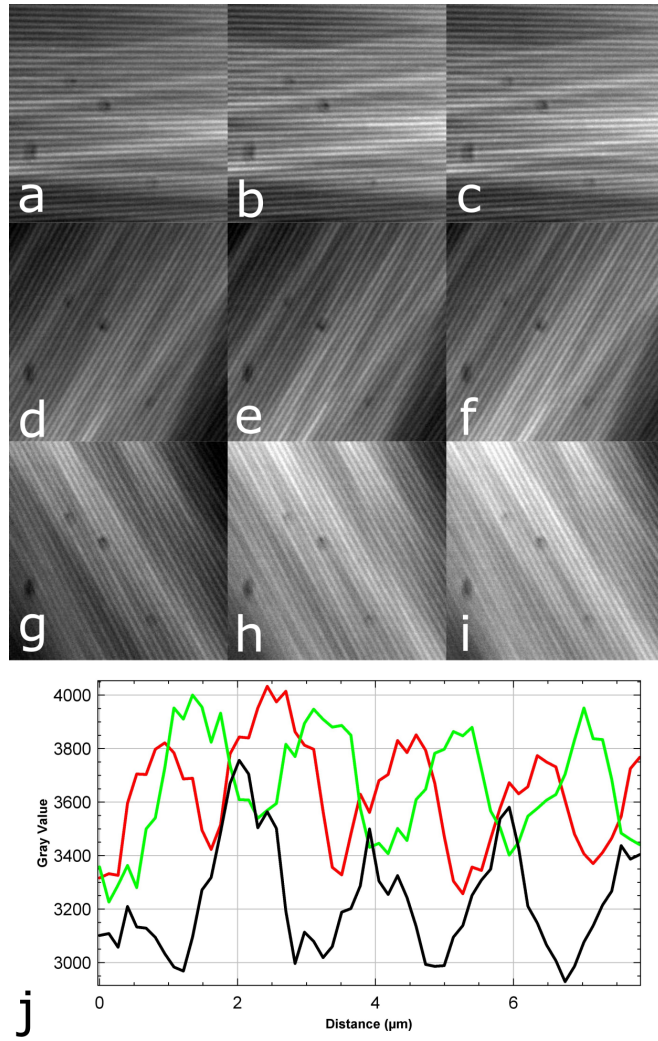


Figure 5.13: (a)-(i) structured illumination with LSFM in three orientations and three phases. The line intensity profile of a set of three phases are shown in (j)

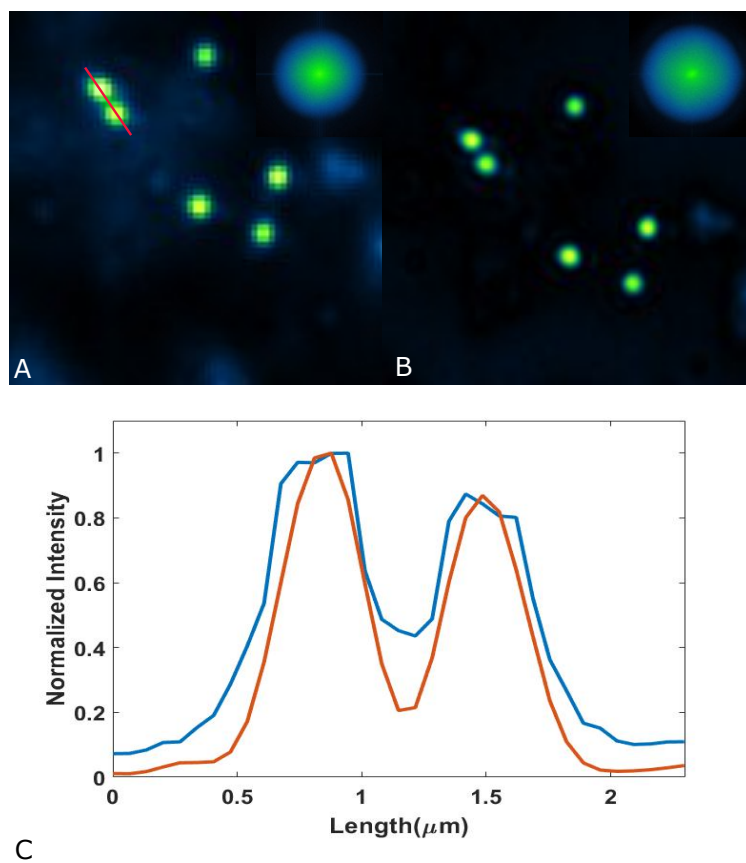


Figure 5.14: (A)-(B) Comparison of fluorescence beads image using LSFM and SIM-LSFM. (A) Beads image acquired using LSFM (B) is reconstructed beads image with SIM-LSFM. (C) The normalized line intensity profile of two beads at noted location in (A).

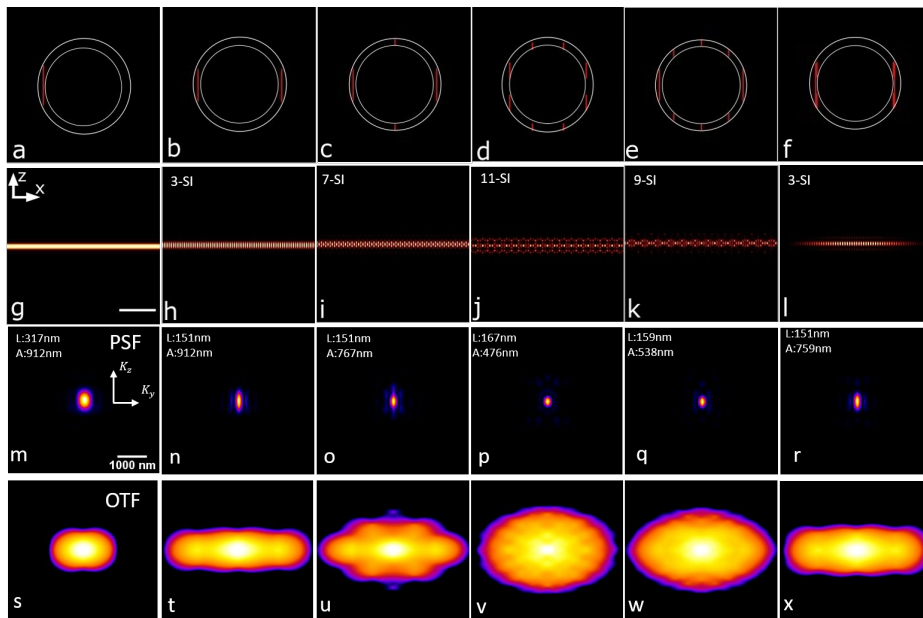


Figure 5.15: Simulation of optical lattice light sheet. (a)-(f) shows the illumination pattern at the back-pupil plane of the excitation path. (g)-(l) lattice light sheet intensity pattern at the front focal plane. (m)-(r) effective point spread function (s)-(x) optical transfer function for different lattice light sheets.

# CHAPTER 6

## CONCLUSION

In conclusion, we presented theory and experimental results of LSFM techniques as applied to the imaging of thick, living multi-cellular organisms for biological research. In Chapter 1, we introduced the concept of light microscopy and reviewed the history of its development into modern microscopy techniques. We also reviewed the current state of research development of this technology. Further, we introduced superresolution microscopy and conducted an overview of various methods and configurations. In Chapter 2, we demonstrated the implementation of LSFM with SI. Specifically, we discussed the application of this technique to the imaging of neural events in the CNS of zebrafish larvae. We showed that, with our system, the contrast is improved and the speed improved enough to capture the neural activity. In Chapter 3, we presented a new approach to alleviate the occurrence of stripe artifacts in the images produced by LSFM. We achieved this using an axial dithering technique. This approach is compatible with digital scanned light sheet illumination, without any restrictions. Further, we developed a new approach to reconstruction. We used adaptive SI reconstruction, which improves the image quality and reduces stripe artifacts even further. In Chapter 4, we developed a multi-region AO correction system for ETL-based light sheet systems. With this system, we are able to reduce spatial varying aberrations caused by the ETL across the imaging FOV as well as in the axial direction. Further, we demonstrated that the system is capable of capturing zebrafish larva neural activities in three dimensions at a speed of 5 seconds per volume. In Chapter 5, we developed a single-objective light sheet microscope that is capable of performing multi-direction structured illumination. We showed improved penetration for thick samples and an isotropic resolution improvement by a factor of 1.2. Currently, the ETL-LSFM still has room for improvement. It uses a sensorless approach, so the time necessary to gather AO settings for different regions is still significant. A sensor-based sys-

tem would increase the speed. In addition, the volumetric imaging speed of the system is 5 seconds per volume. The system could be improved in the future, ideally to between 5 and 10 volumes per second. This could be achieved using an electrical signal to synchronize multiple devices within the microscope. For multi-direction LSFM with SIM, the resolution improvement is limited to a factor of 1.2. In the future, this should be increased to a factor of 2. This could be accomplished by employing a rotation stage with minimal axial wobble, or by using a powerful laser.

# BIBLIOGRAPHY

- [1] E. Abbe. “Beiträge zur Theorie des Mikroskops und der mikroskopischen Wahrnehmung”. In: *Archiv für Mikroskopische Anatomie* 9.1 (Dec. 1873), pp. 413–468. ISSN: 0176-7364. DOI: 10.1007/BF02956173. URL: <https://doi.org/10.1007/BF02956173>.
- [2] Sara Abrahamsson et al. “Fast multicolor 3D imaging using aberration-corrected multifocus microscopy”. In: *Nature Methods* 10.1 (Jan. 2013), pp. 60–63. ISSN: 1548-7105. DOI: 10.1038/nmeth.2277. URL: <https://doi.org/10.1038/nmeth.2277>.
- [3] Sara Abrahamsson et al. “Multifocus structured illumination microscopy for fast volumetric super-resolution imaging”. In: *Biomedical Optics Express* 8.9 (Sept. 2017), pp. 4135–4140. DOI: 10.1364/BOE.8.004135. URL: <http://www.osapublishing.org/boe/abstract.cfm?URI=boe-8-9-4135>.
- [4] Misha B. Ahrens et al. “Whole-brain functional imaging at cellular resolution using light-sheet microscopy”. In: *Nature Methods* 10 (2013), p. 413. DOI: 10.1038/nmeth.2434. URL: <http://dx.doi.org/10.1038/nmeth.2434>.
- [5] Fernando Amat et al. “Efficient processing and analysis of large-scale light-sheet microscopy data”. In: *Nature Protocols* 10 (Oct. 2015), p. 1679. URL: <http://dx.doi.org/10.1038/nprot.2015.111>.
- [6] Daniel Aquino et al. “Two-color nanoscopy of three-dimensional volumes by 4Pi detection of stochastically switched fluorophores”. In: *Nature Methods* 8.4 (Apr. 2011), pp. 353–359. ISSN: 1548-7105. DOI: 10.1038/nmeth.1583. URL: <https://doi.org/10.1038/nmeth.1583>.
- [7] Francisco Balzarotti et al. “Nanometer resolution imaging and tracking of fluorescent molecules with minimal photon fluxes”. In: *Science* 355.6325 (Feb. 2017), p. 606. DOI: 10.1126/science.aak9913.

URL: <http://science.sciencemag.org/content/355/6325/606.abstract>.

- [8] David Bardell. “The First Record of Microscopic Observations”. In: *BioScience* 33.1 (Jan. 1983), pp. 36–38. ISSN: 0006-3568. DOI: 10.2307/1309242. URL: <https://doi.org/10.2307/1309242> (visited on 05/22/2020).
- [9] H Bateman. “HS Carslaw and JC Jaeger, Operational Methods in Applied Mathematics”. In: *Bulletin of the American Mathematical Society* 48.7 (1942). Publisher: American Mathematical Society, pp. 510–511. ISSN: 0002-9904.
- [10] Eric Betzig et al. “Imaging Intracellular Fluorescent Proteins at Nanometer Resolution”. In: *Science* 313.5793 (Sept. 2006), p. 1642. DOI: 10.1126/science.1127344. URL: <http://science.sciencemag.org/content/313/5793/1642.abstract>.
- [11] Andreas Bodén et al. “Volumetric live cell imaging with three-dimensional parallelized RESOLFT microscopy”. In: *Nature Biotechnology* (Jan. 2021). ISSN: 1546-1696. DOI: 10.1038/s41587-020-00779-2. URL: <https://doi.org/10.1038/s41587-020-00779-2>.
- [12] M.J. Booth, M.A.A. Neil, and T. Wilson. “Aberration correction for confocal imaging in refractive-index-mismatched media”. In: *Journal of Microscopy* 192.2 (Nov. 1998), pp. 90–98. ISSN: 0022-2720. DOI: 10.1111/j.1365-2818.1998.99999.x. URL: <https://doi.org/10.1111/j.1365-2818.1998.99999.x> (visited on 01/03/2019).
- [13] Martin J Booth. “Adaptive optical microscopy: the ongoing quest for a perfect image”. In: *Light: Science & Applications* 3.4 (Apr. 2014), e165–e165. ISSN: 2047-7538. DOI: 10.1038/lssa.2014.46. URL: <https://doi.org/10.1038/lssa.2014.46>.
- [14] Martin J. Booth. “Wavefront sensorless adaptive optics for large aberrations”. In: *Optics Letters* 32.1 (Jan. 2007), pp. 5–7. DOI: 10.1364/OL.32.000005. URL: <http://ol.osa.org/abstract.cfm?URI=ol-32-1-5>.
- [15] E.J. Botcherby et al. “An optical technique for remote focusing in microscopy”. In: *Optics Communications* 281.4 (Feb. 2008), pp. 880–887. ISSN: 0030-4018. DOI: 10.1016/j.optcom.2007.10.007. URL: <https://www.sciencedirect.com/science/article/pii/S003040180701005X>.

- [16] Edward J. Botcherby et al. “Aberration-free optical refocusing in high numerical aperture microscopy”. In: *Optics Letters* 32.14 (July 2007), pp. 2007–2009. DOI: 10.1364/OL.32.002007. URL: <http://ol.osa.org/abstract.cfm?URI=ol-32-14-2007>.
- [17] Botcherby Edward J. et al. “Aberration-free three-dimensional multiphoton imaging of neuronal activity at kHz rates”. In: *Proceedings of the National Academy of Sciences* 109.8 (Feb. 2012). Publisher: Proceedings of the National Academy of Sciences, pp. 2919–2924. DOI: 10.1073/pnas.1111662109. URL: <https://doi.org/10.1073/pnas.1111662109> (visited on 05/30/2022).
- [18] Matthew B. Bouchard et al. “Swept confocally-aligned planar excitation (SCAPE) microscopy for high-speed volumetric imaging of behaving organisms”. In: *Nature Photonics* 9.2 (Feb. 2015), pp. 113–119. ISSN: 1749-4893. DOI: 10.1038/nphoton.2014.323. URL: <https://doi.org/10.1038/nphoton.2014.323>.
- [19] N. Bourg et al. “Direct optical nanoscopy with axially localized detection”. In: *Nature Photonics* 9.9 (Sept. 2015), pp. 587–593. ISSN: 1749-4893. DOI: 10.1038/nphoton.2015.132. URL: <https://doi.org/10.1038/nphoton.2015.132>.
- [20] Cyril Bourgenot et al. “3D adaptive optics in a light sheet microscope”. In: *Optics Express* 20.12 (June 2012), pp. 13252–13261. DOI: 10.1364/OE.20.013252. URL: <http://www.opticsexpress.org/abstract.cfm?URI=oe-20-12-13252>.
- [21] Stefan Bretschneider, Christian Eggeling, and Stefan W. Hell. “Breaking the Diffraction Barrier in Fluorescence Microscopy by Optical Shelving”. In: *Physical Review Letters* 98.21 (May 2007). Publisher: American Physical Society, p. 218103. DOI: 10.1103/PhysRevLett.98.218103. URL: <https://link.aps.org/doi/10.1103/PhysRevLett.98.218103>.
- [22] Tobias Breuninger, Klaus Greger, and Ernst H. K. Stelzer. “Lateral modulation boosts image quality in single plane illumination fluorescence microscopy”. In: *Optics Letters* 32.13 (July 2007), pp. 1938–1940. DOI: 10.1364/OL.32.001938. URL: <http://ol.osa.org/abstract.cfm?URI=ol-32-13-1938>.
- [23] Daniel Burke et al. “Adaptive optics correction of specimen-induced aberrations in single-molecule switching microscopy”. In: *Optica* 2.2 (Feb. 2015), pp. 177–185. DOI: 10.1364/OPTICA.2.000177. URL:

- <http://www.osapublishing.org/optica/abstract.cfm?URI=optica-2-2-177>.
- [24] Francesca Cella Zanacchi et al. “Live-cell 3D super-resolution imaging in thick biological samples”. In: *Nature Methods* 8.12 (Dec. 2011), pp. 1047–1049. ISSN: 1548-7105. DOI: 10.1038/nmeth.1744. URL: <https://doi.org/10.1038/nmeth.1744>.
- [25] *CFI75 Water Dipping Series*. en. URL: <https://www.microscope.healthcare.nikon.com/products/optics/cfi75-water-dipping-series> (visited on 09/18/2021).
- [26] Tonmoy Chakraborty et al. “Light-sheet microscopy of cleared tissues with isotropic, subcellular resolution”. In: *Nature Methods* 16.11 (Nov. 2019), pp. 1109–1113. ISSN: 1548-7105. DOI: 10.1038/s41592-019-0615-4. URL: <https://doi.org/10.1038/s41592-019-0615-4>.
- [27] Bo-Jui Chang, Kevin M. Dean, and Reto Fiolka. “Systematic and quantitative comparison of lattice and Gaussian light-sheets”. In: *Optics Express* 28.18 (Aug. 2020), pp. 27052–27077. DOI: 10.1364/OE.400164. URL: <http://www.opticsexpress.org/abstract.cfm?URI=oe-28-18-27052>.
- [28] Bi-Chang Chen et al. “Lattice light-sheet microscopy: Imaging molecules to embryos at high spatiotemporal resolution”. In: *Science* 346.6208 (Oct. 2014). DOI: 10.1126/science.1257998. URL: <http://science.sciencemag.org/content/346/6208/1257998.abstract>.
- [29] Yanlu Chen et al. “A Versatile Tiling Light Sheet Microscope for Imaging of Cleared Tissues”. In: *Cell Reports* 33.5 (Nov. 2020), p. 108349. ISSN: 2211-1247. DOI: 10.1016/j.celrep.2020.108349. URL: <https://www.sciencedirect.com/science/article/pii/S2211124720313383>.
- [30] Raghav K Chhetri et al. “Whole-animal functional and developmental imaging with isotropic spatial resolution”. In: *Nature Methods* 12.12 (Dec. 2015), pp. 1171–1178. ISSN: 1548-7105. DOI: 10.1038/nmeth.3632. URL: <https://doi.org/10.1038/nmeth.3632>.
- [31] Eun-Seo Cho et al. “3DM: deep decomposition and deconvolution microscopy for rapid neural activity imaging”. In: *Optics Express* 29.20 (Sept. 2021). Publisher: OSA, pp. 32700–32711. DOI: 10.1364/

OE . 439619. URL: <http://www.osapublishing.org/oe/abstract.cfm?URI=oe-29-20-32700>.

- [32] José-Angel Conchello and Jeff W Lichtman. “Optical sectioning microscopy”. In: *Nature Methods* 2.12 (Dec. 2005), pp. 920–931. ISSN: 1548-7105. DOI: 10.1038/nmeth815. URL: <https://doi.org/10.1038/nmeth815>.
- [33] A H COONS and M H KAPLAN. “Localization of antigen in tissue cells; improvements in a method for the detection of antigen by means of fluorescent antibody”. eng. In: *The Journal of experimental medicine* 91.1 (Jan. 1950). Publisher: The Rockefeller University Press, pp. 1–13. ISSN: 0022-1007. DOI: 10.1084/jem.91.1.1. URL: <https://pubmed.ncbi.nlm.nih.gov/15395569>.
- [34] Albert H Coons, Hugh J Creech, and R Norman Jones. “Immunological properties of an antibody containing a fluorescent group.” In: *Proceedings of the society for experimental biology and medicine* 47.2 (1941). Publisher: SAGE Publications Sage UK: London, England, pp. 200–202. ISSN: 0037-9727.
- [35] Anindita Dasgupta et al. “Direct supercritical angle localization microscopy for nanometer 3D superresolution”. In: *Nature Communications* 12.1 (Feb. 2021), p. 1180. ISSN: 2041-1723. DOI: 10.1038/s41467-021-21333-x. URL: <https://doi.org/10.1038/s41467-021-21333-x>.
- [36] Adrien Descloux et al. “High-speed multiplane structured illumination microscopy of living cells using an image-splitting prism”. In: *Nanophotonics* 9.1 (2020), pp. 143–148. DOI: 10.1515/nanoph-2019-0346. URL: <https://doi.org/10.1515/nanoph-2019-0346>.
- [37] Hans-Ulrich Dodt et al. “Ultramicroscopy: three-dimensional visualization of neuronal networks in the whole mouse brain”. In: *Nature Methods* 4.4 (Apr. 2007), pp. 331–336. ISSN: 1548-7105. DOI: 10.1038/nmeth1036. URL: <https://doi.org/10.1038/nmeth1036>.
- [38] C. Dunsby. “Optically sectioned imaging by oblique plane microscopy”. In: *Optics Express* 16.25 (Dec. 2008), pp. 20306–20316. DOI: 10.1364/OE.16.020306. URL: <http://www.opticsexpress.org/abstract.cfm?URI=oe-16-25-20306>.

- [39] Christoforos Efstathiou and Viji M. Draviam. “Electrically tunable lenses – eliminating mechanical axial movements during high-speed 3D live imaging”. In: *Journal of Cell Science* 134.16 (Aug. 2021), jcs258650. ISSN: 0021-9533. DOI: 10.1242/jcs.258650. URL: <https://doi.org/10.1242/jcs.258650> (visited on 07/14/2022).
- [40] Alexander Egner, Claudia Geisler, and René Sigmund. “STED Nanoscopy”. In: *Nanoscale Photonic Imaging*. Ed. by Tim Salditt, Alexander Egner, and D. Russell Luke. Cham: Springer International Publishing, 2020, pp. 3–34. ISBN: 978-3-030-34413-9. DOI: 10.1007/978-3-030-34413-9\_1. URL: [https://doi.org/10.1007/978-3-030-34413-9\\_1](https://doi.org/10.1007/978-3-030-34413-9_1).
- [41] Ph Ellinger and A Hirt. “Mikroskopische beobachtungen an lebenden organen mit demonstrationen (intravitalmikroskopie)”. In: *Naunyn-Schmiedeberg’s Archives of Pharmacology* 147.1 (1929), pp. 63–63. ISSN: 0028-1298.
- [42] Tanner C. Fadero et al. “LITE microscopy: Tilted light-sheet excitation of model organisms offers high resolution and low photobleaching”. In: *The Journal of Cell Biology* (2018). DOI: 10.1083/jcb.201710087. URL: <http://jcb.rupress.org/content/early/2018/02/27/jcb.201710087.abstract>.
- [43] Florian O. Fahrbach and Alexander Rohrbach. “A line scanned light-sheet microscope with phase shaped self-reconstructing beams”. In: *Optics Express* 18.23 (Nov. 2010), pp. 24229–24244. DOI: 10.1364/OE.18.024229. URL: <http://www.opticsexpress.org/abstract.cfm?URI=oe-18-23-24229>.
- [44] Florian O. Fahrbach and Alexander Rohrbach. “Propagation stability of self-reconstructing Bessel beams enables contrast-enhanced imaging in thick media”. In: *Nature Communications* 3.1 (Jan. 2012), p. 632. ISSN: 2041-1723. DOI: 10.1038/ncomms1646. URL: <https://doi.org/10.1038/ncomms1646>.
- [45] Florian O. Fahrbach et al. “Light-sheet microscopy in thick media using scanned Bessel beams and two-photon fluorescence excitation”. In: *Optics Express* 21.11 (June 2013), pp. 13824–13839. DOI: 10.1364/OE.21.013824. URL: <http://www.opticsexpress.org/abstract.cfm?URI=oe-21-11-13824>.

- [46] Florian O. Fahrbach et al. “Rapid 3D light-sheet microscopy with a tunable lens”. In: *Optics Express* 21.18 (Sept. 2013), pp. 21010–21026. DOI: 10.1364/OE.21.021010. URL: <http://www.opticsexpress.org/abstract.cfm?URI=oe-21-18-21010>.
- [47] Florian O. Fahrbach et al. “Self-reconstructing sectioned Bessel beams offer submicron optical sectioning for large fields of view in light-sheet microscopy”. In: *Optics Express* 21.9 (May 2013), pp. 11425–11440. DOI: 10.1364/OE.21.011425. URL: <http://www.opticsexpress.org/abstract.cfm?URI=oe-21-9-11425>.
- [48] Patricia Fara. “A microscopic reality tale”. In: *Nature* 459.7247 (June 2009), pp. 642–644. ISSN: 1476-4687. DOI: 10.1038/459642a. URL: <https://doi.org/10.1038/459642a>.
- [49] Reto Fiolka. “Resolution upgrades for light-sheet microscopy”. In: *Nature Methods* 16.9 (Sept. 2019), pp. 813–814. ISSN: 1548-7105. DOI: 10.1038/s41592-019-0542-4. URL: <https://doi.org/10.1038/s41592-019-0542-4>.
- [50] Reto Fiolka, Markus Beck, and Andreas Stemmer. “Structured illumination in total internal reflection fluorescence microscopy using a spatial light modulator”. In: *Optics Letters* 33.14 (July 2008), pp. 1629–1631. DOI: 10.1364/OL.33.001629. URL: <http://ol.osa.org/abstract.cfm?URI=ol-33-14-1629>.
- [51] Jonas Fölling et al. “Fluorescence nanoscopy by ground-state depletion and single-molecule return”. In: *Nature Methods* 5.11 (Nov. 2008), pp. 943–945. ISSN: 1548-7105. DOI: 10.1038/nmeth.1257. URL: <https://doi.org/10.1038/nmeth.1257>.
- [52] Cristiane Miranda França et al. “3D-Imaging of Whole Neuronal and Vascular Networks of the Human Dental Pulp via CLARITY and Light Sheet Microscopy”. In: *Scientific Reports* 9.1 (July 2019), p. 10860. ISSN: 2045-2322. DOI: 10.1038/s41598-019-47221-5. URL: <https://doi.org/10.1038/s41598-019-47221-5>.
- [53] WERNER W. FRANKE et al. “Identification and Characterization of Epithelial Cells in Mammalian Tissues by Immunofluorescence Microscopy Using Antibodies to Prekeratin”. In: *Differentiation* 15.1 (Dec. 1979), pp. 7–25. ISSN: 0301-4681. DOI: 10.1111/j.1432-0436.1979.tb01030.x. URL: <http://www.sciencedirect.com/science/article/pii/S0301468111612814>.

- [54] Rainer W. Friedrich, Gilad A. Jacobson, and Peixin Zhu. “Circuit Neuroscience in Zebrafish”. In: *Current Biology* 20.8 (Apr. 2010), R371–R381. ISSN: 0960-9822. DOI: 10.1016/j.cub.2010.02.039. URL: <https://www.sciencedirect.com/science/article/pii/S0960982210002277>.
- [55] Yiin-Kuen Fuh, Jui-Kuan Chen, and Pin-Wen Chen. “Characterization of electrically tunable liquid lens and adaptive optics for aberration correction”. In: *Optik* 126.24 (Dec. 2015), pp. 5456–5459. ISSN: 0030-4026. DOI: 10.1016/j.ijleo.2015.09.105. URL: <https://www.sciencedirect.com/science/article/pii/S0030402615011742>.
- [56] Tsukasa Funane et al. “Selective plane illumination microscopy (SPIM) with time-domain fluorescence lifetime imaging microscopy (FLIM) for volumetric measurement of cleared mouse brain samples”. In: *Review of Scientific Instruments* 89.5 (May 2018). Publisher: American Institute of Physics, p. 053705. ISSN: 0034-6748. DOI: 10.1063/1.5018846. URL: <https://doi.org/10.1063/1.5018846> (visited on 10/26/2021).
- [57] Remi Galland et al. “3D high- and super-resolution imaging using single-objective SPIM”. In: *Nature Methods* 12.7 (July 2015), pp. 641–644. ISSN: 1548-7105. DOI: 10.1038/nmeth.3402. URL: <https://doi.org/10.1038/nmeth.3402>.
- [58] Liang Gao et al. “Noninvasive Imaging beyond the Diffraction Limit of 3D Dynamics in Thickly Fluorescent Specimens”. In: *Cell* 151.6 (Dec. 2012), pp. 1370–1385. ISSN: 0092-8674. DOI: 10.1016/j.cell.2012.10.008. URL: <https://www.sciencedirect.com/science/article/pii/S0092867412012226>.
- [59] Liang Gao et al. “3D live fluorescence imaging of cellular dynamics using Bessel beam plane illumination microscopy”. In: *Nature Protocols* 9.5 (May 2014), pp. 1083–1101. ISSN: 1750-2799. DOI: 10.1038/nprot.2014.087. URL: <https://doi.org/10.1038/nprot.2014.087>.
- [60] J Christof M Gebhardt et al. “Single-molecule imaging of transcription factor binding to DNA in live mammalian cells”. In: *Nature Methods* 10.5 (May 2013), pp. 421–426. ISSN: 1548-7105. DOI: 10.1038/nmeth.2411. URL: <https://doi.org/10.1038/nmeth.2411>.

- [61] Adam K. Glaser, Ye Chen, and Jonathan T. C. Liu. “Fractal propagation method enables realistic optical microscopy simulations in biological tissues”. In: *Optica* 3.8 (Aug. 2016), pp. 861–869. DOI: 10.1364/OPTICA.3.000861. URL: <http://www.osapublishing.org/optica/abstract.cfm?URI=optica-3-8-861>.
- [62] Adam K. Glaser et al. “Light-sheet microscopy for slide-free non-destructive pathology of large clinical specimens”. In: *Nature Biomedical Engineering* 1.7 (June 2017), p. 0084. ISSN: 2157-846X. DOI: 10.1038/s41551-017-0084. URL: <https://doi.org/10.1038/s41551-017-0084>.
- [63] Adam K. Glaser et al. “Multidirectional digital scanned light-sheet microscopy enables uniform fluorescence excitation and contrast-enhanced imaging”. In: *Scientific Reports* 8.1 (Sept. 2018), p. 13878. ISSN: 2045-2322. DOI: 10.1038/s41598-018-32367-5. URL: <https://doi.org/10.1038/s41598-018-32367-5>.
- [64] Joseph W Goodman. *Introduction to Fourier optics*. Roberts and Company Publishers, 2005. ISBN: 0-9747077-2-4.
- [65] Ferdinand Greiss et al. “Single-Molecule Imaging in Living Drosophila Embryos with Reflected Light-Sheet Microscopy”. In: *Biophysical Journal* 110.4 (Feb. 2016), pp. 939–946. ISSN: 0006-3495. DOI: 10.1016/j.bpj.2015.12.035. URL: <https://doi.org/10.1016/j.bpj.2015.12.035> (visited on 01/25/2021).
- [66] Francesco Maria Grimaldi. *Physico-mathesis de lumine, coloribus, et iride, aliisque adnexis libri duo, in quorum primo afferuntur noua experimenta, & rationes ab ijs deductae pro substantialitate luminis. In secundo autem dissoluuntur argumenta in primo adducta, & probabiliter sustineri posse docetur sententia peripatetica de accidentalitate luminis.... Auctore P. Francisco Maria Grimaldo Societatis Iesu. Opus posthumum.* ex typographia haeredis Victorij Benatij, 1963.
- [67] Lusheng Gu et al. “Molecular resolution imaging by repetitive optical selective exposure”. In: *Nature Methods* 16.11 (Nov. 2019), pp. 1114–1118. ISSN: 1548-7105. DOI: 10.1038/s41592-019-0544-2. URL: <https://doi.org/10.1038/s41592-019-0544-2>.
- [68] M. G. L. Gustafsson. “Surpassing the lateral resolution limit by a factor of two using structured illumination microscopy”. In: *Journal of Microscopy* 198.2 (May 2000). Publisher: John Wiley & Sons, Ltd, pp. 82–87. ISSN: 0022-2720. DOI: 10.1046/j.1365-2818.2000.00710.

- x. URL: <https://doi.org/10.1046/j.1365-2818.2000.00710.x> (visited on 02/24/2021).
- [69] Mats G.L. Gustafsson. “Nonlinear structured-illumination microscopy: Wide-field fluorescence imaging with theoretically unlimited resolution”. In: *Proceedings of the National Academy of Sciences of the United States of America* 102.37 (Sept. 2005), p. 13081. DOI: 10.1073/pnas.0406877102. URL: <http://www.pnas.org/content/102/37/13081.abstract>.
- [70] Mats G.L. Gustafsson et al. “Three-Dimensional Resolution Doubling in Wide-Field Fluorescence Microscopy by Structured Illumination”. In: *Biophysical Journal* 94.12 (June 2008), pp. 4957–4970. ISSN: 0006-3495. DOI: 10.1529/biophysj.107.120345. URL: <https://www.sciencedirect.com/science/article/pii/S0006349508703606>.
- [71] Anna-Karin Gustavsson et al. “3D single-molecule super-resolution microscopy with a tilted light sheet”. In: *Nature Communications* 9.1 (Jan. 2018), p. 123. ISSN: 2041-1723. DOI: 10.1038/s41467-017-02563-4. URL: <https://doi.org/10.1038/s41467-017-02563-4>.
- [72] Eugene Hecht. “Optics. Harlow”. In: (2017).
- [73] Mike Heilemann et al. “Subdiffraction-Resolution Fluorescence Imaging with Conventional Fluorescent Probes”. In: *Angewandte Chemie International Edition* 47.33 (Aug. 2008). Publisher: John Wiley & Sons, Ltd, pp. 6172–6176. ISSN: 1433-7851. DOI: 10.1002/anie.200802376. URL: <https://doi.org/10.1002/anie.200802376> (visited on 03/19/2021).
- [74] Oskar Heimstidt. “Das fluoreszenzmikroskop”. In: *Zeitschrift für wissenschaftliche Mikroskopie und mikroskopische Technik* 28 (1911), p. 330. ISSN: 0373-031X.
- [75] Birka Hein, Katrin I. Willig, and Stefan W. Hell. “Stimulated emission depletion (STED) nanoscopy of a fluorescent protein-labeled organelle inside a living cell”. In: *Proceedings of the National Academy of Sciences* 105.38 (Sept. 2008), p. 14271. DOI: 10.1073/pnas.0807705105. URL: <http://www.pnas.org/content/105/38/14271.abstract>.

- [76] Rainer Heintzmann, Thomas M. Jovin, and Christoph Cremer. “Saturated patterned excitation microscopy—a concept for optical resolution improvement”. In: *Journal of the Optical Society of America A* 19.8 (Aug. 2002). Publisher: OSA, pp. 1599–1609. DOI: 10.1364/JOSAA.19.001599. URL: <http://josaa.osa.org/abstract.cfm?URI=josaa-19-8-1599>.
- [77] S. HELL et al. “Aberrations in confocal fluorescence microscopy induced by mismatches in refractive index”. In: *Journal of Microscopy* 169.3 (Mar. 1993). Publisher: John Wiley & Sons, Ltd, pp. 391–405. ISSN: 0022-2720. DOI: 10.1111/j.1365-2818.1993.tb03315.x. URL: <https://doi.org/10.1111/j.1365-2818.1993.tb03315.x> (visited on 05/15/2022).
- [78] Stefan W. Hell and Jan Wichmann. “Breaking the diffraction resolution limit by stimulated emission: stimulated-emission-depletion fluorescence microscopy”. In: *Optics Letters* 19.11 (June 1994). Publisher: OSA, pp. 780–782. DOI: 10.1364/OL.19.000780. URL: <http://ol.osa.org/abstract.cfm?URI=ol-19-11-780>.
- [79] Samuel T. Hess, Thanu P.K. Girirajan, and Michael D. Mason. “Ultra-High Resolution Imaging by Fluorescence Photoactivation Localization Microscopy”. In: *Biophysical Journal* 91.11 (Dec. 2006), pp. 4258–4272. ISSN: 0006-3495. DOI: 10.1529/biophysj.106.091116. URL: <https://www.sciencedirect.com/science/article/pii/S0006349506721403>.
- [80] Maximilian Hoffmann and Benjamin Judkewitz. “Diffractive oblique plane microscopy”. In: *Optica* 6.9 (Sept. 2019), pp. 1166–1170. DOI: 10.1364/OPTICA.6.001166. URL: <http://www.osapublishing.org/optica/abstract.cfm?URI=optica-6-9-1166>.
- [81] Laurent Holtzer, Tobias Meckel, and Thomas Schmidt. “Nanometric three-dimensional tracking of individual quantum dots in cells”. In: *Applied Physics Letters* 90.5 (Jan. 2007). Publisher: American Institute of Physics, p. 053902. ISSN: 0003-6951. DOI: 10.1063/1.2437066. URL: <https://doi.org/10.1063/1.2437066> (visited on 04/07/2021).
- [82] Robert Hooke 1635-1703. *Micrographia, or, Some physiological descriptions of minute bodies made by magnifying glasses: with observations and inquiries thereupon*. London: Printed for James Allestry ... and are to be sold at his shop ..., MDCLXVII [1667], 1667. URL: <https://search.library.wisc.edu/catalog/9910000368102121>.

- [83] Patrick Hoyer et al. “Breaking the diffraction limit of light-sheet fluorescence microscopy by RESOLFT”. In: *Proceedings of the National Academy of Sciences* 113.13 (2016), p. 3442. DOI: 10.1073/pnas.1522292113. URL: <http://www.pnas.org/content/113/13/3442.abstract>.
- [84] Bihe Hu, Daniel Bolus, and J. Quincy Brown. “Improved contrast in inverted selective plane illumination microscopy of thick tissues using confocal detection and structured illumination”. In: *Biomedical Optics Express* 8.12 (Dec. 2017), pp. 5546–5559. DOI: 10.1364/BOE.8.005546. URL: <http://www.osapublishing.org/boe/abstract.cfm?URI=boe-8-12-5546>.
- [85] Bo Huang, Hazen Babcock, and Xiaowei Zhuang. “Breaking the Diffraction Barrier: Super-Resolution Imaging of Cells”. In: *Cell* 143.7 (Dec. 2010). Publisher: Elsevier, pp. 1047–1058. ISSN: 0092-8674. DOI: 10.1016/j.cell.2010.12.002. URL: <https://doi.org/10.1016/j.cell.2010.12.002> (visited on 04/07/2021).
- [86] Bo Huang, Mark Bates, and Xiaowei Zhuang. “Super-resolution fluorescence microscopy”. In: *Annual review of biochemistry* 78 (2009), pp. 993–1016. ISSN: 0066-4154.
- [87] Bo Huang et al. “Three-Dimensional Super-Resolution Imaging by Stochastic Optical Reconstruction Microscopy”. In: *Science* 319.5864 (Feb. 2008), p. 810. DOI: 10.1126/science.1153529. URL: <http://science.sciencemag.org/content/319/5864/810.abstract>.
- [88] Fang Huang et al. “Ultra-High Resolution 3D Imaging of Whole Cells”. In: *Cell* 166.4 (Aug. 2016), pp. 1028–1040. ISSN: 0092-8674. DOI: 10.1016/j.cell.2016.06.016. URL: <https://www.sciencedirect.com/science/article/pii/S0092867416307450>.
- [89] Jan Huisken and Didier Y. R. Stainier. “Even fluorescence excitation by multidirectional selective plane illumination microscopy (mSPIM)”. In: *Optics Letters* 32.17 (Sept. 2007), pp. 2608–2610. DOI: 10.1364/OL.32.002608. URL: <http://ol.osa.org/abstract.cfm?URI=ol-32-17-2608>.
- [90] Jan Huisken and Didier Y. R. Stainier. “Selective plane illumination microscopy techniques in developmental biology”. In: *Development* 136.12 (June 2009), p. 1963. DOI: 10.1242/dev.022426. URL: <http://dev.biologists.org/content/136/12/1963.abstract>.

- [91] Jan Huiskens et al. “Optical Sectioning Deep Inside Live Embryos by Selective Plane Illumination Microscopy”. In: *Science* 305 (Aug. 2004), pp. 1007–1009.
- [92] E.A. INGERMAN et al. “Signal, noise and resolution in linear and nonlinear structured-illumination microscopy”. In: *Journal of Microscopy* 273.1 (Jan. 2019). Publisher: John Wiley & Sons, Ltd, pp. 3–25. ISSN: 0022-2720. DOI: 10.1111/jmi.12753. URL: <https://doi.org/10.1111/jmi.12753> (visited on 05/27/2021).
- [93] J. Fehrenbach, P. Weiss, and C. Lorenzo. “Variational Algorithms to Remove Stationary Noise: Applications to Microscopy Imaging”. In: *IEEE Transactions on Image Processing* 21.10 (Oct. 2012), pp. 4420–4430. ISSN: 1057-7149. DOI: 10.1109/TIP.2012.2206037.
- [94] Joey M. Jabbour et al. “Optical axial scanning in confocal microscopy using an electrically tunable lens”. In: *Biomedical Optics Express* 5.2 (Feb. 2014), pp. 645–652. DOI: 10.1364/BOE.5.000645. URL: <http://www.osapublishing.org/boe/abstract.cfm?URI=boe-5-2-645>.
- [95] Na Ji. “Adaptive optical fluorescence microscopy”. In: *Nature Methods* 14 (Mar. 2017), p. 374. URL: <https://doi.org/10.1038/nmeth.4218>.
- [96] Shu Jia, Joshua C Vaughan, and Xiaowei Zhuang. “Isotropic 3D Super-resolution Imaging with a Self-bending Point Spread Function”. eng. In: *Nature photonics* 8 (2014), pp. 302–306. ISSN: 1749-4885. DOI: 10.1038/nphoton.2014.13. URL: <https://pubmed.ncbi.nlm.nih.gov/25383090>.
- [97] Raphael Jorand et al. “Deep and Clear Optical Imaging of Thick Inhomogeneous Samples”. In: *PLOS ONE* 7.4 (Apr. 2012), e35795. DOI: 10.1371/journal.pone.0035795. URL: <https://doi.org/10.1371/journal.pone.0035795>.
- [98] Aurélie Jost and Rainer Heintzmann. “Superresolution Multidimensional Imaging with Structured Illumination Microscopy”. In: *Annual Review of Materials Research* 43.1 (July 2013), pp. 261–282. ISSN: 1531-7331. DOI: 10.1146/annurev-matsci-071312-121648. URL: <https://doi.org/10.1146/annurev-matsci-071312-121648> (visited on 10/30/2020).

- [99] ZVI KAM et al. “Modelling the application of adaptive optics to wide-field microscope live imaging”. In: *Journal of Microscopy* 226.1 (Apr. 2007). Publisher: John Wiley & Sons, Ltd, pp. 33–42. ISSN: 0022-2720. DOI: 10.1111/j.1365-2818.2007.01751.x. URL: <https://doi.org/10.1111/j.1365-2818.2007.01751.x> (visited on 05/15/2022).
- [100] HP Kao and AS Verkman. “Tracking of single fluorescent particles in three dimensions: use of cylindrical optics to encode particle position”. eng. In: *Biophysical journal* 67.3 (Sept. 1994), pp. 1291–1300. ISSN: 0006-3495. DOI: 10.1016/s0006-3495(94)80601-0. URL: <http://europepmc.org/abstract/MED/7811944>.
- [101] Dejan Karadaglić and Tony Wilson. “Image formation in structured illumination wide-field fluorescence microscopy”. In: *Micron* 39.7 (Oct. 2008), pp. 808–818. ISSN: 0968-4328. DOI: 10.1016/j.micron.2008.01.017. URL: <https://www.sciencedirect.com/science/article/pii/S0968432808000267>.
- [102] Anjan Bhat Kashekodi et al. “Miniature scanning light-sheet illumination implemented in a conventional microscope”. In: *Biomedical Optics Express* 9.9 (Sept. 2018), pp. 4263–4274. DOI: 10.1364/BOE.9.004263. URL: <http://www.osapublishing.org/boe/abstract.cfm?URI=boe-9-9-4263>.
- [103] Anna Kaufmann et al. “Multilayer mounting enables long-term imaging of zebrafish development in a light sheet microscope”. In: *Development* 139.17 (Sept. 2012), p. 3242. DOI: 10.1242/dev.082586. URL: <http://dev.biologists.org/content/139/17/3242.abstract>.
- [104] Philipp J Keller, Misha B Ahrens, and Jeremy Freeman. “Light-sheet imaging for systems neuroscience”. In: *Nature Methods* 12.1 (Jan. 2015), pp. 27–29. ISSN: 1548-7105. DOI: 10.1038/nmeth.3214. URL: <https://doi.org/10.1038/nmeth.3214>.
- [105] Philipp J Keller et al. “Fast, high-contrast imaging of animal development with scanned light sheet-based structured-illumination microscopy”. In: *Nature Methods* 7.8 (Aug. 2010), pp. 637–642. ISSN: 1548-7105. DOI: 10.1038/nmeth.1476. URL: <https://doi.org/10.1038/nmeth.1476>.

- [106] Philipp J Keller et al. “Digital scanned laser light-sheet fluorescence microscopy (DSLM) of zebrafish and *Drosophila* embryonic development”. In: *Cold Spring Harbor Protocols* 2011.10 (2011), pdb–proto65839. ISSN: 1940-3402.
- [107] Philipp J. Keller and Ernst H. K. Stelzer. “Digital Scanned Laser Light Sheet Fluorescence Microscopy”. In: *Cold Spring Harbor Protocols* 2010.5 (May 2010), pdb.top78. DOI: 10.1101/pdb.top78. URL: <http://cshprotocols.cshlp.org/content/2010/5/pdb.top78.abstract>.
- [108] Philipp J. Keller et al. “Reconstruction of Zebrafish Early Embryonic Development by Scanned Light Sheet Microscopy”. In: *Science* 322 (Nov. 2008), pp. 1065–1069.
- [109] Ismail M. Khater, Ivan Robert Nabi, and Ghassan Hamarneh. “A Review of Super-Resolution Single-Molecule Localization Microscopy Cluster Analysis and Quantification Methods”. In: *Patterns* 1.3 (June 2020), p. 100038. ISSN: 2666-3899. DOI: 10.1016/j.patter.2020.100038. URL: <https://www.sciencedirect.com/science/article/pii/S266638992030043X>.
- [110] Jeongmin Kim et al. “Oblique-plane single-molecule localization microscopy for tissues and small intact animals”. In: *Nature Methods* 16.9 (Sept. 2019), pp. 853–857. ISSN: 1548-7105. DOI: 10.1038/s41592-019-0510-z. URL: <https://doi.org/10.1038/s41592-019-0510-z>.
- [111] Thomas A. Klar and Stefan W. Hell. “Subdiffraction resolution in far-field fluorescence microscopy”. In: *Optics Letters* 24.14 (July 1999). Publisher: OSA, pp. 954–956. DOI: 10.1364/OL.24.000954. URL: <http://ol.osa.org/abstract.cfm?URI=ol-24-14-954>.
- [112] Peter Kner et al. “Super-resolution video microscopy of live cells by structured illumination”. In: *Nature Methods* 6.5 (May 2009), pp. 339–342. ISSN: 1548-7105. DOI: 10.1038/nmeth.1324. URL: <https://doi.org/10.1038/nmeth.1324>.
- [113] D. Kromm, T. Thumberger, and J. Wittbrodt. “Chapter 5 - An eye on light-sheet microscopy”. In: *Methods in Cell Biology*. Ed. by H. William Detrich, Monte Westerfield, and Leonard I. Zon. Vol. 133. Academic Press, Jan. 2016, pp. 105–123. ISBN: 0091-679X. DOI: 10.1016/bs.mcb.2016.01.001. URL: <http://www.sciencedirect.com/science/article/pii/S0091679X16000029>.

- [114] Uros Krzic et al. “Multiview light-sheet microscope for rapid in toto imaging”. In: *Nature Methods* 9.7 (July 2012), pp. 730–733. ISSN: 1548-7105. DOI: 10.1038/nmeth.2064. URL: <https://doi.org/10.1038/nmeth.2064>.
- [115] Abhishek Kumar et al. “Dual-view plane illumination microscopy for rapid and spatially isotropic imaging”. In: *Nature Protocols* 9.11 (Nov. 2014), pp. 2555–2573. ISSN: 1750-2799. DOI: 10.1038/nprot.2014.172. URL: <https://doi.org/10.1038/nprot.2014.172>.
- [116] Manish Kumar et al. “Integrated one- and two-photon scanned oblique plane illumination (SOPi) microscopy for rapid volumetric imaging”. In: *Optics Express* 26.10 (May 2018), pp. 13027–13041. DOI: 10.1364/OE.26.013027. URL: <http://www.opticsexpress.org/abstract.cfm?URI=oe-26-10-13027>.
- [117] Lawrence, K et al. “Scene-based Shack-Hartmann wavefront sensor for light-sheet microscopy”. In: *Proceedings of SPIE* 10502 (2018), 105020B–10502–6. URL: <https://doi.org/10.1117/12.2288777>.
- [118] William C. Lemon et al. “Whole-central nervous system functional imaging in larval *Drosophila*”. In: *Nature Communications* 6.1 (Aug. 2015), p. 7924. ISSN: 2041-1723. DOI: 10.1038/ncomms8924. URL: <https://doi.org/10.1038/ncomms8924>.
- [119] Dong Li et al. “Extended-resolution structured illumination imaging of endocytic and cytoskeletal dynamics”. In: *Science* 349.6251 (Aug. 2015), aab3500. DOI: 10.1126/science.aab3500. URL: <http://science.sciencemag.org/content/349/6251/aab3500.abstract>.
- [120] Xiao Liang et al. “Stripe artifact elimination based on nonsubsampling contourlet transform for light sheet fluorescence microscopy”. In: *Journal of Biomedical Optics* 21 (2016), p. 9.
- [121] Bei Liu et al. “VIEW-MOD: a versatile illumination engine with a modular optical design for fluorescence microscopy”. In: *Optics Express* 27.14 (July 2019). Publisher: OSA, pp. 19950–19972. DOI: 10.1364/OE.27.019950. URL: <http://www.osapublishing.org/oe/abstract.cfm?URI=oe-27-14-19950>.
- [122] Sheng Liu et al. “Three-Dimensional Single-Molecule Localization Microscopy in Whole-Cell and Tissue Specimens”. In: *Annual Review of Biomedical Engineering* 22.1 (June 2020), pp. 155–184. ISSN: 1523-9829. DOI: 10.1146/annurev-bioeng-060418-052203. URL: <https://doi.org/10.1146/annurev-bioeng-060418-052203>.

<https://doi.org/10.1146/annurev-bioeng-060418-052203> (visited on 03/27/2021).

- [123] Tsung-Li Liu et al. “Observing the cell in its native state: Imaging subcellular dynamics in multicellular organisms”. In: *Science* 360.6386 (Apr. 2018). DOI: 10.1126/science.aaq1392. URL: <http://science.sciencemag.org/content/360/6386/aaq1392.abstract>.
- [124] Yang Liu et al. “Imaging neural events in zebrafish larvae with linear structured illumination light sheet fluorescence microscopy”. In: *Neurophotonics* 6.1 (Mar. 2019), p. 015009. URL: <https://doi.org/10.1117/1.NPh.6.1.015009>.
- [125] Liu, Y et al. “Sensorless and sensor based adaptive optics for light sheet microscopy”. In: *Proceedings of SPIE* 11248 (Feb. 2020). DOI: 10.1117/12.2543251. URL: <https://doi.org/10.1117/12.2543251>.
- [126] Corinne Lorenzo et al. “Live cell division dynamics monitoring in 3D large spheroid tumor models using light sheet microscopy”. In: *Cell Division* 6.1 (Dec. 2011), p. 22. ISSN: 1747-1028. DOI: 10.1186/1747-1028-6-22. URL: <https://doi.org/10.1186/1747-1028-6-22>.
- [127] Suliana Manley et al. “High-density mapping of single-molecule trajectories with photoactivated localization microscopy”. In: *Nature Methods* 5.2 (Feb. 2008), pp. 155–157. ISSN: 1548-7105. DOI: 10.1038/nmeth.1176. URL: <https://doi.org/10.1038/nmeth.1176>.
- [128] Justin Marshall and Sonke Johnsen. “Fluorescence as a means of colour signal enhancement”. In: *Philosophical Transactions of the Royal Society B: Biological Sciences* 372.1724 (July 2017). Publisher: Royal Society, p. 20160335. DOI: 10.1098/rstb.2016.0335. URL: <https://doi.org/10.1098/rstb.2016.0335> (visited on 09/08/2021).
- [129] Luciano A. Masullo et al. “Enhanced photon collection enables four dimensional fluorescence nanoscopy of living systems”. In: *Nature Communications* 9.1 (Aug. 2018), p. 3281. ISSN: 2041-1723. DOI: 10.1038/s41467-018-05799-w. URL: <https://doi.org/10.1038/s41467-018-05799-w>.

- [130] Ryan McGorty et al. “Open-top selective plane illumination microscope for conventionally mounted specimens”. In: *Optics Express* 23.12 (June 2015), pp. 16142–16153. DOI: 10.1364/OE.23.016142. URL: <http://www.opticsexpress.org/abstract.cfm?URI=oe-23-12-16142>.
- [131] James G. McNally et al. “Three-Dimensional Imaging by Deconvolution Microscopy”. In: *Methods* 19.3 (Nov. 1999), pp. 373–385. ISSN: 1046-2023. DOI: 10.1006/meth.1999.0873. URL: <https://www.sciencedirect.com/science/article/pii/S1046202399908733>.
- [132] Marjolein B. M. Meddens et al. “Single objective light-sheet microscopy for high-speed whole-cell 3D super-resolution”. In: *Biomedical Optics Express* 7.6 (June 2016), pp. 2219–2236. DOI: 10.1364/BOE.7.002219. URL: <http://www.osapublishing.org/boe/abstract.cfm?URI=boe-7-6-2219>.
- [133] Gustavo de Medeiros et al. “Confocal multiview light-sheet microscopy”. In: *Nature Communications* 6.1 (Nov. 2015), p. 8881. ISSN: 2041-1723. DOI: 10.1038/ncomms9881. URL: <https://doi.org/10.1038/ncomms9881>.
- [134] Jerome Mertz and Jinhyun Kim. “Scanning light-sheet microscopy in the whole mouse brain with HiLo background rejection”. In: *Journal of Biomedical Optics* 15.1 (Jan. 2010), p. 016027. ISSN: 1083-3668 1560-2281. DOI: 10.1117/1.3324890. URL: <http://www.ncbi.nlm.nih.gov/pmc/articles/PMC2917465/>.
- [135] Michaela Mickoleit et al. “High-resolution reconstruction of the beating zebrafish heart”. In: *Nature Methods* 11.9 (Sept. 2014), pp. 919–922. ISSN: 1548-7105. DOI: 10.1038/nmeth.3037. URL: <https://doi.org/10.1038/nmeth.3037>.
- [136] Bianca Migliori et al. “Light sheet theta microscopy for rapid high-resolution imaging of large biological samples”. In: *BMC Biology* 16.1 (May 2018), p. 57. ISSN: 1741-7007. DOI: 10.1186/s12915-018-0521-8. URL: <https://doi.org/10.1186/s12915-018-0521-8>.
- [137] M. Caroline Müllenbroich et al. “High-Fidelity Imaging in Brain-Wide Structural Studies Using Light-Sheet Microscopy”. In: *eneuro* 5.6 (Nov. 2018), ENEURO.0124-18.2018. DOI: 10.1523/ENEURO.0124-18.2018. URL: <http://www.eneuro.org/content/5/6/ENEURO.0124-18.2018.abstract>.

- [138] Douglas B. Murphy. *Fundamentals of light microscopy and electronic imaging*. John Wiley & Sons, 2002. ISBN: 0-471-23429-X.
- [139] Yuichiro Nakai et al. “High-speed microscopy with an electrically tunable lens to image the dynamics of in vivo molecular complexes”. In: *Review of Scientific Instruments* 86.1 (Jan. 2015), p. 013707. ISSN: 0034-6748. DOI: 10.1063/1.4905330. URL: <https://doi.org/10.1063/1.4905330> (visited on 02/02/2021).
- [140] Nathan P. Wells et al. “Going beyond 2D: following membrane diffusion and topography in the IgE-Fc[epsilon]RI system using 3-dimensional tracking microscopy”. In: vol. 7185. Feb. 2009. DOI: 10.1117/12.809412. URL: <https://doi.org/10.1117/12.809412>.
- [141] M. A. A. Neil, R. Juškaitis, and T. Wilson. “Method of obtaining optical sectioning by using structured light in a conventional microscope”. In: *Optics Letters* 22.24 (Dec. 1997). Publisher: OSA, pp. 1905–1907. DOI: 10.1364/OL.22.001905. URL: <http://ol.osa.org/abstract.cfm?URI=ol-22-24-1905>.
- [142] Robert J. Noll. “Zernike polynomials and atmospheric turbulence”. In: *Journal of the Optical Society of America* 66.3 (Mar. 1976), pp. 207–211. DOI: 10.1364/JOSA.66.000207. URL: <http://www.osapublishing.org/abstract.cfm?URI=josa-66-3-207>.
- [143] Omar E. Olarte et al. “Decoupled illumination detection in light sheet microscopy for fast volumetric imaging”. In: *Optica* 2.8 (Aug. 2015), pp. 702–705. DOI: 10.1364/OPTICA.2.000702. URL: <http://www.osapublishing.org/optica/abstract.cfm?URI=optica-2-8-702>.
- [144] Omar E. Olarte et al. “Light-sheet microscopy: a tutorial”. In: *Advances in Optics and Photonics* 10.1 (Mar. 2018), pp. III–179. DOI: 10.1364/AOP.10.000111. URL: <http://aop.osa.org/abstract.cfm?URI=aop-10-1-111>.
- [145] Francesco Pampaloni, Nariman Ansari, and Ernst H. K. Stelzer. “High-resolution deep imaging of live cellular spheroids with light-sheet-based fluorescence microscopy”. In: *Cell and Tissue Research* 352.1 (Apr. 2013), pp. 161–177. ISSN: 1432-0878. DOI: 10.1007/s00441-013-1589-7. URL: <https://doi.org/10.1007/s00441-013-1589-7>.

- [146] Thomas Panier et al. “Fast functional imaging of multiple brain regions in intact zebrafish larvae using Selective Plane Illumination Microscopy”. English. In: *Frontiers in Neural Circuits* 7.65 (Apr. 2013). ISSN: 1662-5110. DOI: 10.3389/fncir.2013.00065. URL: <https://www.frontiersin.org/article/10.3389/fncir.2013.00065>.
- [147] Sri Rama Prasanna Pavani et al. “Three-dimensional, single-molecule fluorescence imaging beyond the diffraction limit by using a double-helix point spread function”. In: *Proceedings of the National Academy of Sciences* 106.9 (Mar. 2009), p. 2995. DOI: 10.1073/pnas.0900245106. URL: <http://www.pnas.org/content/106/9/2995.abstract>.
- [148] Peter G. Pitrone et al. “OpenSPIM: an open-access light-sheet microscopy platform”. In: *Nature Methods* 10.7 (2013), pp. 598–599. ISSN: 1548-7091. DOI: 10.1038/nmeth.2507. URL: <http://dx.doi.org/10.1038/nmeth.2507>.
- [149] Thomas A. Planchon et al. “Rapid three-dimensional isotropic imaging of living cells using Bessel beam plane illumination”. In: *Nature Methods* 8 (2011), p. 417. DOI: 10.1038/nmeth.1586. URL: <http://dx.doi.org/10.1038/nmeth.1586>.
- [150] Rory M Power and Jan Huiskens. “A guide to light-sheet fluorescence microscopy for multiscale imaging”. In: *Nature Methods* 14 (Mar. 2017), p. 360. URL: <http://dx.doi.org/10.1038/nmeth.4224>.
- [151] Stephan Preibisch et al. “Software for bead-based registration of selective plane illumination microscopy data”. In: *Nature Methods* 7.6 (June 2010), pp. 418–419. ISSN: 1548-7105. DOI: 10.1038/nmeth0610-418. URL: <https://doi.org/10.1038/nmeth0610-418>.
- [152] Sean Quirin et al. “Calcium imaging of neural circuits with extended depth-of-field light-sheet microscopy”. In: *Optics Letters* 41.5 (Mar. 2016). Publisher: OSA, pp. 855–858. DOI: 10.1364/OL.41.000855. URL: <http://ol.osa.org/abstract.cfm?URI=ol-41-5-855>.
- [153] Rainer Heintzmann and Christoph G. Cremer. “Laterally modulated excitation microscopy: improvement of resolution by using a diffraction grating”. In: *Proceedings of SPIE* 3568 (1999), pp. 3568–12. URL: <https://doi.org/10.1117/12.336833>.

- [154] Lord Rayleigh. “XV. On the theory of optical images, with special reference to the microscope”. In: *The London, Edinburgh, and Dublin Philosophical Magazine and Journal of Science* 42.255 (1896), pp. 167–195. ISSN: 1941-5982.
- [155] E. Hesper Rego and Lin Shao. “Practical Structured Illumination Microscopy”. In: *Advanced Fluorescence Microscopy: Methods and Protocols*. Ed. by Peter J. Verveer. New York, NY: Springer New York, 2015, pp. 175–192. ISBN: 978-1-4939-2080-8. DOI: 10.1007/978-1-4939-2080-8\_10. URL: [https://doi.org/10.1007/978-1-4939-2080-8\\_10](https://doi.org/10.1007/978-1-4939-2080-8_10).
- [156] E. Hesper Rego et al. “Nonlinear structured-illumination microscopy with a photoswitchable protein reveals cellular structures at 50-nm resolution”. In: *Proceedings of the National Academy of Sciences* 109.3 (Jan. 2012), E135. DOI: 10.1073/pnas.1107547108. URL: <http://www.pnas.org/content/109/3/E135.abstract>.
- [157] Pietro Ricci et al. “Fast multi-directional DSLM for confocal detection without striping artifacts”. In: *Biomedical Optics Express* 11.6 (June 2020), pp. 3111–3124. DOI: 10.1364/BOE.390916. URL: <http://www.osapublishing.org/boe/abstract.cfm?URI=boe-11-6-3111>.
- [158] Stephen T. Ross, John R. Allen, and Michael W. Davidson. “Chapter 2 - Practical considerations of objective lenses for application in cell biology”. In: *Methods in Cell Biology*. Ed. by Jennifer C. Waters and Torsten Wittman. Vol. 123. Academic Press, Jan. 2014, pp. 19–34. ISBN: 0091-679X. DOI: 10.1016/B978-0-12-420138-5.00002-1. URL: <https://www.sciencedirect.com/science/article/pii/B9780124201385000021>.
- [159] Loïc A Royer et al. “Adaptive light-sheet microscopy for long-term, high-resolution imaging in living organisms”. In: *Nature Biotechnology* 34 (Oct. 2016), p. 1267. URL: <https://doi.org/10.1038/nbt.3708>.
- [160] Michael J Rust, Mark Bates, and Xiaowei Zhuang. “Sub-diffraction-limit imaging by stochastic optical reconstruction microscopy (STORM)”. In: *Nature Methods* 3.10 (Oct. 2006), pp. 793–796. ISSN: 1548-7105. DOI: 10.1038/nmeth929. URL: <https://doi.org/10.1038/nmeth929>.

- [161] Duncan P. Ryan et al. “Automatic and adaptive heterogeneous refractive index compensation for light-sheet microscopy”. In: *Nature Communications* 8.1 (Sept. 2017), p. 612. ISSN: 2041-1723. DOI: 10.1038/s41467-017-00514-7. URL: <https://doi.org/10.1038/s41467-017-00514-7>.
- [162] L. H. Schaeffer, D. Schuster, and J. Schaffer. “Structured illumination microscopy: artefact analysis and reduction utilizing a parameter optimization approach”. In: *Journal of Microscopy* 216.2 (Oct. 2004), pp. 165–174. ISSN: 0022-2720. DOI: 10.1111/j.0022-2720.2004.01411.x. URL: <https://doi.org/10.1111/j.0022-2720.2004.01411.x> (visited on 11/29/2018).
- [163] Lothar Schermelleh et al. “Subdiffraction Multicolor Imaging of the Nuclear Periphery with 3D Structured Illumination Microscopy”. In: *Science* 320.5881 (June 2008), p. 1332. DOI: 10.1126/science.1156947. URL: <http://science.sciencemag.org/content/320/5881/1332.abstract>.
- [164] Lothar Schermelleh et al. “Super-resolution microscopy demystified”. In: *Nature Cell Biology* 21.1 (Jan. 2019), pp. 72–84. ISSN: 1476-4679. DOI: 10.1038/s41556-018-0251-8. URL: <https://doi.org/10.1038/s41556-018-0251-8>.
- [165] Benjamin Schmid et al. “High-speed panoramic light-sheet microscopy reveals global endodermal cell dynamics”. In: *Nature Communications* 4.1 (July 2013), p. 2207. ISSN: 2041-1723. DOI: 10.1038/ncomms3207. URL: <https://doi.org/10.1038/ncomms3207>.
- [166] Tobias J. Schröter et al. “Scanning thin-sheet laser imaging microscopy (sTSLIM) with structured illumination and HiLo background rejection”. In: *Biomedical Optics Express* 3.1 (Jan. 2012), pp. 170–177. DOI: 10.1364/BOE.3.000170. URL: <http://www.osapublishing.org/boe/abstract.cfm?URI=boe-3-1-170>.
- [167] Lin Shao et al. “Super-resolution 3D microscopy of live whole cells using structured illumination”. In: *Nature Methods* 8.12 (Dec. 2011), pp. 1044–1046. ISSN: 1548-7105. DOI: 10.1038/nmeth.1734. URL: <https://doi.org/10.1038/nmeth.1734>.
- [168] Yoav Shechtman et al. “Multicolour localization microscopy by point-spread-function engineering”. In: *Nature Photonics* 10.9 (Sept. 2016), pp. 590–594. ISSN: 1749-4893. DOI: 10.1038/nphoton.2016.137. URL: <https://doi.org/10.1038/nphoton.2016.137>.

- [169] C.J.R. Sheppard and A. Choudhury. “Image Formation in the Scanning Microscope”. In: *Optica Acta: International Journal of Optics* 24.10 (Oct. 1977), pp. 1051–1073. ISSN: 0030-3909. DOI: 10.1080/713819421. URL: <https://doi.org/10.1080/713819421>.
- [170] Osamu Shimomura, Frank H. Johnson, and Yo Saiga. “Extraction, Purification and Properties of Aequorin, a Bioluminescent Protein from the Luminous Hydromedusan, Aequorea”. In: *Journal of Cellular and Comparative Physiology* 59.3 (June 1962), pp. 223–239. ISSN: 0095-9898. DOI: 10.1002/jcp.1030590302. URL: <https://doi.org/10.1002/jcp.1030590302> (visited on 08/13/2020).
- [171] Gleb Shtengel et al. “Interferometric fluorescent super-resolution microscopy resolves 3D cellular ultrastructure”. In: *Proceedings of the National Academy of Sciences* 106.9 (Mar. 2009), p. 3125. DOI: 10.1073/pnas.0813131106. URL: <http://www.pnas.org/content/106/9/3125.abstract>.
- [172] H. Siedentopf and R. Zsigmondy. “Über Sichtbarmachung und Größenbestimmung ultramikroskopischer Teilchen, mit besonderer Anwendung auf Goldrubingläser”. In: *Annalen der Physik* 315.1 (Jan. 1902), pp. 1–39. ISSN: 0003-3804. DOI: 10.1002/andp.19023150102. URL: <https://doi.org/10.1002/andp.19023150102> (visited on 11/15/2020).
- [173] Ludovico Silvestri et al. “Correlative two-photon and light sheet microscopy”. In: *Advanced Light Microscopy* 66.2 (Mar. 2014), pp. 268–272. ISSN: 1046-2023. DOI: 10.1016/j.ymeth.2013.06.013. URL: <https://www.sciencedirect.com/science/article/pii/S1046202313002144>.
- [174] Liyan Song et al. “Fast structured illumination microscopy using rolling shutter cameras”. In: *Measurement Science and Technology* 27.5 (Apr. 2016), p. 055401. ISSN: 0957-0233. DOI: 10.1088/0957-0233/27/5/055401. URL: <http://dx.doi.org/10.1088/0957-0233/27/5/055401>.
- [175] N. Streibl. “Three-dimensional imaging by a microscope”. In: *Journal of the Optical Society of America A* 2.2 (Feb. 1985), pp. 121–127. DOI: 10.1364/JOSAA.2.000121. URL: <http://josaa.osa.org/abstract.cfm?URI=josaa-2-2-121>.

- [176] James A. Strother. “Reduction of spherical and chromatic aberration in axial-scanning optical systems with tunable lenses”. In: *Biomedical Optics Express* 12.6 (June 2021). Publisher: OSA, pp. 3530–3552. DOI: 10.1364/BOE.422936. URL: <http://www.osapublishing.org/boe/abstract.cfm?URI=boe-12-6-3530>.
- [177] Jim Swoger et al. “Multi-view image fusion improves resolution in three-dimensional microscopy”. In: *Optics Express* 15.13 (June 2007), pp. 8029–8042. DOI: 10.1364/OE.15.008029. URL: <http://www.opticsexpress.org/abstract.cfm?URI=oe-15-13-8029>.
- [178] Jialei Tang, Jinhan Ren, and Kyu Young Han. “Fluorescence imaging with tailored light”. In: *Nanophotonics* 8.12 (2019), pp. 2111–2128. DOI: 10.1515/nanoph-2019-0227. URL: <https://doi.org/10.1515/nanoph-2019-0227>.
- [179] Jonathan M. Taylor et al. “Author Correction: Adaptive prospective optical gating enables day-long 3D time-lapse imaging of the beating embryonic zebrafish heart”. In: *Nature Communications* 11.1 (July 2020), p. 3648. ISSN: 2041-1723. DOI: 10.1038/s41467-020-17483-z. URL: <https://doi.org/10.1038/s41467-020-17483-z>.
- [180] Michael A. Taylor et al. “Diffuse light-sheet microscopy for stripe-free calcium imaging of neural populations”. In: *Journal of Biophotonics* 0.0 (June 2018), e201800088. ISSN: 1864-063X. DOI: 10.1002/jbio.201800088. URL: <https://doi.org/10.1002/jbio.201800088> (visited on 10/13/2018).
- [181] Kayvan F Tehrani et al. “Adaptive optics stochastic optical reconstruction microscopy (AO-STORM) using a genetic algorithm”. In: *Optics Express* 23.10 (May 2015), pp. 13677–13692. DOI: 10.1364/OE.23.013677. URL: <http://www.opticsexpress.org/abstract.cfm?URI=oe-23-10-13677>.
- [182] Kayvan F. Tehrani et al. “Adaptive optics stochastic optical reconstruction microscopy (AO-STORM) by particle swarm optimization”. In: *Biomedical Optics Express* 8.11 (Nov. 2017), pp. 5087–5097. DOI: 10.1364/BOE.8.005087. URL: <http://www.osapublishing.org/boe/abstract.cfm?URI=boe-8-11-5087>.

- [183] Benjamin Thomas, Michelle Momany, and Peter Kner. “Optical sectioning structured illumination microscopy with enhanced sensitivity”. In: *Journal of Optics* 15.9 (2013), p. 094004. ISSN: 2040-8986. URL: <http://stacks.iop.org/2040-8986/15/i=9/a=094004>.
- [184] Thomas, B et al. “Enhanced resolution through thick tissue with structured illumination and adaptive optics”. In: *Journal of Biomedical Optics* 20 (2015), pp. 026006–20–8. URL: <https://doi.org/10.1117/1.JBO.20.2.026006>.
- [185] Kurt Thorn. “A quick guide to light microscopy in cell biology”. eng. In: *Molecular biology of the cell* 27.2 (Jan. 2016), pp. 219–222. ISSN: 1939-4586. DOI: 10.1091/mbc.E15-02-0088. URL: <https://pubmed.ncbi.nlm.nih.gov/26768859>.
- [186] Makio Tokunaga, Naoko Imamoto, and Kumiko Sakata-Sogawa. “Highly inclined thin illumination enables clear single-molecule imaging in cells”. In: *Nature Methods* 5.2 (Feb. 2008), pp. 159–161. ISSN: 1548-7105. DOI: 10.1038/nmeth1171. URL: <https://doi.org/10.1038/nmeth1171>.
- [187] Raju Tomer et al. “Quantitative high-speed imaging of entire developing embryos with simultaneous multiview light-sheet microscopy”. In: *Nature Methods* 9.7 (July 2012), pp. 755–763. ISSN: 1548-7105. DOI: 10.1038/nmeth.2062. URL: <https://doi.org/10.1038/nmeth.2062>.
- [188] Raju Tomer et al. “SPED Light Sheet Microscopy: Fast Mapping of Biological System Structure and Function”. In: *Cell* 163.7 (Dec. 2015), pp. 1796–1806. ISSN: 0092-8674. DOI: 10.1016/j.cell.2015.11.061. URL: <http://www.sciencedirect.com/science/article/pii/S0092867415016232>.
- [189] Erdal Toprak et al. “Three-Dimensional Particle Tracking via Bifocal Imaging”. In: *Nano Letters* 7.7 (July 2007). Publisher: American Chemical Society, pp. 2043–2045. ISSN: 1530-6984. DOI: 10.1021/nl0709120. URL: <https://doi.org/10.1021/nl0709120>.
- [190] Madhu Veetikazhy et al. “Multi-photon attenuation-compensated light-sheet fluorescence microscopy”. In: *Scientific Reports* 10.1 (May 2020), p. 8090. ISSN: 2045-2322. DOI: 10.1038/s41598-020-64891-8. URL: <https://doi.org/10.1038/s41598-020-64891-8>.

- [191] Mary Grace M. Velasco et al. “3D super-resolution deep-tissue imaging in living mice”. In: *Optica* 8.4 (Apr. 2021). Publisher: OSA, pp. 442–450. DOI: 10.1364/OPTICA.416841. URL: <http://www.osapublishing.org/optica/abstract.cfm?URI=optica-8-4-442>.
- [192] Peter J Verveer et al. “High-resolution three-dimensional imaging of large specimens with light sheet-based microscopy”. In: *Nature Methods* 4.4 (Apr. 2007), pp. 311–313. ISSN: 1548-7105. DOI: 10.1038/nmeth1017. URL: <https://doi.org/10.1038/nmeth1017>.
- [193] Tom Vettenburg et al. “Light-sheet microscopy using an Airy beam”. In: *Nature Methods* 11.5 (May 2014), pp. 541–544. ISSN: 1548-7105. DOI: 10.1038/nmeth.2922. URL: <https://doi.org/10.1038/nmeth.2922>.
- [194] A. H. VOIE, D. H. BURNS, and F. A. SPELMAN. “Orthogonal-plane fluorescence optical sectioning: Three-dimensional imaging of macroscopic biological specimens”. In: *Journal of Microscopy* 170.3 (June 1993), pp. 229–236. ISSN: 0022-2720. DOI: 10.1111/j.1365-2818.1993.tb03346.x. URL: <https://doi.org/10.1111/j.1365-2818.1993.tb03346.x> (visited on 11/16/2020).
- [195] Fabian F. Voigt et al. “The mesoSPIM initiative: open-source light-sheet microscopes for imaging cleared tissue”. In: *Nature Methods* 16.11 (Nov. 2019), pp. 1105–1108. ISSN: 1548-7105. DOI: 10.1038/s41592-019-0554-0. URL: <https://doi.org/10.1038/s41592-019-0554-0>.
- [196] Felix Wäldchen et al. “Whole-cell imaging of plasma membrane receptors by 3D lattice light-sheet dSTORM”. In: *Nature Communications* 11.1 (Feb. 2020), p. 887. ISSN: 2041-1723. DOI: 10.1038/s41467-020-14731-0. URL: <https://doi.org/10.1038/s41467-020-14731-0>.
- [197] Depeng Wang et al. “Hybrid light-sheet and light-field microscope for high resolution and large volume neuroimaging”. In: *Biomedical Optics Express* 10.12 (Dec. 2019). Publisher: OSA, pp. 6595–6610. DOI: 10.1364/BOE.10.006595. URL: <http://www.osapublishing.org/boe/abstract.cfm?URI=boe-10-12-6595>.
- [198] Kai Wang et al. “Rapid adaptive optical recovery of optimal resolution over large volumes”. In: *Nature Methods* 11 (Apr. 2014), p. 625. URL: <https://doi.org/10.1038/nmeth.2925>.

- [199] Michael Weber, Michaela Mickoleit, and Jan Huisken. “Multilayer mounting for long-term light sheet microscopy of zebrafish”. In: *Journal of visualized experiments: JoVE* 84 (Feb. 2014), e51119–e51119. ISSN: 1940-087X. DOI: 10.3791/51119. URL: <https://www.ncbi.nlm.nih.gov/pubmed/24637614>.
- [200] Dean Wilding et al. “Adaptive illumination based on direct wavefront sensing in a light-sheet fluorescence microscope”. In: *Optics Express* 24.22 (Oct. 2016), pp. 24896–24906. DOI: 10.1364/OE.24.024896. URL: <http://www.opticsexpress.org/abstract.cfm?URI=oe-24-22-24896>.
- [201] Yicong Wu and Hari Shroff. “Faster, sharper, and deeper: structured illumination microscopy for biological imaging”. In: *Nature Methods* 15.12 (Dec. 2018), pp. 1011–1019. ISSN: 1548-7105. DOI: 10.1038/s41592-018-0211-z. URL: <https://doi.org/10.1038/s41592-018-0211-z>.
- [202] Yicong Wu et al. “Inverted selective plane illumination microscopy (<em>SPIM</em>) enables coupled cell identity lineaging and neurodevelopmental imaging in <em>Caenorhabditis elegans</em>”. In: *Proceedings of the National Academy of Sciences* 108.43 (Oct. 2011), p. 17708. DOI: 10.1073/pnas.1108494108. URL: <http://www.pnas.org/content/108/43/17708.abstract>.
- [203] Yicong Wu et al. “Spatially isotropic four-dimensional imaging with dual-view plane illumination microscopy”. In: *Nature Biotechnology* 31.11 (Nov. 2013), pp. 1032–1038. ISSN: 1546-1696. DOI: 10.1038/nbt.2713. URL: <https://doi.org/10.1038/nbt.2713>.
- [204] Xiao Liang et al. “Stripe artifact elimination based on nonsubsampling contourlet transform for light sheet fluorescence microscopy”. In: *Journal of Biomedical Optics* 21 (2016), pp. 106005–21–9. URL: <https://doi.org/10.1117/1.JBO.21.10.106005>.
- [205] Masahito Yamanaka, Nicholas I. Smith, and Katsumasa Fujita. “Introduction to super-resolution microscopy”. In: *Microscopy* 63.3 (June 2014), pp. 177–192. ISSN: 2050-5698. DOI: 10.1093/jmicro/dfu007. URL: <https://doi.org/10.1093/jmicro/dfu007> (visited on 02/24/2021).
- [206] Bin Yang et al. “Epi-illumination SPIM for volumetric imaging with high spatial-temporal resolution”. In: *Nature Methods* 16.6 (June 2019), pp. 501–504. ISSN: 1548-7105. DOI: 10.1038/s41592-019-0401-3. URL: <https://doi.org/10.1038/s41592-019-0401-3>.

- [207] Zhe Yang et al. “Dual-slit confocal light sheet microscopy for in vivo whole-brain imaging of zebrafish”. In: *Biomedical Optics Express* 6.5 (May 2015), pp. 1797–1811. DOI: 10.1364/BOE.6.001797. URL: <http://www.osapublishing.org/boe/abstract.cfm?URI=boe-6-5-1797>.
- [208] Zhengyi Yang et al. “A compact Airy beam light sheet microscope with a tilted cylindrical lens”. In: *Biomedical Optics Express* 5.10 (Oct. 2014), pp. 3434–3442. DOI: 10.1364/BOE.5.003434. URL: <http://www.osapublishing.org/boe/abstract.cfm?URI=boe-5-10-3434>.
- [209] Elisa Zagato et al. “Microfabricated devices for single objective single plane illumination microscopy (SoSPIM)”. In: *Optics Express* 25.3 (Feb. 2017), pp. 1732–1745. DOI: 10.1364/OE.25.001732. URL: <http://www.opticsexpress.org/abstract.cfm?URI=oe-25-3-1732>.
- [210] ZEISS Microscopy Online Campus | *Introduction to Superresolution Microscopy*. URL: <http://zeiss-campus.magnet.fsu.edu/articles/superresolution/introduction.html> (visited on 09/10/2021).
- [211] Ziqing W. Zhao et al. “Spatial organization of RNA polymerase II inside a mammalian cell nucleus revealed by reflected light-sheet super-resolution microscopy”. In: *Proceedings of the National Academy of Sciences* 111.2 (Jan. 2014), p. 681. DOI: 10.1073/pnas.1318496111. URL: <http://www.pnas.org/content/111/2/681.abstract>.
- [212] Chao Zuo et al. “High-speed transport-of-intensity phase microscopy with an electrically tunable lens”. In: *Optics Express* 21.20 (Oct. 2013), pp. 24060–24075. DOI: 10.1364/OE.21.024060. URL: <http://www.opticsexpress.org/abstract.cfm?URI=oe-21-20-24060>.

# APPENDIX A

## A.1 LLSM illumination pattern simulation

```
1  """
2  Created on Sun Aug  2 15:20:04 2020
3
4  @author: Yang Liu
5  """
6
7
8  import numpy as np
9  from numpy import matlib as mb
10 fft2 = np.fft.fft2
11 ifft2 = np.fft.ifft2
12 fftn = np.fft.fftn
13 ifftn = np.fft.ifftn
14 fftshift = np.fft.fftshift
15 ifftshift = np.fft.ifftshift
16 import tiff file as tf
17 from scipy.ndimage import gaussian_filter
18 from PIL import Image
19 from scipy.special import jn
20
21
22
23
24
25
26
27 class generate(object):
28
29     def __init__(self):
30         self.na1 = 0.07
```

```

31     self.na2 = 0.128
32     self.na_p = 0.4
33     self.wl = 0.488
34     self.nx = 512
35     self.dx = self.wl/self.na2/2/8
36     self.dp = 1/(self.nx*self.dx)
37     self.n2 = 1.333
38     self.p = self.dp*np.arange((-self.nx/2),(self.
nx/2))
39     p = self.p
40     self.kx,self.ky = np.meshgrid(p,p,sparse=True)
41     self.rho = np.sqrt(self.kx**2+self.ky**2)
42     self.msk = self.rho<=self.na2/self.wl
43     self.bpp2 = np.array(self.msk).astype('int64')
44     self.bpp1 = np.array(self.rho<=self.na1/self.wl
).astype('int64')
45     self.move = int(self.na_p/self.wl/self.dp)
46     self.move1 = int(self.move*np.cos(np.pi/3))+1
47     self.move2 = int(self.move*np.sin(np.pi/3))+1
48     self.annulus = self.bpp2-self.bpp1
49     self.dz = .100
50     self.zr = 25.5 # in microns
51     self.Np = 50 # number of particles
52     self.imgf = np.zeros((self.nx,self.nx), dtype=
np.float32)
53     lim1 = -self.zr/2
54     lim2 = self.zr/2
55     self.nz = int((lim2-lim1)/self.dz+1)
56     # self.Zreleigh =
57     # np.pad use wrap to expand the image
58
59     def getSLMimg(self, img, alpha, num_phase=5, pattern_px
=20):
60         nx = 4096
61         ny = 4096
62         slmwidth = 2048
63         slmheight = 1536
64         pdx = int((nx-self.nx)*.5)
65         pdy = int((ny-self.nx)*.5)
66         I = np.pad(img,((pdy,pdy),(pdx,pdx)), 'wrap')
67         I = I/np.max(I)*255
68         slm_h_start = int((nx-slmwidth)*.5)
69         slm_v_start = int((ny-slmheight)*.5)
70         move = int(pattern_px/num_phase)
71         for i in range(num_phase):
72             slm_h_start=slm_h_start+i*move

```

```

73         temp = I[slm_v_start:slm_v_start+slmheight,
slm_h_start:slm_h_start+slmwidth]
74         temp[temp<=np.max(I)*alpha]=0
75         temp[temp!=0]=255
76         temp = temp.astype(np.uint8)
77         final = Image.fromarray(temp)
78         final.save('converted_pattern.bmp')
79         im = Image.open('converted_pattern.bmp')
80         im=im.convert('1')
81         im.save(f'phase{i}_pattern_px{pattern_px}
_1bitimg.bmp')
82         im.close()
83         tf.imshow(temp)
84         #binary
85         return temp
86     # def getfivephase(self,I):
87
88
89     def convertimg(self,filepath):
90         im = Image.open(filepath)
91         im=im.convert('1')
92         im.save('1bitimg_converted.bmp')
93         im.close()
94
95
96
97     def getSquareLatticePixel(self, Npix = 10, phase =
0):
98         ''' repeats pattern every Npix
99         phase is in pixels '''
100         k = 2*np.pi/self.wl
101         x = np.linspace(-self.nx*self.dx*.5,self.nx*
self.dx*.5,self.nx) #FOV_x in micron
102         y = np.linspace(-self.nx*self.dx*.5,self.nx*
self.dx*.5,self.nx) #FOV_y
103         [xx,yy] = np.meshgrid(x,y)
104         xxc = phase*self.dx
105         rho = np.sqrt((xx-xxc)**2+yy**2)
106         ## light sheet thickness
107         fwhm = 5.0
108         ls_sigma = fwhm/(2*np.log(2))
109         ## bessell function maxima 1st: 7.0156, 2nd:
13.3237
110         xmax = 7.0156
111         na_p = xmax/(k*Npix*self.dx)
112         bconf = self.dx*xmax# bessell confinement factor
113         print(na_p)

```

```

114     e1 = jn(0,k*rho*na_p)*np.exp(-0.5*(rho/bconf)
**2)
115     tf.imshow(e1)
116     spacing = Npix*self.dx
117     ## create lattice
118     st_x= int((self.nx)*.5)
119     a1 = np.array([0, Npix])
120     a2 = np.array([Npix, 0])
121     elatt = np.zeros([self.nx,self.nx])
122     for m in np.arange(-8,8):
123         for n in np.arange(-8,8):
124             b = m*a1 + n*a2
125             C = np.roll(e1,b[0],axis=0)
126             C = np.roll(C,b[1],axis=1)
127             elatt = elatt + C
128     # pattern
129     I = np.abs(elatt)**2
130     I = I/np.max(I)
131     tf.imshow(I)
132     # back pupil
133     ls = np.exp(-0.5*(yy/ls_sigma)**2)
134     # tf.imshow((np.abs(ls*elatt))**2)
135     bpp = np.abs(fftshift(fft2(ls*elatt)))**2
136     tf.imshow(bpp)
137     elatt = elatt[st_x-Npix:st_x+Npix,st_x-Npix:
st_x+Npix]
138     I = np.abs(elatt)**2
139     I = I/np.max(I)
140     return I
141
142     def getSquareLatticePixel2(self, Npix = 10, phase =
0):
143         ''' repeats pattern every Npix
144             phase is in pixels '''
145         k = 2*np.pi/self.wl
146         x = np.linspace(-self.nx*self.dx*.5,self.nx*
self.dx*.5,self.nx) #FOV_x in micron
147         y = np.linspace(-self.nx*self.dx*.5,self.nx*
self.dx*.5,self.nx) #FOV_y
148         [xx,yy] = np.meshgrid(x,y)
149         xxc = phase*self.dx
150         rho = np.sqrt((xx-xxc)**2+yy**2)
151         ## light sheet thickness
152         fwhm = 5.0
153         ls_sigma = fwhm/(2*np.log(2))
154         ## bessell function maxima 1st: 7.0156, 2nd:
13.3237

```

```

155     xmax = 7.0156
156     na_p = xmax/(k*Npix*self.dx)
157     bconf = self.dx*xmax# bessel confinement factor
158     print(na_p)
159     e1 = jn(0,k*rho*na_p)*np.exp(-0.5*(rho/bconf)
**2)
160     tf.imshow(e1)
161     spacing = Npix*self.dx
162     ## create lattice
163     st_x= int((self.nx)*.5)
164     a1 = np.array([0, Npix])
165     a2 = np.array([Npix, 0])
166     elatt = np.zeros([self.nx,self.nx])
167     for m in np.arange(-8,8):
168         for n in np.arange(-8,8):
169             b = m*a1 + n*a2
170             C = np.roll(e1,b[0],axis=0)
171             C = np.roll(C,b[1],axis=1)
172             elatt = elatt + C
173     # pattern
174     I = np.abs(elatt)**2
175     I = I/np.max(I)
176     tf.imshow(I)
177     # back pupil
178     ls = np.exp(-0.5*(yy/ls_sigma)**2)
179     temp = I
180     temp[temp<=np.max(I)*alpha]=0
181     temp[temp!=0]=1
182     # tf.imshow((np.abs(ls*elatt))**2)
183     bpp = np.abs(fftshift(fft2(ls*temp)))**2
184     tf.imshow(bpp)
185     elatt = elatt[st_x-Npix:st_x+Npix,st_x-Npix:
st_x+Npix]
186     I = np.abs(elatt)**2
187     I = I/np.max(I)
188     return I
189
190
191
192
193     def gethexagonallattice(self, degree=None, a=1.0):
194         if degree ==None:
195             degree = np.deg2rad(120)
196         else:
197             degree = np.deg2rad(degree)
198         k = 2*np.pi/self.wl

```

```

199     x = np.linspace(-self.nx*self.dx*.5,self.nx*
self.dx*.5,self.nx) #FOV_x in micron
200     y = np.linspace(-self.nx*self.dx*.5,self.nx*
self.dx*.5,self.nx) #FOV_y
201     [xx,yy] = np.meshgrid(x,y)
202     rho = np.sqrt(xx**2+yy**2)
203     e1 = jn(0,k*rho*self.na_p)
204     # tf.imshow(e1)
205     sp = self.wl/self.na_p
206     ns =(sp/self.dx)
207     print(ns)
208     step = int(np.floor(ns))
209     a1 = np.array([0.0,sp*2.0*a])
210     a2 = np.array([a*2*sp*np.sin(degree),a*2.0*sp*
np.cos(degree)])
211     step_y=int(np.ceil(step*2*np.tan(0.5*(np.
deg2rad(180)-degree))))
212     # print(step_y)
213     elatt = np.zeros([self.nx,self.nx])
214     fov_radius = self.nx*self.dx*.1
215     st_x = int((self.nx)*.5)
216     st_y = int((self.nx)*.5)
217     for m in np.arange(-fov_radius,fov_radius):
218         for n in np.arange(-fov_radius,fov_radius):
219             b = np.floor((m*a1+n*a2)/self.dx)
220             b = b.astype(int)
221             # print(b)
222             C = np.roll(e1,b[0],axis=0)
223             C = np.roll(C,b[1],axis=1)
224             elatt = elatt + C
225     elatt = elatt[st_y-step_y:st_y+step_y,st_x-step
:st_x+step]
226     I = np.abs(elatt)**2
227     I = I/np.max(I)
228     # tf.imshow(I)
229     # tf.imshow(elatt)
230     return I
231
232
233
234
235
236     def getsquarelattice(self,a=1):
237         k = 2*np.pi/self.wl
238         x = np.linspace(-self.nx*self.dx*.5,self.nx*
self.dx*.5,self.nx) #FOV_x in micron

```

```

239     y = np.linspace(-self.nx*self.dx*.5,self.nx*
self.dx*.5,self.nx) #FOV_y
240     [xx,yy] = np.meshgrid(x,y)
241     rho = np.sqrt(xx**2+yy**2)
242     e1 = jn(0,k*rho*self.na_p)
243     sp = self.wl/self.na_p
244     print(sp)
245     ns =(sp/self.dx)
246     step = int(np.floor(ns))
247     move= int(np.ceil(step*np.tan(np.deg2rad(45))))
248     a1 = np.array([0.0,a*sp*1.0])
249     a2 = np.array([a*sp*1.0,0.0])
250     elatt = np.zeros([self.nx,self.nx])
251     dx = self.wl/self.na_p/2/8
252     fov_radius = self.nx*dx*.25
253     st_x= int((self.nx)*.5)
254     # width = int(self.nx*.25)
255     for m in np.arange(-fov_radius,fov_radius+1):
256         for n in np.arange(-fov_radius,fov_radius
+1):
257             b = np.floor((m*a1+n*a2)/self.dx)
258             b = b.astype(int)
259             # print(b)
260             C = np.roll(e1,b[0],axis=0)
261             C = np.roll(C,b[1],axis=1)
262             elatt = elatt + C
263         elatt = elatt[st_x-move:st_x+move,st_x-move:
st_x+move]
264         I = np.abs(elatt)**2
265         I = I/np.max(I)
266         # tf.imshow(I)
267         # tf.imshow(elatt)
268         return I
269
270
271
272
273
274
275
276     def threebeamlatticeangle1(self):
277         '''get the central diff order'''
278         self.getdot(int(0))
279         part1 = self.dot
280         '''get the right difforder, 2 is the diff
length'''
281         part4 = np.roll(part1,self.move1,axis=1)

```

```

282     part4 = np.roll(part4,self.move2,axis=0)
283     '''get the left difforder, 2 is the diff length
    ,,,
284     part5 = np.roll(part1,self.move1,axis=1)
285     part5 = np.roll(part5,-self.move2,axis=0)
286     part3 = np.roll(part1,-self.move,axis=1)
287     temp = part3+part4+part5
288     self.bpp = self.annulus*temp
289     E = ifftshift(iff2(self.bpp))
290     I1 =np.abs(E)**2
291     #     I1 = np.real(E*np.conj(E))
292     I1 = I1/np.max(I1)
293     tf.imshow(self.bpp)
294     tf.imshow(I1)
295     return I1
296
297
298     def getpixpattern(self):
299         img = np.zeros((self.nx,self.nx))
300         patternlength =4
301         delta = patternlength*0.5
302         pos = np.arange(0,self.nx,4)
303         for n in range(delta):
304             img[:,pos+n]=1
305
306         return img
307
308
309     def twobeamsinpattern(self):
310         self.getdot(int(0))
311         temp = self.dot
312         part1 = np.roll(temp,self.move,axis=1)
313         part2 = np.roll(temp,-self.move,axis=1)
314         final = part1+part2
315         self.bpp = self.annulus*final
316         E = ifftshift(iff2(self.bpp))
317         I1 =np.abs(E)**2
318         I1 = I1/np.max(I1)
319         tf.imshow(self.bpp)
320         tf.imshow(I1)
321         return I1
322
323
324
325
326
327

```

```

328     def fourbeam3dsimlattice(self):
329         self.getVline(0,1)
330         temp = self.Vline
331         part1 = np.roll(temp,self.move,axis=1)
332         part2 = np.roll(temp,-self.move,axis=1)
333         part3 = np.roll(temp,self.move+1,axis=0)
334         part4 = np.roll(temp,-self.move,axis=0)
335         final = part1+part2+part3+part4
336         self.bpp = self.annulus*final
337         E = ifftshift(ifft2(self.bpp))
338         I1 =np.abs(E)**2
339         tf.imshow(self.bpp)
340         tf.imshow(I1)
341         return I1
342
343
344
345
346     def getVline(self,position,length=None):
347         '''max length for 256 is 255'''
348         self.Vline = np.zeros_like(self.msk)
349         if length != None:
350             d = length/2
351             self.Vline[int(self.nx/2-d):int(self.nx/2+d
352 ),int(self.nx/2)]=1.0
353         else:
354             self.Vline[:,int(self.nx/2)]=1.0
355         self.Vline = np.array(self.Vline).astype('
float32')
356         self.Vline=np.roll(self.Vline,position,axis =
357 1)
358
359     def getdot(self,position):
360         self.dot = np.zeros_like(self.msk)
361         self.dot[int(self.nx/2)-1,int(self.nx/2)-1]=1.0
362
363     def getHline(self,position,length=None):
364         self.Hline = np.zeros_like(self.msk)
365         if length != None:
366             d = length/2
367             self.Hline[int(self.nx/2),int(self.nx/2-d):
368 int(self.nx/2+d)]=1.0
369         else:
370             self.Hline[int(self.nx/2),:]=1.0
371         self.Hline = np.array(self.Hline).astype('
float32')
372         if position!=None:

```

```

370         self.Hline=np.roll(self.Hline,position,axis
=0)
371     else:
372         self.Hline=np.roll(self.Hline,self.move,
axis=0)
373
374
375
376 def main():
377     gen = generate()
378     # I = gen.gethexagonallattice()
379     # I = gen.getsquarelattice(a=2)
380     I=gen.getSquareLatticePixel(Npix=10)
381     final = gen.getSLMimg(I,0.35,pattern_px=10)
382     img =
383
384
385
386
387 if __name__ == '__main__':
388     main()
389
390
391
392
393 #
394 #     self.wl = 0.488 # wavelength
395 #     self.k = 2*pi/self.wl
396 #     self.mag = 66.67 # mag of slm to imaging plane
397 #     self.n2 = 1.333 # Immersion medium
398 #     self.numpix = [int(self.SLM_x/2), int(self.
SLM_y/2)]
399 #     pixsize = np.array([512,512]) / (self.wl /
1.33)
400 #     x = pixsize[0] * np.arange(0, self.numpix[0] +
1)
401 #     y = pixsize[1] * np.arange(0, self.numpix[1] +
1)
402 #     [X, Y] = np.meshgrid(x, y)
403 #     NA_outer=0.8
404 #     NA_inner=0.7
405 #     NA_ideal = 0.75
406 #     kideal = 2 * np.pi * (NA_ideal / self.n2)
407 #     kxmax = 2 * np.pi * (NA_outer / self.n2)
408 #     kxmin = 2 * np.pi * (NA_inner / self.n2)
409 #     kxdiff = kxmax - kxmin

```

```

410 #         # approximate half width of the function
        limiting
411 #         # the extent of the bound lattice, in media
        wavelengths
412 #         lattice_full_width = np.pi / kxdiff
413 #         print('xwidth')
414 #         print(lattice_full_width)
415 #         kzmax = 2 * np.pi * np.sqrt(1 - (NA_inner/self
        .n2)**2)
416 #         kzmin = 2 * np.pi * np.sqrt(1 - (NA_outer/self
        .n2)**2)
417 #         kzdiff = kzmax - kzmin
418 #         yextent = np.pi / kzdiff # approximate extent
        of the lattice in y, in media wavelengths
419 #         print('fov length')
420 #         print(yextent)
421 #         R = np.sqrt(X*X + Y*Y)
422 #         MaxRad = NA_outer / self.n2 # maximum annulus
        diameter
423 #         MinRad = NA_inner / self.n2 # minimum annulus
        diameter
424 #         self.AnnularFilter = (R <= MaxRad) & (R >=
        MinRad)
425 #         self.dp_x = 1/(self.numpix*pixsize[0]) #
        sampling frequency
426 #         self.dp_y = 1/(self.numpix*pixsize[1])
427 #         self.position_x = (NA_outer/self.wl)/self.dp_x
        # radius
428 #         self.position_y = (NA_outer/self.wl)/self.dp_y
        # radius
429 ##         self.radius = (self.na/self.wl)/self.dp #
        radius

```

## A.2 Mask at conjugate back pupil plane

```

1  """
2  Created on Sat Apr 9 17:25:47 2022
3
4  @author: Yang Liu
5
6  """
7
8  import numpy as np
9
10
11 def main():
12     wl = 0.488

```

```

13 patternpx = 9 # [10:20]
14 slmpxsize = 8.2
15 Na_obj = 0.8
16 mag = 16
17 f_tl = 200
18 f_obj = f_tl/mag
19 D_bpp = 2*f_obj*Na_obj
20 theta = wl/patternpx/slmpxsize
21 D = theta*2*200*100/150*75/30*200/80
22 print(D)
23 Na = D/D_bpp*Na_obj
24 print(Na)
25 thickness = np.arange(1, 5)
26 NAeff = wl/2/thickness
27 NA = np.round(np.sqrt(NAeff**2+Na**2),3) #mask
outer
28 na = np.round(Na*2-NA,3)
29 NA[NA>Na_obj]=Na_obj
30 D_outer = np.round(NA/.8*20*80/200*30/75*150/100,3)
31 D_inner = np.round(na/.8*20*80/200*30/75*150/100,3)
32 NA_neweff = np.sqrt(NA**2-((NA+na)*0.5)**2)
33 thickness= wl/2/NA_neweff
34 print('Light Sheet Thickness')
35 print(np.round(thickness,3))
36 print('Outer NA')
37 print(NA)
38 print('Innter na')
39 print(na)
40 print('Diameter of NA')
41 print(D_outer)
42 print('Diameter of na')
43 print(D_inner)
44 print('Annular width')
45 print(D_outer-D_inner)
46
47
48
49 if __name__ == '__main__':
50     main()

```

